MODELING, OPTIMIZATION, AND CONTROL OF DOWN-HOLE DRILLING SYSTEM

A Dissertation

by

KE, CHONG

Submitted to the Office of Graduate and Professional Studies of
Texas A&M University
in partial fulfillment of the requirements for the degree of

DOCTOR OF PHILOSOPHY

Chair of Committee,	Xingyong Song
Co-chair of Committee,	Li-Jung Tai
Committee Members,	Sheng-Jen Hsieh
	Pilwon Hur
Head of Department,	Andreas Polycarpou

August 2020

Major Subject: Mechanical Engineering

ABSTRACT

This dissertation investigates dynamics modeling, optimization, and control methodologies of the down-hole drilling system, which can enable a more accurate and reliable automated tracking of drilling trajectory, mitigating drilling vibration, improving the drilling rate, etc. Unlike many existing works, which only consider drilling control in the torsional dimension, the proposed research aims to address the drilling dynamics modeling and control considering both coupled axial and torsional drill string dynamics. The dissertation will first address optimization and control for vertical drilling, and then resolve critical modeling and control challenges for the directional drilling process.

In Chapter 2, a customized Dynamic Programming (DP) method is proposed to enable a computationally efficient optimization for the vertical down-hole drilling process. The method is enabled by a new customized DP searching scheme based on a partial inversion of the dynamics model. Through extensive simulation, the method is proved to be effective in searching for an optimal drilling control solution. This method can generate an open-loop optimal control solution, which can be used as a guide for drilling control or in a driller-assist system.

In Chapter 3, to enable a closed-loop control solution for the vertical drilling, a neutral-delay differential equations (NDDEs) model based control approach is proposed, specifically to address an axial-torsional coupled vertical drilling dynamics capturing more transient dynamics behaviors through the NDDE. An equivalent input disturbance (EID) approach is used to control the NDDEs model by constructing the Lyapunov-Krasovskii functional (LKF) and formulating them into a linear matrix inequality (LMI). The control gains can be obtained to effectively mitigate the undesired vibrations and maintain accurate trajectory tracking performance under different control references.

The works on Chapter 2 and Chapter 3 are mostly for vertical drilling, and the remaining of the dissertation will focus on modeling and control for directional drilling. Chapter 4

proposes a dual heuristic programming (DHP) approach for automated directional drilling control. By approximating the derivative of the cost-to-go function using a neural network (NN), the DHP approach solves the "*curse of dimensionality*" associated with the traditional DP. The result shows that the proposed controller is robust, computationally efficient, and effective for the directional drilling system.

To validate the DHP based control method using a high-fidelity directional drilling model, a hybrid drilling dynamics model is proposed in Chapter 5. The philosophy of the proposed modeling approach is to use the finite element method (FEM) to describe curved sections in the drill string and use the transfer matrix method (TMM) to model straight sections in the drill string. By integrating different methods, we can achieve both modeling accuracy and computational efficiency for a geometrically complex structure. Compared to existing directional drilling models used for off-line analysis, this model can be used for real-time testbeds such as software-in-the-loop (SIL) system and hardware-in-the-loop (HIL) system.

Finally, a software-in-the-loop real-time simulation testbed is built to test the designed DHP based controller in Chapter 6. A higher-order hybrid model of directional drilling is implemented in the SIL. The SIL results demonstrate that the designed DHP based controller can effectively mitigate harmful vibrations and accurately track the desired references.

DEDICATION

This dissertation is dedicated to my parents

Mr. Wentan Ke and Ms. Yanli Cheng

For their endless love, support, and encouragement

ACKNOWLEDGMENTS

I would like to express my sincere gratitude to the people who made a significant difference in the successful completion of my doctoral study at Texas A&M University.

First and foremost, I would like to thank my advisor, Professor Xingyong Song, for the extraordinary vision, competence, dedication, generosity, knowledge, and guidance he provided me throughout my time at Texas A&M University. I feel forever grateful to be his first Ph.D. student. His energy and consistent support encouraged me towards the completion of my doctoral study. I sincerely appreciate the invaluable insights and continuous inspiration provided by him. What's more, I will never forget the time he has spent reviewing my research outcomes, checking technical details, and proofreading paper drafts. Step by step, he taught me how to express logically and concisely, and how to become an independent researcher.

I would also like to extend my thanks to my committee co-chair, Professor Bruce Li-Jung Tai, my other committee members, Professor Sheng-Jen ("Tony") Hsieh, and Professor Pilwon Hur. I'm sincerely grateful to Professor Bruce Tai for his invaluable advice during my research and coursework, and to Professor Pilwon Hur for his patience whenever I asked questions in his nonlinear control lecture, and to Professor Sheng-Jen ("Tony") Hsieh for his suggestions when I just came to Texas A&M University. In addition, I also would like to thank my former advisor, Professor Won-jong Kim, for spending his time helping me with my research during the early stage of my Ph.D. study.

Besides, I also want to thank my friends and colleagues in the Controls and Mechatronics Research Laboratory, with whom I had the privilege to work and spend time together, including but not limited to Dr. Masood Ghasemi, Dr. Tohid Sardarmehni, Mr. Dongzuo Tian, Mr. Guoqi Ma, Mr. Mohammadali Kargar, Mr. Sai Sudeep Reddy Mandipalli, Mr. Abhishek Paramasivan, and Mr. Zihang Zhang, etc. I gained a lot from working and discussing ideas with them.

Last but certainly not least, my greatest gratitude goes to my family for their love and long-lasting support. From my parents, Mr. Wentan Ke and Ms. Yanli Cheng, I received the most encouragement and strength whenever challenges arose. I'm sincerely grateful for all these years together, and all the happiness we have enjoyed. In addition, my deepest and sincerest gratitude goes to my beloved girlfriend, Ms. Kexin Sun, for her love, understanding, devotions, supports, and encouragement during my study. She has always been an irreplaceable resource of wisdom and strength for me. I feel extremely fortunate to meet her and go through all these incredible years with her together.

CONTRIBUTORS AND FUNDING SOURCES

Contributors

This work was supported by a dissertation committee consisting of Professor Xingyong Song, Professor Sheng-Jen ("Tony") Hsieh of the Department of Engineering Technology and Industrial Distribution and Professor Bruce Li-Jung Tai, Professor Pilwon Hur of the Department of Mechanical Engineering.

All other work conducted for the dissertation was completed by the student independently.

Funding Sources

Graduate study was supported by a Graduate Teaching Assistantship and Graduate Research Assistanship from Texas A&M University, partially supported by the National Academy of Science (NAS) GRP Early Career Research Fellow Award and American Chemical Society (ACS) Doctoral Young Investigator Research Award.

NOMENCLATURE

3-D	Three-Dimensional
ROP	Rate of Penetration
FRF	Frequency Response Function
DOF	Degree of Freedom
EBT	Euler-Bernoulli Beam Theory
TBT	Timoshenko Beam Theory
MC	Monte Carlo
ARMA	Auto Regressive Moving Average
KLD	Karhunen-Loeve Decomposition
DQM	Differential Quadrature Method
FSI	Fluid-Structure Interaction
LPS	Lumped Parameter System
DPS	Distributed Parameter System
NES	Nonlinear Energy Sink
FEM	Finite Element Method
MBD	Multi-Body Dynamics
BHA	Bottom-Hole-Assembly
NDDE	Neutral Delay Differential Equation
DDE	Delay Differential Equation
ODE	Ordinary Differential Equation
PID	Proportional Integral Derivative
PI	Proportional Integral

LMI	Linear Matrix Inequality
MIL	Model-in-the-Loop
SIL	Software-in-the-Loop
HIL	Hardware-in-the-Loop
EID	Equivalent Input Disturbance
PDC	Polycrystalline Diamond Compact
GA	Genetic Algorithm
PDE	Partial Differential Equation
DP	Dynamic Programming
ADP	Approximate Dynamic Programming
MSE	Mechanical Specific Energy
LKF	Lyapunov-Krasovskii Functional
TMM	Transfer Matrix Method
IFT	Inverse Fourier Transform
BOP	Blow-Out Preventer
SNAC	Single-Neuron-Adaptive-Critic
NN	Neural Network
DHP	Dual Heuristic Programming
HDP	Heuristic Dynamic Programming
CT	Continuous-Time
DT	Discrete-Time
WOB	Weight-On-Bit
TOB	Torque-On-Bit
DOC	Depth Of Cut
FFT	Fast Fourier Transform
FSM	Finite Segment Method

FDM	Finite Difference Method
AC	Adaptive Critic
HJB	Hamilton-Jacobian-Bellman
NPT	Non-Production Time

TABLE OF CONTENTS

Page

LIST OF FIGURES

FIGURE Page

LIST OF TABLES

TABLE Page

1. INTRODUCTION

1.1 Introduction and Background

Drilling systems are used to extract natural resources, such as oil and gas, from reservoirs usually deep under ground. The first prehistoric drilling rig dates back to A.D. 347 in China even though this drilling production was hydrocarbon [11]. The ancient Chinese drilled a 240-meter gas well near the salt well to collect enough fuel for lighting and heating [12] [13]. However, it was not until the 19^{th} century that the modern oil industry started in 1859 in Titusville, Pennsylvania, USA [11] [13]. During that year, Edwin L. Drake drilled the first oil well in documented history (see Fig. 1.1). In the 20^{th} century, rotary drilling was introduced to extract and exploit oil and gas. With greater drilling depth and less drilling time, the rotary drilling rapidly increased the drilling production rate and transformed the petroleum industry [13].

Currently, a standard modern rotary drilling rig uses a bit at the bottom of the well, with provided axial force and rotational torque, to cut and break the rock into small pieces. This axial force is provided by the weight of the drill string while the rotational torque is supplied by a motor on the ground and transmitted through the drill string. Meanwhile, the drilling fluid is pumped through the drill string (refer to the green arrow in Fig. 1.2) to wash away the cutting pieces and force the mud to move back to the surface through the annular space between the drill string and the well (see purple arrow in Fig. 1.2). Once reaching the ground, the mud goes through filtering equipment including shale shakers, degreasers, desilters to separate the drilling fluid from small cutting pieces for reuse.

State-of-the-art directional drilling behaves like a flexible robot (Fig. 1.2) traveling through a three-dimensional (3-D) space. As the major component for the down-hole drilling system, drill string typically consists of a number of hollow cylindrical drilling pipes and drill collars and spans more than ten thousand feet. Usually, the top drive motor on the surface

Figure 1.1 First oil well in United States (reprinted from "https://aoghs.org/petroleum-discoveries/" with permission) [1]

provides its primary drilling power and transfers the energy to the drill bit through the drill string. For directional drilling, the drill string is significantly bended, which can be regarded as a three-dimensional curved beam. Drill string control is a crucial element in the drilling automation, as it determines the drilling path (well-bore trajectory) and rate of penetration (ROP). Figure 1.2 shows the control inputs to the down-hole drilling system: top drive torque and hook load force. The complex down-hole environment and the flexible feature of the drill string with such a long scale makes drilling control extremely challenging.

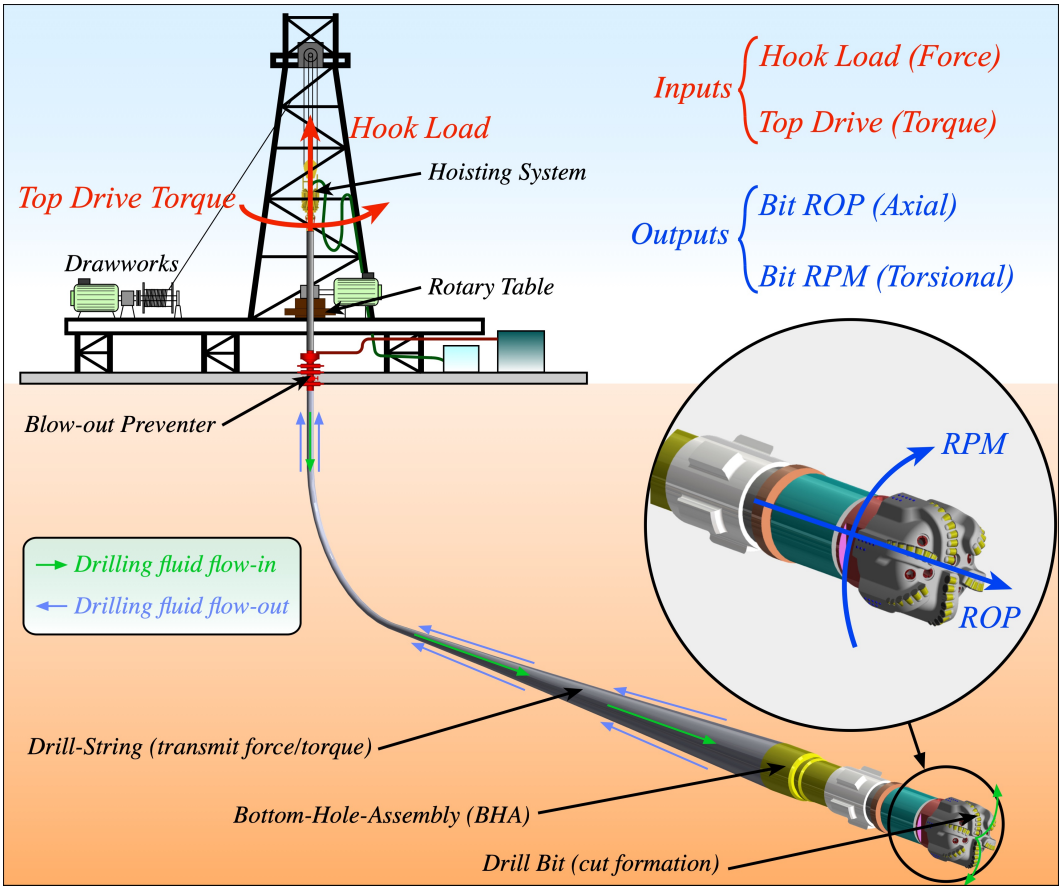

Figure 1.2 Schematic diagram of a common directional drilling system

1.2 Motivation

Traditional drilling operations require the operators to manually control the drill-rig, which has several issues including safety, reliability, control accuracy, drilling efficiency, etc. All of these pose the necessity to design an effective and reliable control to assist the drilling operators for more accurate trajectory tracking, vibration mitigation, drilling efficiency enhancement, and increase of the drilling production rate, etc.

As shown in Fig. 1.2, the down-hole drilling system normally consists of a power unit on the surface, a long drilling pipe (drill string, which can be over $10,000$ feet) through the well-bore, and a down-hole drill bit for rock cutting. The main drilling power is generated on the surface, transmitted to the bit through the large scale drill string (pipe). The primary

control inputs are the torsional torque from the heavy-duty motor to control the rock cutting force, and the axial force to regulate the bit axial motion. Both of the two control inputs are on the surface, separated thousands of feet away from the control outputs (bit torsional and axial velocity) at the drill bit. Although made of steel pipes, the long dimension of the drill string makes its stiffness relatively low, and thus it is, in fact, a flexible pipe in such a large scale [14]. The complex down-hole environment results in unavoidable uncertainty in the drilling dynamics model, and the bit/rock interaction also exhibits strong nonlinearity. All of these pose significant challenges to the control design.

1.3 Literature Review

Over the last several decades, many researchers have conducted investigations regarding drilling dynamics modeling, optimization, and control. These research works can be divided into three categories: drill string dynamics modeling, drill bit dynamics modeling, and drilling system optimization and control.

1.3.1 Drill String Dynamics Modeling

Drill string is an essential component of the drilling system. Due to the large ratio of axial to radial dimension and three-dimensional geometry, the modeling approach for drill string has its uniqueness. In the following, modeling methods classified from the vibration mode perspective and methodology perspective are stated to list the existing drill string modeling approaches.

1.3.1.1 Vibration Mode Point of View

Three different vibration modes occur in drill string dynamics: axial, torsional, and lateral (transverse, flexural, or bending), as shown in Fig. 1.3. Correspondingly, these vibrations are the main causes of "*bit-bounce*," "*stick-slip*," and "*whirl*." The reasons behind these deteriorated phenomena lie on different factors such as BHA imbalance, bit/rock interaction, drill string/well-bore interaction, and drill string three-dimensional geometry, etc. Besides these three vibration modes, there are also three different coupled vibration modes: axial-

lateral, axial-torsional, and torsional-lateral. The following provides the literature review for each of the vibration modes and coupled vibration modes in detail:

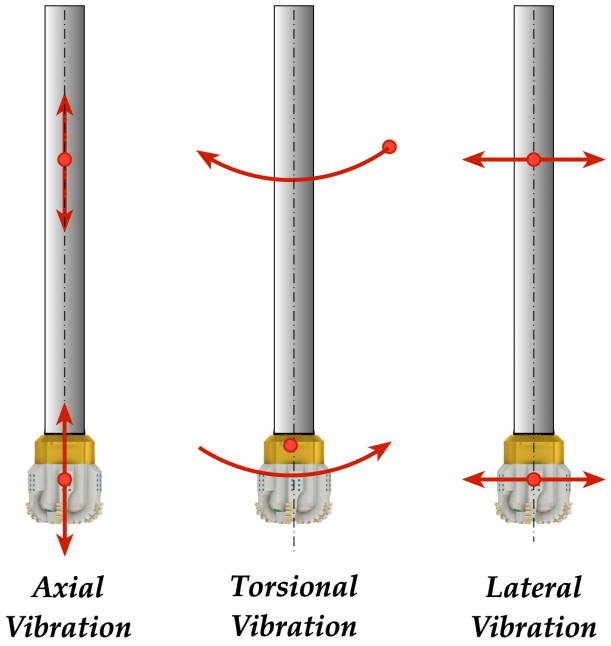

Figure 1.3 Basic vibrations in down-hole drilling dynamics

Axial Vibration Models: There are various different models to describe the axial vibration in the drilling system. Bailey and Finn developed the analytical solution for drilling axial vibration from the linear undamped partial differential equation (PDE) in 1960 [15]. In 1963, Paslay and Bogy investigated the longitudinal vibration in the drill bit [16]. Dareing and Livesay added a damping term to the linear partial differential equation to account for more details for longitudinal vibration [17]. In 1970, Kreisle and Vance implemented the Laplace transformation to the linear damped partial differential equation on the shock sub effects [18]. In 1984, Dareing studied the undamped partial differential wave equation and found that the length of the bottom-hole-assembly (BHA) and drill collar is a major factor to control longitudinal vibration [19] [20]. Skaugen and Kyllingstad tested out a sinusoidal vibration under a 1000 m vertical drill string by the down-hole exciter [21]. Then

Skaugen developed a friction model and studied the quasi-random drill string vibration based on a linear damped partial differential equation [22]. In 1991, Hyun Yup Lee used a single-layered acoustic waves model to analyze an infinitely long, uniform drill string in his Ph.D. dissertation [23]. In 1993, Dunayevsky ascertained the stability region under the undamped uncoupled axial vibration [24]. Parfitt and Abbassian used a finite difference method (FDM) to account for drill string dynamics and considered viscous damping and nonlinear bit-formation dynamics [25]. Niedzwecki and Thampi used Dareing and Livesay's model and discussed the Heave response predictions for long rise-less drill string [26]. In 2000, Schmalhorst et al. took consideration of the mud flow circulation with the drill string axial vibration dynamics [27]. In 2005, Elsayed and Phung modeled a drill string into 28 separate masses and springs in series. By using the frequency response function (FRF), they showed that the above model can be simplified into a model with 6 chosen modes [28]. In 2007, Li et al. used the damped axial vibration equation for a bar and verified the bit-displacement model through drilling field data [29]. In 2016, Tian et al. studied the longitudinal vibration considering the inertia effect from lateral vibration [30].

Torsional Vibration Models: The torsional vibration has been widely studied and described by the torsional pendulum model for years. Lin and Wang proposed the one degree-of-freedom (DOF) equation to simplify the drill string dynamics and also added dry friction to model the torsional bit/rock interaction [31]. Jansen and Steen modified the bit-rock interaction model to a threshold limiting function and also considered the drive system dynamics [32]. In 1999, Tucker and Wang built a comprehensive drilling system model based on cosserat rod theory [33]. Halsey et al. also used the torsional pendulum model of drill string torsional vibration to calculate the torsional vibration frequencies and compared them to experimental data [34]. Baumgart derived a finite element model for the drilling process from energy conservation equations [35]. Challamel investigated the distributed parameter system model and combined them with the field data [36]. Besselink studied a semi-analytical solution and limit cycle for axial linear stability [37]. Barton et al. performed the bifurcation

analysis based on a nonlinear torsional model [38]. Navarro-Lopez and Cortes studied the higher order model and considered the torsional sliding motion and bit bouncing phenomena at the same time. They used Hopf bifurcation to determine when the undesired vibrations happen [39].

Lateral Vibration Models: Both analytical and numerical models have been proposed for the drilling system lateral vibrations. Compared with the axial and torsional vibrations, the lateral vibration could potentially become more destructive than the other vibration modes and hasn't been investigated thoroughly. Generally, the Euler-Bernoulli beam theory (EBT) is the most widely used model for drill string lateral vibration [40], though some researchers may use the Timoshenko beam theory (TBT) to extend the EBT considering shear deformation [41]. There are two types of lateral vibration models for the drilling system: single-plane models and three-dimensional models [42]. Rong-Juin Shyu thoroughly discussed the bending vibration due to dynamic axial force and whirling behavior with or without bore-hole contact in his Ph.D. dissertation [43]. Jansen investigated the interaction between drill string and well-bore in polar coordinate. He discussed the stability regions for the forward and backward whirling [44]. Chen and Geradin proposed a three-dimensional lateral vibration analysis based on the analytical transfer matrix method [45]. Berlioz et al. modeled the lateral behavior of the drill string subjected to bit excitation [46]. Christoforou and Yigit studied lateral vibration modal analysis of the BHA and found the causes of the failure. [47]. Spanos et al. (1997) implemented the transfer function method based on modal superposition to investigate the effects of frequency-dependent fluid added mass and nonlinear well-bore constraints on the lateral response of the BHA. [48]. Spanos developed a finite element discretization for a nonlinear dynamic model. He also considered stochastic scenarios in his model by using the Monte Carlo (MC) method and Auto Regressive Moving Average (ARMA) [49]. Khajiyeva et al. developed a nonlinear coupled lateral vibrations model under axial compression and torsional torque. In addition, the fluid flow is also considered as an added mass to the drill string [50].

Axial-Torsional Coupled Models: Elsayed and Raymond studied axial-torsional coupled dynamics for drill string and discussed the coupling effects [51]. Yigit and Christoforou proposed a 2 DOF torsional model and 1 DOF axial model and considered the coupling effect at the drill bit [52]. Sampaio et al. investigated the axial-torsional coupling drill string vibration based on a nonlinear finite element model. They found the nonlinear model differed considerably with the linear model on the first period of stick-slip [53]. Zamanian et al. studied a two DOF lumped model for torsional vibration and one DOF model for axial vibration. He concluded the coupling happened in the bit/rock interaction [54]. Chi et al. investigated drill string failure life and also concluded that the bit/rock interaction coupling for axial & torsional motions [55]. Germay et al. investigated the effect of axial vibration to stick-slip behavior [56].

Axial-Lateral Coupled Models: Trindade and Sampaio used Karhunen-Loeve (orthogonal) decomposition (KLD) and applied it to the nonlinear axial-lateral finite element model. The results show that 15 proper orthogonal modes are sufficient to account for the dynamics reconstruction [57]. Hakimi and Moradi applied the differential quadrature method (DQM) to analyze the vertical drill string vibration [58]. Jafari et al. determined a continuous axial-lateral coupled model and considered drilling mud effect [59] [60]. Sahebkar used perturbation techniques to solve the axial-lateral coupled model and investigated the stability region [61]. Ghasemloonia et al. investigated the coupled axial-lateral model from the partial differential equations. And these results are validated by the finite element method in [62].

Torsional-Lateral Coupled Models: Christoforou and Yigit first analyzed torsional-lateral coupled vibrations. A polar coordinate newton's method was used considering contact between the drill string and well-bore [47]. Al-Hiddabi et al. used Newton's law and Lagrangian dynamics to present the torsional-lateral coupled dynamics and designed a nonlinear dynamic inversion control to suppress these coupled vibrations [63]. Leine et al. addressed the stick-slip whirl interaction and considered fluid interaction and well-bore

contact [64]. Melakhessou et al. developed a four DOF Lagrangian model to integrate torsional-lateral coupled dynamics and verified through experiments [65]. In 2007, Richard derived a torsional-bending coupled model to study the stick-slip phenomenon [2]. Liao et al. proposed a reduced-order distributed parameter model that allows for torsional-lateral coupled dynamics. They considered the interaction between the drill string and well-bore and further validated the simulation with a scaled experimental apparatus [66] [67]. More details can be found in his Ph.D. dissertation in 2011 [68].

Axial-Torsional-Lateral Coupled Models: In 2000, Baumgart studied a fully coupled drill string vibrations and considered the effects of mud flow and pump pressure on the drill string vibration [35]. In 2005, Kulief and Al-Naser developed a finite element model for fully coupled dynamics. This model considered the gyroscopic effect, torsional-lateral inertia coupling, and the effect of the gravitational force field [69]. In 2008, Kulief and Al-Naser extended its finite element model to accommodate contact-impact behavior [70]. In 2009, Ritto et al. developed a fully coupled drill string model and considered a simplified fluid-structure interaction (FSI) [71]. In 2017, Feng et al. presented a 6 DOF finite element model to characterize the drill string dynamics. In this model, a comprehensive bit-force model along with a boundary condition was developed [72].

1.3.1.2 Modeling Methodology Point of View

From the modeling methodology perspective, we can divide the down-hole drilling models into two categories: lumped parameter system (LPS) and distributed parameter system (DPS).

Lumped Parameter System: Spring-mass-damper model is a classical model for the lumped parameter system (see Fig. 1.4 and Fig. 1.5). In 2004, Richard developed a simplified axial-torsional coupled model [73]. In 2007, Richard further modified his model, converted into a dimensionless form, and conducted bifurcation analysis [2]. Nandakumar also used Richard's model but emphasized on discussion of a state-dependent time delay in the bit-rock interaction [74]. In 2015, Kapitaniak et al. investigated a complex drill string dynamics

on an experimental rig and used a low-dimensional torsional pendulum model [75].

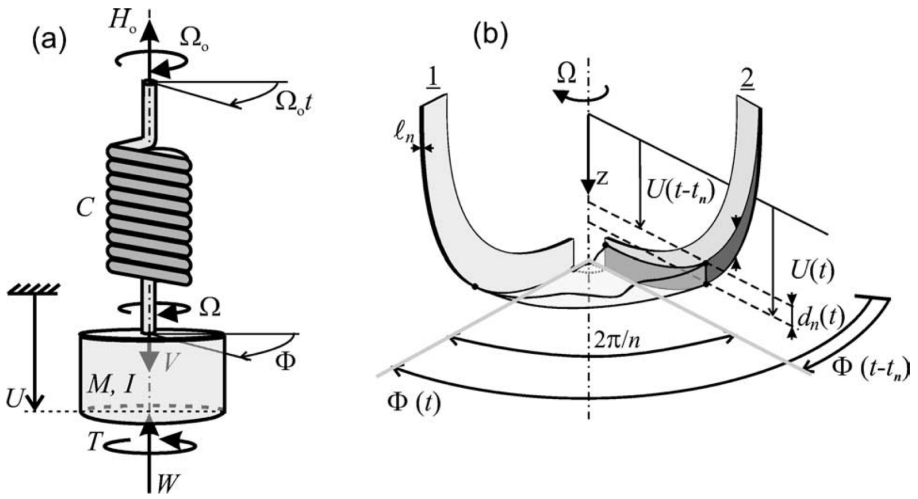

Figure 1.4 Richard's simplified single spring-mass-damper model (reprinted with permission) [2]

Although a linear stability analysis can be analyzed in this model, it lacks the fidelity to accurately describe the long slender drill string. To address this issue, multiple spring-mass-dampers model was investigated. Melakhessou et al. developed a four DOF Lagrangian model to investigate the coupled vibration [65].

In addition, the finite element method is a numerical method to solve the partial differential equations. It provides a more high-fidelity solution for geometrically complex structures. Generally, system dynamics is derived from Lagrangian mechanics. Reference papers can be seen in [14] [76] [69] [70] [72]. Although this method is widely used in many applications, it has the drawback of significant computational expenses for drill-sting dynamics modeling.

Distributed Parameter System: Distributed parameter system provides a more accurate result than the lumped parameter system for drill string dynamics modeling. As one type of distributed parameter system, the partial differential equation is infinite-dimensional and usually derived from the Euler-Bernoulli beam theory, either undamped or damped. Ritto et al. proposed a partial differential equation model and analyzed the stochastic fric-

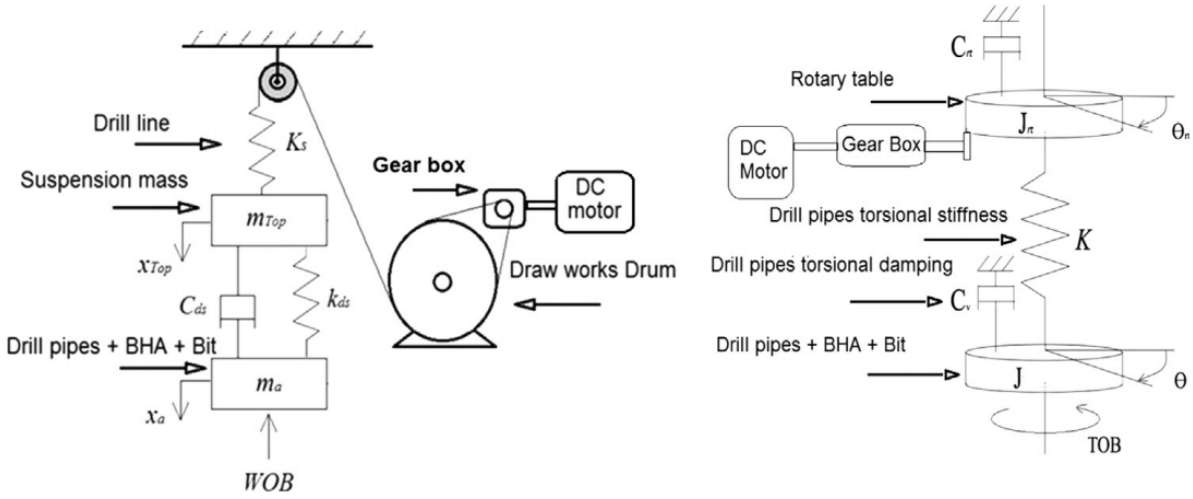

Figure 1.5 Yigit's simplified multiple spring-mass-damper model (reprinted with permission) [3]

tional force in the bit [77].

Through applying the "*D'Alembert's*" formula, the hyperbolic partial differential equations can be transformed into a set of neutral delay differential equations (NDDE). NDDE is a particular kind of delay differential equation (DDE) [78] [79]. Saldivar et al. worked on the neutral delay differential equation model for down-hole drilling system [80] and developed different control methods to suppress the stick-slip phenomenon such as Proportional-Integral-Derivative (PID) control [81], flatness based control [82], linear matrix inequality based control [83], and attractive ellipsoid method [84], etc. But all these controllers deal with torsional only dynamics, which neglects the essential axial-torsional coupling effect at drill bit dynamics.

1.3.2 Drill Bit Dynamics Modeling

Since the early 1940s, rock cutting mechanics has been reported in the literature. In 1944, Mechant firstly developed a semi-empirical cutting theory for the metal cutting process [4]. Based on the Mohr-Coulomb plasticity criterion, this model considered the force equilibrium of the single shear plane in the orthogonal cutting action. Based on Coulomb's criterion and

the shear plane assumption, Merchant's cutting force equation can be expressed by [4] [5]:

$$F_d = F_c = \tau_s A_c \frac{\cos(\beta - \gamma_b)}{\sin\phi \cos(\phi + \beta - \gamma_b)} \tag{1.1}$$

where τ_s is the shear strength of the work material on the shear plan; β is the mean angle of friction between the chip and tool; ϕ is the shear angle, γ_b is the working normal rake angle (or back angle in rock cutting); and A_c is the cross-sectional area of uncut chip as shown in Fig. 1.6. In the Merchant's model, the drag force F_d is equivalent to the cutting force F_c. The shear angle ϕ can be derived based on the assumption of minimum cutting force, i.e.,

$$2\phi + \beta - \gamma_b = \frac{\pi}{2} \tag{1.2}$$

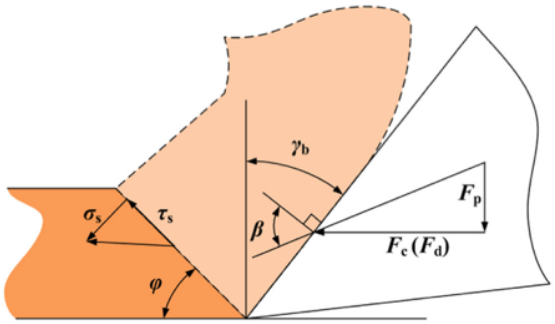

Figure 1.6 Schematic diagram of Mechant's and Nishimatsu's metal cutting model (reprinted with permission) [4] [5]

This is the first complete metal cutting model and most of the later models are based on this model. However, due to the fact that it's based on an ideally sharp cutter, its applicability is limited. Fairhurst and Lacanne considered the wear phenomenon and proposed that

the forces are on a drag bit along the wear-flat. Their model can be expressed by [6]:

$$F_p = pA_f, \quad F_d = F_c + \mu p A_f \tag{1.3}$$

where F_p and F_d are the vertical and horizontal components of the resultant force; F_c is the cutting force exerted by the diamond-rock interface; A_f is the area of the flat; p is the contact pressure under the bit; and l is the coefficient of friction at the wear-flat of the cutter-rock interface (Fig. 1.7). Based on Mohr's criterion of failure and the specific stress distribution assumption, Nishimatsu proposed a formula for the cutting force in rock cutting by a wedge-shaped tool, which can be described by [85]:

$$F_c = \frac{2}{n+1} \cdot \tau_c A_c \cdot \frac{\cos k}{1 - \sin(k - \gamma_b + \beta)} \cdot \cos(\beta - \gamma_b) \tag{1.4}$$

where n is the stress distribution factor and k is the angle of internal friction. Compared to Merchant's model, Nishimatsu's model considered the brittle mode failure criterion during the cutting process. In his model, cutting chips are periodically formed and sheared off. The shortcoming of this model is that it fails to describe the ductile mode of failure.

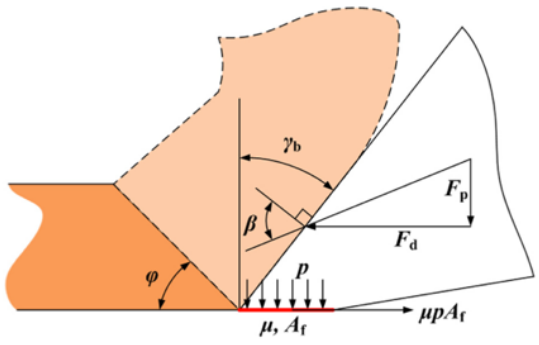

Figure 1.7 Schematic diagram of Fairhurst and Lacanne's metal cutting model (reprinted with permission) [6] [5]

Lebrun extended Nishimatsu's theory. He developed a 3-D model to simulate the failure of the rock due to the cutting tool action. He proposed the linear relationship between cutting force and depth of cut (DOC) and specifies that this coefficient proportionally depends on the width, wear, and rake angle of the cutter [86]. Cheatham [87] showed that the cutter forces are functions of the cutting area and rock shear strength. Warren and Sinor investigated a PDC cutter force model that introduces a bit factor to combine the performance of individual cutters and the full-scale bit:

$$F_p = c_1 \frac{\cos(\beta - \gamma_b)}{1 - \sin(\beta - \gamma_b)} B_F S_R A_c + c_2 S_R A_w \tag{1.5}$$

where B_F is a bit factor to account for unexplained effects for a particular bit; S_R is a relative rock strength roughly proportional to the compressive strength of the rock; c_1 and c_2 are constants obtained from the drilling data [88]:

$$F_d = c_3 \frac{\sin(\beta - \gamma_b)}{1 - \sin(\beta - \gamma_b)} S_R A_c + c_4 F_p \tag{1.6}$$

where c_3 and c_4 are constants.

Glowka developed a practical conceptual model of the rock drag cutting process to provide a mathematical description of the penetrating and drag forces applied during the process [89]. In 1991, Detournay and Atkinson obtained an analytical solution for the 2-D rock cutting that considers the angle of the internal friction of the rock [90]:

$$\epsilon = \frac{2 \cos\phi \cos(\theta + \Psi_n)}{1 - \sin(\phi + \theta + \Psi_n)} [\tau_0 + k(P_b - P_p)] \tag{1.7}$$

In 1992, Detournay and Defourny adopted the force response mechanism of a drag bit [7], which was first developed by Fairhurst and Lacabanne [6] and experimentally verified by Glowka [89]. This model builds cutting force models for both sharp and worn cutters by

introducing three constants: the intrinsic specific energy ϵ, the cutter geometry coefficient ζ, and friction coefficient μ. For sharp cutters, the penetrating and drag forces can be expressed by:

$$F_d = \epsilon A_c, \qquad F_p = \zeta \epsilon A_c \tag{1.8}$$

For worn cutters, the friction force acting across the wear-flat should also be considered:

$$F_d = (1 - \mu\zeta)\epsilon A_c + \mu F_p \tag{1.9}$$

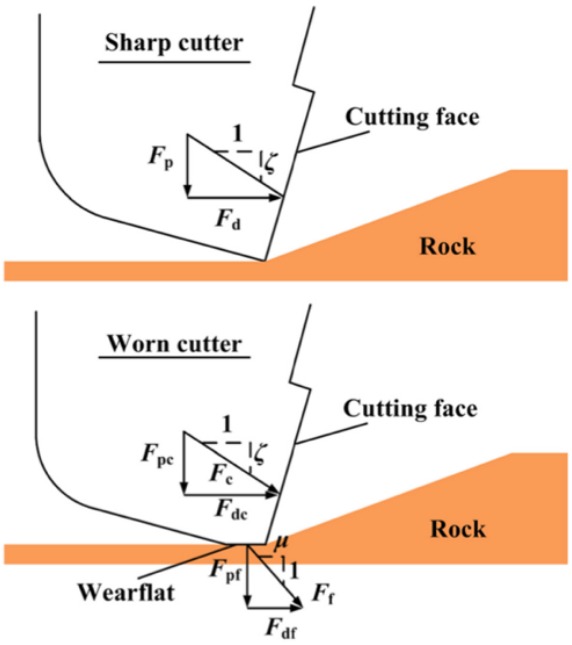

Figure 1.8 Schematic diagram of Detournay's metal cutting model (reprinted with permission) [7] [5]

Figure 1.8 shows the force response in the Detournay-Defourny model (D-D model). It provides a convenient way to predict the force response at the cutter-rock interface since the force can be quantified through bit characteristic constants. However, this model fails

to describe the cutting process under the plastic mode of rock failure [91]. Even though this limits its applications, it still simplified the modeling of the rock-cutting process. Since then, Almenara (1992), Samiselo (1992), Lasserre (1994), Kuru and Wojtanowicz (1995), and Adachi (1996) also provided experimental supports to the D-D model [91] [92] [93] [94].

There are three main assumptions in the D-D model:

1. The cutting process can be decomposed into the "*pure cutting*" process and the "*frictional contact*" process at the wear flat-rock interface.
2. Cutting force exerted on the cutting face is proportional to the groove cross-sectional area (A_c).
3. The frictional force acting on the wear flat-rock interface is independent of the depth of cut (d_{oc}).

In 2006, Gerbaud et al. developed a novel cutter-rock interaction model to include the effects of chamfer, side, and back rake angles of the cutter:

$$F = F^c + F^{ch} + F^b \tag{1.10}$$

where F^c, F^{ch}, F^b represent forces exerting on cutting face surface, chamfer surface, and back cutter surface, respectively [95]. They introduced the built-up edge of crushed materials on the cutting face that was observed by Zijsling [96] and Adachi et al. [91] to provide an assessment of the back and side rake angle effects on PDC forces.

In 2008, Detournay et al. proposed a drill bit dynamics model and experimentally verified its results [8]. Recently, Rostamsowlat did extensive experiments and further improved and verified the D-D model [97] [98].

1.3.3 Control Schemes and Strategies

Most existing studies on drilling control focus on torsional vibration mitigation, rather than the motion control in both axial and torsional direction. Jansen and Steen proposed a torsional vibration controller based on a torsional pendulum model [32]. Serrarens introduced

an H_∞ controller to suppress the torsional stick-slip phenomenon in [99]. In 1999, Tucker proposed a "*torsional rectification*" method to suppress the stick-slip [33]. In 2003, Tucker and Wang used a so-called "*soft torque*" method for torsional vibration reduction [100]. Abudulgalil and Siguerdidjane designed a back-stepping controller to track the bit torsional velocity [101]. Navarro-Lopez and Cortres presented an n-dimensional lumped torsional model and designed control strategies by studying local bifurcations of the system [39]. Karkoub et al. studied a torsional vibration control approach based on the Genetic Algorithm (GA) in [102]. In 2012, Kreuzer regarded torsional vibration as an acoustic wave and used the algorithm to absorb the traveling wave to mitigate torsional vibration [103]. In 2013, Sagert et al. developed a back-stepping transformation technique control for PDEs [104]. Recently, Feng et al. developed a Dynamic Programming based reduced-order controller in [105]. However, for the aforementioned works, the models adopted only contain torsional dynamics, and the control considered is mainly stabilization in torsional direction. As pointed out in [8] and also validated with experimental data [33], the torsional and axial dynamics are indeed coupled at the drill bit, and it is more desirable to have control design based on the coupled dynamics. Besides, instead of only having vibration reduction and system stabilization, a more efficient, cost-effective, and smooth drilling process requires drilling rate regulation, axial trajectory control, and optimal drilling process management, which needs to be resolved by a systematic control/optimization scheme.

1.4 Research Objectives

The purpose of this research is to develop dynamics modeling and control for both vertical down-hole drilling systems and directional down-hole drilling systems. Compared with existing control approaches, the proposed research can provide more effective and reliable controls for more accurate trajectory tracking, mitigating vibrations, increasing energy efficiency, and preventing drilling failures.

Unlike many existing works, which only consider drilling control in the torsional dimension, the proposed research aims to address the drilling dynamics modeling and control con-

sidering both coupled axial and torsional drill string dynamics with a high-fidelity dynamics model. The dissertation will first address optimization and control for vertical drilling, and then resolves critical modeling and control challenge for the directional drilling process.

1.5 Dissertation Overview

In summary, this dissertation investigates the dynamics modeling, optimization, and control methodologies for the down-hole drilling system, which enables more smooth and energy-efficient motion of the drill bit, mitigates detrimental vibrations, maintains trajectory tracking, increases production rate for existing drilling process, and prevents drilling failures, etc. We will address vertical drilling optimization and control first, and then resolve critical modeling and control challenge for the directional drilling process, as shown in Fig. 1.9.

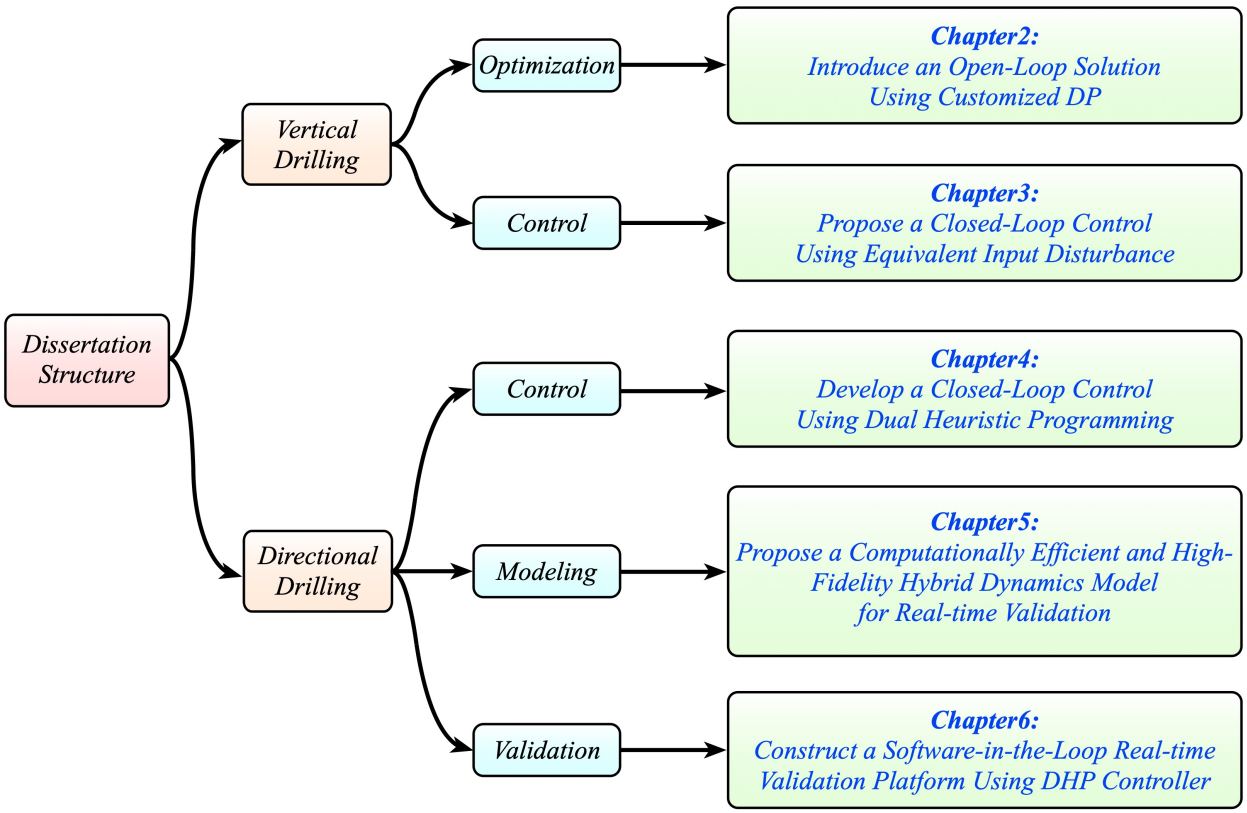

Figure 1.9 Dissertation structure

Chapter 2 and Chapter 3 present the dynamics modeling, optimization, and control for the vertical drilling system. A customized Dynamic Programming method is proposed in Chapter 2 to enable a computationally efficient optimization for the vertical down-hole drilling process. The method is enabled by a new customized DP searching scheme based on a partial inversion of the dynamics model. Through extensive simulation, the method is proved to be effective in searching for an optimal drilling control solution. This method can generate an open-loop optimal control solution, which can be used as a guide for drilling control or in a driller-assist system.

To enable a closed-loop control solution, a neutral-model based control approach is proposed in Chapter 3, specifically to address an axial-torsional coupled vertical drilling dynamics capturing more transient dynamics behaviors through the neutral model. The drilling dynamics can be described by neutral-type time-delay equations through applying the "*D'Alembert*" formula for partial differential equations. The equivalent input disturbance method is used to estimate the uncertain bit-rock interaction, and formulate the proposed Lyapunov-Krasovskii functional into a linear matrix inequality. Thus the control gains can be obtained to effectively mitigate the undesired vibrations, maintain accurate trajectory tracking performance under different control references.

While the works on Chapter 2 and Chapter 3 are mostly for vertical drilling, the remaining of the dissertation will focus on modeling and control for directional drilling. With three-dimensional curved geometry, the dynamics of the directional drilling inevitably requires much more order than the vertical drilling dynamics, and DP becomes computationally infeasible to be used for directional drilling control/optimization. Therefore, we apply the approximate dynamic programming (ADP) framework in Chapter 4. Specifically, a dual heuristic dynamic programming control approach is proposed for optimal control of the directional drilling system. The proposed approach used the neural network to approximate the derivative of the cost-to-go function and further formulated the optimal solution of a high-dimensional problem, which can be used to address the "*curse of dimensionality*" in

the traditional DP.

With the DHP based controller designed in Chapter 4, a high-fidelity directional drilling dynamics model is presented in Chapter 5 to be used for real-time control validation. The existing high-fidelity drilling dynamics models are mostly high order and thus computationally intensive, which is hard to be used for real-time validation in terms of hardware-in-the-loop simulation or software-in-the-loop simulation. The new model we proposed integrates two distinct modeling approaches (the finite element and the transfer matrix) and has merits of both model accuracy and computational efficiency with the purpose of using it directly into the real-time software-in-the-loop real-time system and hardware-in-the-loop (HIL) system.

Finally, a software-in-the-loop real-time validation platform is developed in Chapter 6, and the designed DHP based controller is validated using a 68 DOF higher-order hybrid directional drilling dynamics model.

The details of each chapter will be presented as follows:

Chapter 2: Optimization of Vertical Down-Hole Drilling Process Using a Computationally Efficient Dynamic Programming Method

In this chapter, we present a method based on Dynamic Programming that can lead to a computationally efficient drilling control optimization. A drilling dynamics model that can enable this method is first constructed, and the DP algorithm is customized so much improved computational efficiency can be achieved compared with using standard DP. A higher-order dynamics model is then used to validate the effectiveness of the optimized control, and the control robustness is also evaluated by adding perturbations to the model. The results verify that the proposed approach is effective and efficient to solve the down-hole drilling control optimization problem.

Chapter 3: Control of Vertical Down-Hole Drilling Process Using an Equivalent Input Disturbance Approach with a Neutral-Type Axial-Torsional Coupled Dynamics Model

This chapter proposed an equivalent input disturbance based approach to control the

vertical down-hole drilling process using a distributed parameter model. To describe a drill string that is typically long with a large axial-to-radius ratio, a neutral type model is used to accurately capture the dynamics of this type of slender string structure. The axial-torsional coupling effect due to drill bit-rock interaction is also included in the model. A new controller is then designed based on the coupled neutral model and the coupling effect is specifically addressed in the design. To address the uncertainty of the bit-rock interaction, the equivalent input disturbance method is used. A new Lyapunov-Krasovskii functional is proposed for the control design. To this end, a series of numerical simulation results are presented to demonstrate the effectiveness of the proposed control scheme.

Chapter 4: Control of Directional Down-Hole Drilling Process Based on Dual Heuristic Programming

In this chapter, a single-neuron-adaptive-critic (SNAC) dual heuristic programming based controller is proposed for trajectory tracking and rate of penetration control of the directional down-hole drilling process. A finite element dynamics model is firstly customized and further formulated into the optimal control problem, then the DHP based controller is constructed in the finite receding horizon. Instead of searching all the states' and inputs' spaces, the SNAC-DHP approach uses one neural network to approximate the gradient of the cost-to-go function to obtain the optimal control inputs. The greatest advantage of using this approach is that the computational expenses will mostly depend on the convergence of the neural network no matter how many states and inputs this system has. Therefore, this approach can be used to solve the optimal control problem of the very high-dimensional system such as the directional drilling system. To this end, a series of simulations are conducted to evaluate the efficacy of this proposed controller. The robustness of this controller is also discussed, and the computational expenses also show the potential to apply this approach to other high-dimensional control problems.

Chapter 5: A Hybrid Directional Drilling Dynamics Model Integrating Finite Element and Transfer Matrix

This chapter presents a computationally efficient dynamics model for the directional down-hole drilling system integrating finite element and transfer matrix. Due to the long dimension of the drill string, a drilling model based on pure numerical methods such as the finite element method may require a large number of meshes, which induces high computational intensity. By using a hybrid method combining the finite element method and the transfer matrix method, the order of the model can be significantly reduced. To this end, simulation results are presented to demonstrate the effectiveness of the proposed hybrid modeling approach in terms of accuracy, robustness, and sensitivity. Results show that a computationally-efficient and high-fidelity hybrid model can be reached for real-time state estimation and control design.

Chapter 6: Validation of Directional Drilling Control Using Software-in-the-Loop

In this chapter, a software-in-the-loop real-time simulation testbed is constructed in LabVIEW for control validation. Then the higher-order hybrid directional drilling dynamics model is used to validate the DHP based controller designed in Chapter 4. The SIL real-time validation results demonstrate that the proposed DHP based controller can effectively mitigate harmful vibrations and accurately track the desired references.

2. OPTIMIZATION OF VERTICAL DOWN-HOLE DRILLING PROCESS USING A COMPUTATIONALLY EFFICIENT DYNAMIC PROGRAMMING METHOD*

The unconventional down-hole resources such as shale oil and gas have gradually become a critical form of energy supply thanks to the recent petroleum technology advancement. Its economically viable and reliable production highly depends on the proper operation and control of the down-hole drilling system. The trend of deeper drilling in a complex environment requires a more effective and reliable control optimization scheme, either for pre-drilling planning or on-line optimal control. Given the nonlinear nature of the drilling system, such an optimal control is not trivial. In this chapter, we present a method based on Dynamic Programming that can lead to a computationally efficient drilling control optimization. A drilling dynamics model that can enable this method is first constructed, and the DP algorithm is customized so much improved computational efficiency can be achieved compared with using standard DP. A higher-order dynamics model is then used to validate the effectiveness of the optimized control, and the control robustness is also evaluated by adding perturbations to the model. The results verify that the proposed approach is effective and efficient to solve the down-hole drilling control optimization problem.

2.1 Introduction

The recent technology advancements in directional drilling and hydraulic fracturing enable more cost-effective and reliable production of shale oil and gas. This unconventional energy revolution may eventually shift North America into a world energy center. As the essential component to explore the down-hole energy, the down-hole drilling system requires

*Reprinted with permission from "Control of Down-hole Drilling Process Using a Computationally Efficient Dynamic Programming Method," **C. Ke** and X. Song, *ASME Transactions on Journal of Dynamic Systems, Measurement and Control* 140.10 (2018): 101010, Copyright 2018 by ASME Publisher

more optimal and reliable control, for accurate trajectory tracking, mitigating vibrations, enhancing energy efficiency of the drilling system, and preventing drilling failure. The trend of deeper well [106] and a more complex drilling environment makes the control problem increasingly challenging.

As shown in Fig. 2.1, the down-hole drilling system normally consists of a power unit on the surface, a long drilling pipe (drill string, which can be over 10,000 feet) through the wellbore, and a down-hole drill bit for rock cutting. The main drilling power is generated on the surface, transmitting to the bit through the large scale drill string (pipe). The primary control inputs are the torsional torque from the heavy-duty motor to control the rock cutting force, and the axial force to regulate the bit axial motion. Both of the two control inputs are on the surface, separated thousands of feet away from the control outputs (bit torsional and axial velocity) at the drill bit. Although made of steel pipes, the long dimension of the drill string makes its stiffness relatively low and thus it is in fact a flexible pipe in such a large scale [14]. The complex down-hole environment results in unavoidable uncertainty in the drilling dynamics model, and the bit-rock interaction also exhibits strong nonlinearity. All of these pose significant challenges to the control design.

Most existing studies on drilling control focus on torsional vibration mitigation, rather than the motion control in both axial and torsional direction. Jansen and Steen proposed a torsional vibration controller based on a torsional pendulum model [32]. Serrarens introduced an H_∞ controller to suppress the torsional stick-slip phenomenon in [99]. Tucker and Wang used a so-called "*soft torque*" and "*torsional rectification*" methods for torsional vibration reduction [100]. Abudulgalil and Siguerdidjane designed a backstepping controller to track the bit torsional velocity [101]. Navarro-Lopez and Cortres presented an n-dimensional lumped torsional model and designed control strategies by studying local bifurcations of the system [39]. Karboub et al. studied a torsional vibration control approach based on the Genetic Algorithm in [102]. Recently, Feng et al. developed a Dynamic Programming based reduced-order controller in [105]. However, for the aforementioned works, the models

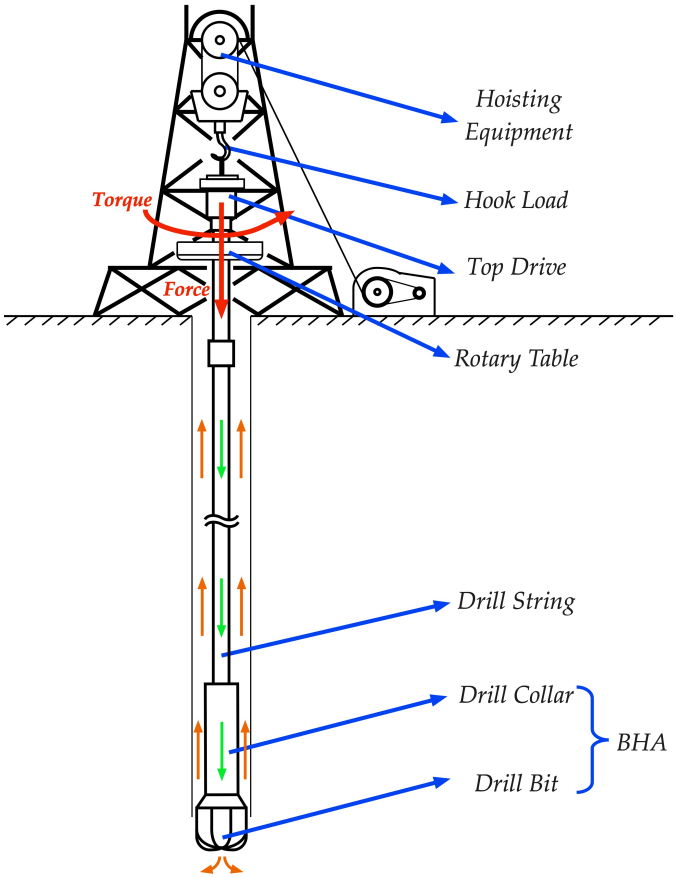

Figure 2.1 Schematic diagram of the vertical down-hole drilling system

adopted only contain torsional dynamics, and the control considered is mainly stabilization in torsional direction. As pointed out in [8] and also validated with experimental data [33], the torsional and axial dynamics are indeed coupled at the drill bit, and it is more desirable to have control design based on the coupled dynamics. Besides, instead of only having a vibration reduction and system stabilization, a more efficient, cost-effective, and smooth drilling process requires drilling rate regulation, axial trajectory control, and optimal drilling process management, which needs to be resolved by a systematic optimization scheme.

In this chapter, we will investigate an approach to optimize the vertical drilling control. The framework can be used for either pre-drilling planning or on-line control optimization, which requires the optimization to be computationally efficient. Dynamic programming is a

well-established approach for optimal control of complicated and highly nonlinear systems [107] [108] [109]. However, the main challenge of using standard DP is the high computational intensity [110]. It will be shown later in this chapter that, it is hard to directly apply the standard DP for real-time drilling optimization due to its high computational cost. To address that, in this chapter, we propose a computationally efficient approach to optimize the drilling control under the DP framework. We first approximate the nonlinear drill bit dynamics model using a term that can make the drilling dynamics model partially invertible. This approximation is proved to be valid in the desired drilling operation conditions. Then leveraging the partial invertibility of the nonlinear dynamics, we can customize the DP algorithm and have the optimization conducted in a more computationally efficient fashion. The simulation results demonstrate the effectiveness of the optimized control inputs on both the axial and torsional dynamics control. In addition, to enable robustness when having uncertainties, model parameter perturbations can also be considered in the optimization process.

The rest of the chapter is organized as follows. Section 2.2 presents the dynamics model for the down-hole drilling system, where an approximation on drill bit dynamics is made to enable the computationally efficient DP design. Section 2.3 describes the proposed optimization approach under the DP framework. In section 2.4, a series of simulations are conducted to demonstrate the feasibility of the proposed optimization algorithm. The summary of this chapter is presented in section 2.5.

2.2 Drilling System Dynamics Modeling

The drilling dynamics model will be presented in this section. We will first use a lower order model for the DP control optimization, and then use a higher-order model to validate the control performance. Meanwhile, an approximation is made for the drill bit dynamics to enable a computationally efficient approach using DP.

2.2.1 Drill String Modeling

Drill string is the major component in the drilling system connecting the drilling power source on the surface with the down-hole drill bit. In this chapter, we follow the same assumptions widely made in vertical drilling system modeling [74] [111] [112]. Specifically, (i) vertical well-bore is considered and the axial/torsional dynamics are dominant. Thus lateral motion can be neglected. (ii) top drive is regarded as a massless and inertia-less circular plate.

The system dynamics of the drill string can be written as:

$$\begin{cases} \dot{x}_1(t) = x_2(t) \\ \dot{x}_2(t) = -\dfrac{C_a}{M}x_2(t) - \dfrac{K_a}{M}(x_1(t) - u_1(t)) + \dfrac{Mg - WOB\Big(x_2(t), x_4(t)\Big)}{M} \\ \dot{x}_3(t) = x_4(t) \\ \dot{x}_4(t) = -\dfrac{C_t}{I}x_4(t) - \dfrac{K_t}{I}(x_3(t) - u_2(t)) - \dfrac{TOB\Big(x_2(t), x_4(t)\Big)}{I} \end{cases} \tag{2.1}$$

where the state vector is defined as: $\Big[x_1, x_2, x_3, x_4\Big]^T = \Big[x_{bit}(t), \dot{x}_{bit}(t), \theta_{bit}(t), \dot{\theta}_{bit}(t)\Big]^T$, with the initial condition $\Big[x_1(0), x_2(0), x_3(0), x_4(0)\Big]^T = \Big[0, 0, 0, 0\Big]^T$; control input is $\Big[u_1, u_2\Big]^T = \Big[x_{top}(t), \theta_{top}(t)\Big]^T$; x_1 is the axial displacement of the drill bit ($x_{bit}(t)$), x_2 is the axial velocity of the drill bit ($\dot{x}_{bit}(t)$), x_3 is the torsional displacement of the drill bit ($\theta_{bit}(t)$), x_4 is the torsional velocity of the drill bit ($\dot{\theta}_{bit}(t)$). K_a is the axial stiffness, C_a is the axial damping, M is the equivalent mass, K_t is the torsional stiffness, C_t is the torsional damping, I is the torsional equivalent inertia; u_1 and u_2 represent the axial and torsional displacements at the top drive, which are the selected control inputs in this chapter. In the drilling industry, the control inputs are often considered as the hook load F and top drive torque T. They can be produced by a local internal feedback controller of the top drive and hook load actuators to track the optimized u_1 and u_2.

$WOB\Big(x_2, x_4\Big)$ and $TOB\Big(x_2, x_4\Big)$ are the weight-on-bit (WOB, stands for the axial cut-

ting/resistance force on the bit) and torque-on-bit (TOB, represents the torsional cutting torque on the bit), which are nonlinear functions of the axial and torsional state variables and will be modeled in subsection 2.2.2. Since both $WOB\Big(x_2, x_4\Big)$ and $TOB\Big(x_2, x_4\Big)$ are dependent on the axial and torsional states, the axial and torsional dynamics of the drilling system are coupled at the bit (Fig. 2.2). Note that, a lower order drill string dynamics is adopted here for DP control optimization, while a higher-order model will be used for the control validation in the section 2.4.

2.2.2 Bit/Rock Interaction

$WOB\Big(x_2, x_4\Big)$ and $TOB\Big(x_2, x_4\Big)$ are the force and torque induced by the drill bit and rock interaction, which are subject to nonlinear and complex geo-mechanics. A widely used bit-rock interaction model for the PDC bit was developed by Detournay et al. [8] [77], in which experimental data are given to verify the efficacy of the model proposed. WOB and TOB are determined by decomposing into cutting components WOB_c and TOB_c and friction components WOB_f and TOB_f as:

$$\begin{cases} WOB(t) = WOB_c(t) + WOB_f(t) \\ TOB(t) = TOB_c(t) + TOB_f(t) \end{cases} \tag{2.2}$$

Both of them are dependent on the depth of cut of the drill bit d, which is the effective engaging area between the blade front face and the rock (Fig. 2.2).

The cutting components are dependent on the drilling depth of cut d as:

$$WOB_c(t) = \begin{cases} \zeta \cdot \epsilon \cdot a \cdot d(t) & \text{if } d(t) > 0 \\ 0 & \text{if } d(t) \leq 0 \end{cases} \tag{2.3}$$

$$TOB_c(t) = \begin{cases} \frac{1}{2} \cdot \epsilon \cdot a^2 \cdot d(t) & \text{if } d(t) > 0 \\ 0 & \text{if } d(t) \leq 0 \end{cases} \tag{2.4}$$

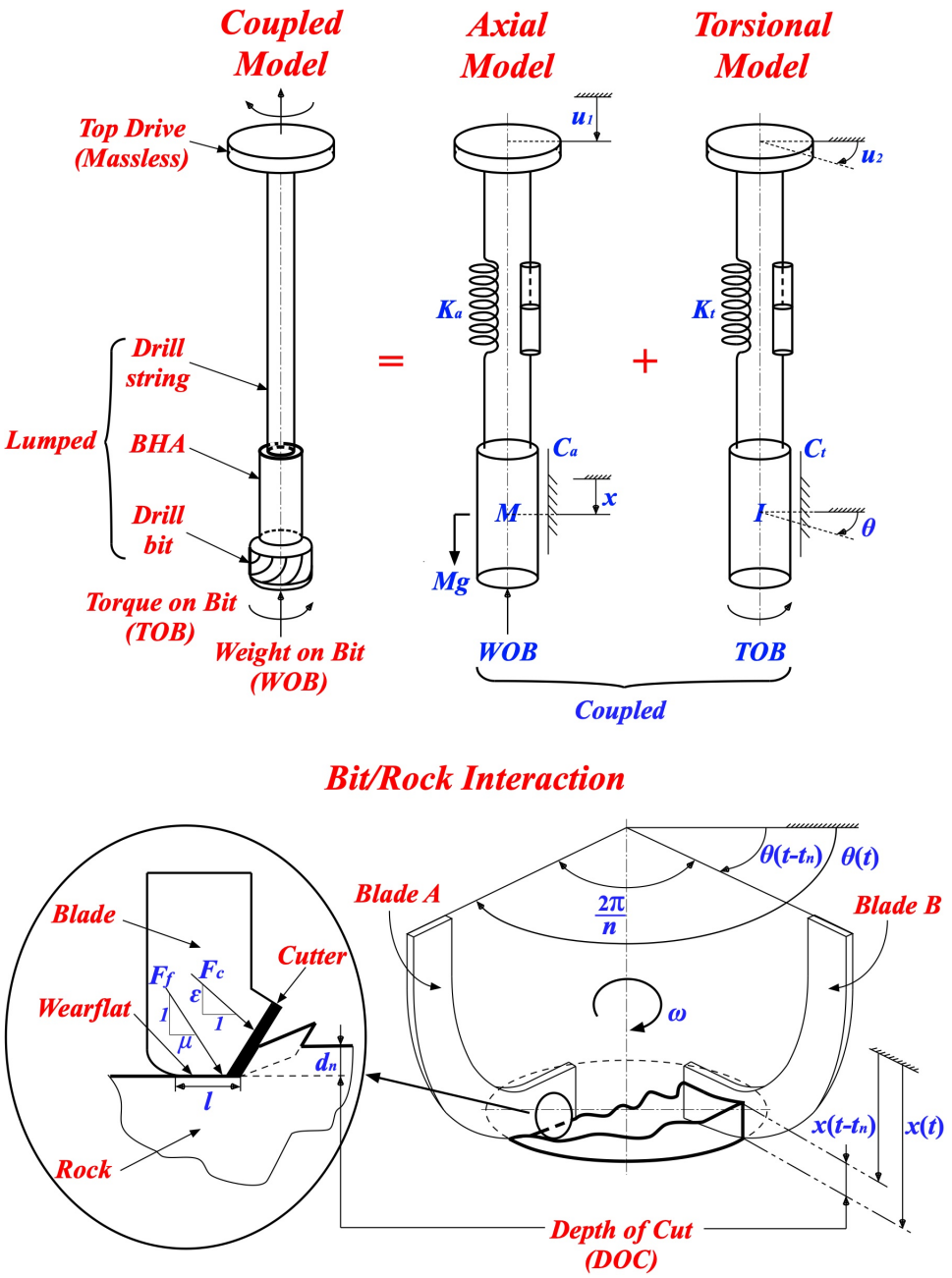

Figure 2.2 Axial-Torsional coupled model for the down-hole drilling system (reprinted with permission) [8] [5]

where a is the bit radius; ϵ is the intrinsic specific energy; $\zeta \in [0.5, 0.8]$ represents a constant to describe the bit geometry.

The frictional components of WOB and TOB are modeled as:

$$WOB_f(t) = \begin{cases} \sigma \cdot l \cdot a \cdot f(x_2(t)) & \text{if } d(t) > d^* \\ K_c \cdot d(t) & \text{if } 0 < d(t) \leq d^* \\ 0 & \text{if } d(t) \leq 0 \end{cases}$$

$$TOB_f(t) = \frac{1}{2} \cdot \mu \cdot \gamma \cdot a \cdot g(x_4(t)) \cdot WOB_f(t) \tag{2.5}$$

where σ is maximum contact pressure at the wear-flat interface; l is equivalent wear-flat length; K_c is linear contact stiffness; d^* is the threshold of the depth of cut; δ is the geometry parameter of the bit. $f(x_2)$ and $g(x_4)$ are functions of x_2 and x_4 and listed as follows:

$$f(x_2(t)) = \frac{1}{1 + \exp^{(a_1 x_2(t) + b_1)}} \tag{2.6}$$

$$g(x_4(t)) = \tanh(a_2 x_4(t) + b_2) \tag{2.7}$$

where the values of a_1, b_1, a_2, and b_2 are chosen as -20×10^4, -1.5, 70×10^3, 2 respectively [3]. μ represents the coefficient of friction at the wear-flat rock interface:

$$\mu = \mu_c + (\mu_s - \mu_c) \exp^{-\frac{\gamma_b}{v_f}|x_2(t)|} \tag{2.8}$$

where μ_c is the is the Coulomb friction coefficient; μ_s is the static friction coefficient [113].

The depth of cut is determined by the difference between the axial displacement of the blade considered (Blade B in Fig. 2.2, for example) and the height of the rock surface created by the adjacent blade (Blade A, for example). Mathematically it can be written as:

$$\begin{cases} d(t) = n \cdot d_n(t) \\ d_n(t) = x_{bit}(t) - x_{bit}(t - t_n) \end{cases} \tag{2.9}$$

where n denotes the number of blades; $x_{bit}(t)$ represents the bit axial displacement at the current time t; $x_{bit}(t-t_n)$ is the bit axial displacement at time $(t-t_n)$, which is identical to the height of the rock surface created by the neighboring blade; the time delay term $(t-t_n)$ is the time when the neighboring blade (Blade A) was at the same torsional location as the blade considered (Blade B) in Fig. 2.2, which can be solved from:

$$\theta_{bit}(t) - \theta_{bit}(t-t_n) = \frac{2\pi}{n} \tag{2.10}$$

where $\theta_{bit}(t)$ represents the bit torsional displacement at time t; $\dot{\theta}_{bit}(t-t_n)$ is the bit torsional displacement at time $(t-t_n)$.

2.2.3 Bit Model Approximation

Once the time delay t_n is determined from Eq. (2.10), the drilling depth of cut d can be obtained from Eq. (2.9). However, directly using the time-delay Eq. (2.9) to determine the depth of cut can be a problem for the backward DP based optimization since the time-delay term $x(t-t_n)$ is unknown when DP calculation proceeds from the final states to states at time t (calculation is conducted in a backward fashion). Furthermore, as will be explained in section 2.3, the computationally efficient algorithm proposed in this chapter requires the system dynamics to be partially invertible, while having a time-delay term in the system dynamics can make this requirement hard to meet. To address that, we approximate the depth of cut in Eq. (2.9) as:

$$d(t) = 2\pi \frac{\dot{x}_{bit}(t)}{\dot{\theta}_{bit}(t)} = 2\pi \frac{x_2(t)}{x_4(t)} \tag{2.11}$$

This approximation essentially means that the total depth of cut is equal to the axial bit blade displacement when the bit rotates a full circle. The efficacy of using this approximation to model the depth of cut can be verified in Fig. 2.3 and Fig. 2.4, which shows comparison between the model using Eqs. (2.9, 2.10) and that using Eq. (2.11). As long as $\dot{\theta}_{bit}(t)$ is

away from zero, this approximation is sufficiently accurate [2] [8] [76] [52], otherwise it may cause singularity. As shown in Fig. 2.3 and Fig. 2.4, the histogram of errors between two depth of cut models also demonstrates the efficacy of this approximation. Since the desired operation range of the drilling torsional velocity is much away from zero, this model can be used in the DP computation.

2.3 Optimal Control Design

In this section, the optimal control problem is formulated. Given the nonlinear axial-torsional coupled drilling dynamics, it is hard to directly achieve an analytical solution. Thus we resolve this optimization problem based on numerical Dynamic Programming [107].

2.3.1 System Model Discretization

A discrete dynamics model is needed for DP computation. The drilling system dynamics model (Eq. (2.1)) can be discretized as:

$$\begin{cases} x_1(k+1) = x_1(k) + x_2(k)\Delta t \\ x_2(k+1) = x_2(k) + \Big[-\dfrac{C_a}{M}x_2(k) - \dfrac{K_a}{M}x_1(k) + \dfrac{K_a}{M}u_1(k) + \dfrac{Mg - WOB(x_2, x_4)}{M} \Big]\Delta t \\ x_3(k+1) = x_3(k) + x_4(k)\Delta t \\ x_4(k+1) = x_4(k) + \Big[-\dfrac{C_t}{I}x_4(k) - \dfrac{K_t}{I}x_3(k) + \dfrac{K_t}{I}u_2(k) - \dfrac{TOB(x_2, x_4)}{I} \Big]\Delta t \end{cases} \tag{2.12}$$

where Δt is the sampling time interval. T is the total time considered in the optimization. $N = T/\Delta t$ is the total steps of sampling.

The cost function for the drilling process optimization is defined in Eq. (2.13). The first term is to enforce the bit axial velocity close to the mean axial velocity v_m, which can minimize the overshoot of x_2 and attenuate the bit velocity oscillation. The second term ensures that the bit torsional velocity x_4 can be close to the average torsional velocity w_m and be smooth. The third term and the fourth term are to make sure that the drill bit reach

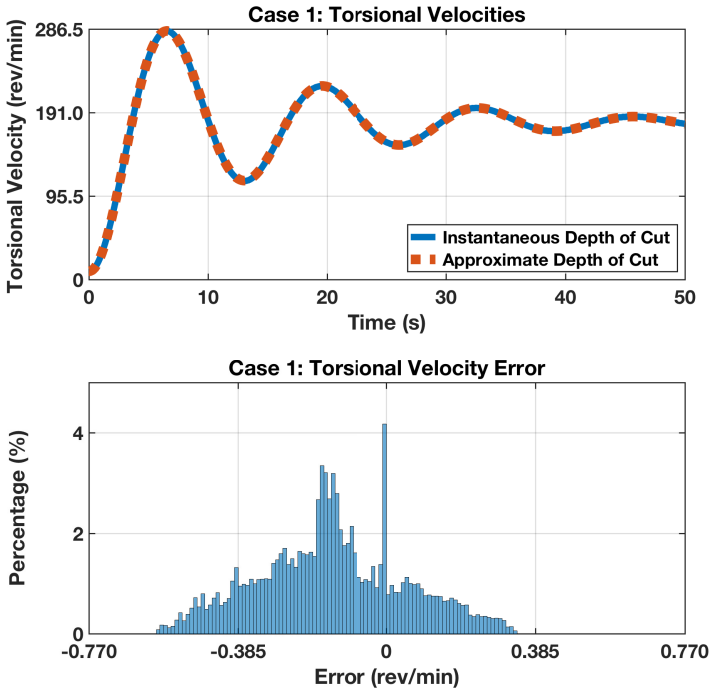

Figure 2.3 Case 1: comparison between model using time-delay based depth of cut and that with the approximated depth of cut

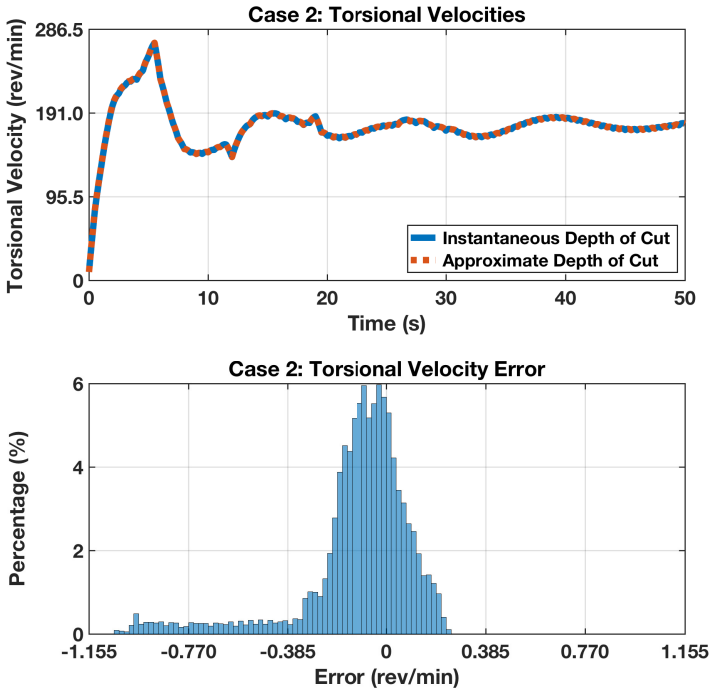

Figure 2.4 Case 2: comparison between model using time-delay based depth of cut and that with the approximated depth of cut

the final desired velocity (v_d and w_d) in both axial and torsional directions.

$$g(\boldsymbol{x}) = \lambda_1 \sum_{k=0}^{N-1} [x_2(k) - v_m]^2 \Delta t + \lambda_2 \sum_{k=0}^{N-1} [x_4(k) - w_m]^2 \Delta t + \lambda_3 [x_2(N) - v_d]^2 + \lambda_4 [x_4(N) - w_d]^2 \tag{2.13}$$

where λ_1, λ_2, λ_3, λ_4 are the weighting factors. v_d and w_d are desired bit velocity in axial and torsional directions.

Therefore, the control problem is to find an optimal set of inputs $\boldsymbol{u}$ to minimize the cost function above $g(\boldsymbol{x})$:

$$J(\boldsymbol{x}) = \min_{[\boldsymbol{u}] \in \boldsymbol{U_f}} g(\boldsymbol{x}) \tag{2.14}$$

where $\boldsymbol{x}$ denotes all states at all time steps. $\boldsymbol{u} = [u_1, u_2]$ stands for control inputs. $\boldsymbol{U_f}$ represents all feasible control input sets.

2.3.2 Control Optimization Using the Computationally Efficient Dynamic Programming

In this subsection, the standard Dynamic Programming is first briefly reviewed. We show that it is hard to directly apply the standard DP for our problem. Then we will present a computationally efficient approach by leveraging the partial invertibility [110] of the approximated drilling dynamics model proposed in section 2.2.

The standard DP resolves an optimization problem by searching a state trajectory connecting the final states with the initial states that can minimize the given cost function. This is usually conducted in a backward fashion, starting from the final state to initial conditions. First, the entire state space is gridded to generate a number of candidate states for each time step k. For example, as shown in Fig. 2.5, for our 4^{th} order drilling dynamics model, each candidate state is a combination of grids of x_1, x_2, x_3, and x_4. If x_1, x_2, x_3, and x_4 are each gridded into L sets of values, then the total number of candidate states for step k will

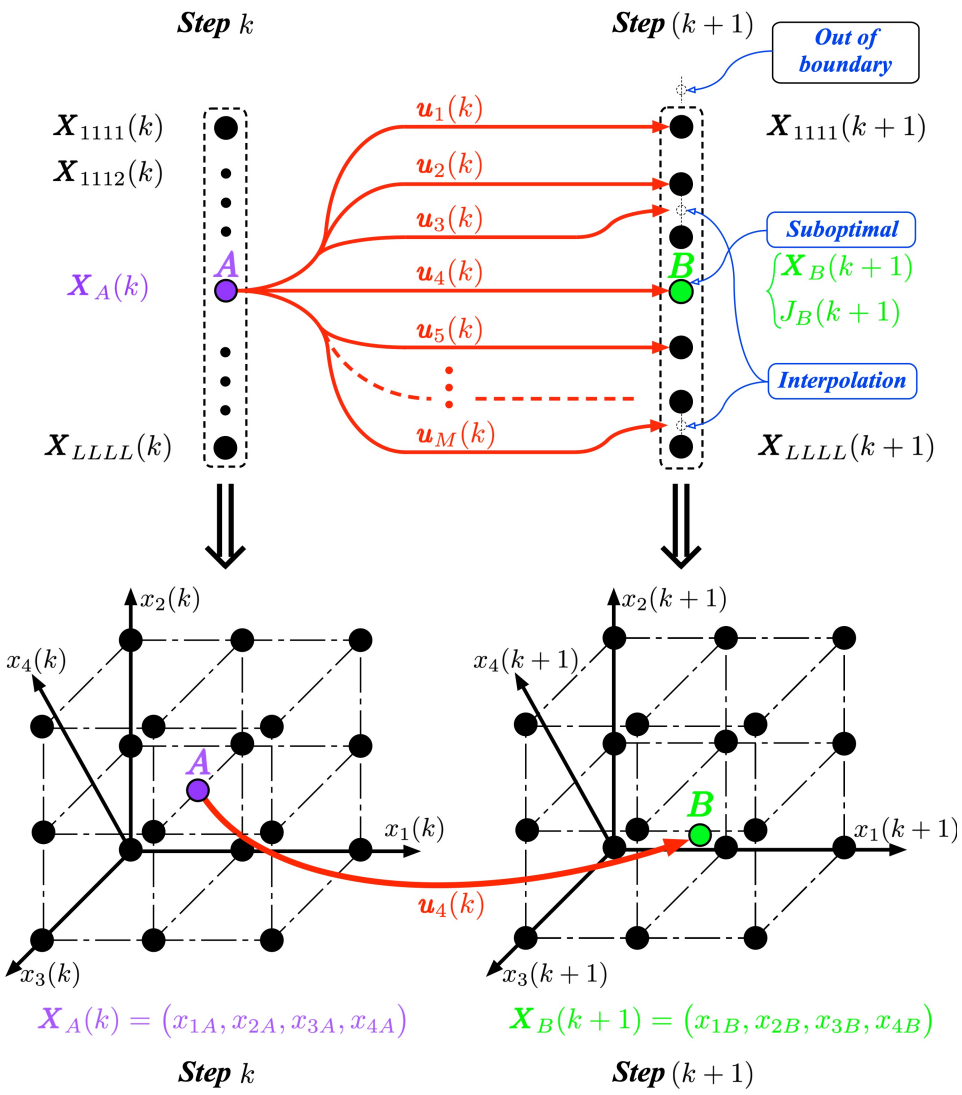

Figure 2.5 Conventional dynamic programming state space gridding

be $L \times L \times L \times L$. Then cost value is assigned to each candidate state, which is achieved based on the cost function Eq. (2.13) and the cost value of its corresponding state at the previous step. Specifically, at step k, each candidate state (node A, for example) is related to a candidate state at the previous step (step $k+1$ for backward DP). This correspondence is built by finding admissible control input that can project the candidate state (node A) to a candidate state at step $k+1$ with minimum cost. This is usually achieved by having a set of discretized control inputs u_1, u_2, ... within the admissible range project node A to step $k+1$,

i.e., $X(k+1) = F[X_A(k), u]$. Since the cost values for the candidate states at $k+1$ were obtained at the previous DP step, the cost value for each input projection can be obtained and the one with the lowest cost value is assigned to node A. This method of projection has three issues. First, the projection to step $k+1$ may not exactly lie on the pre-determined candidate states at $k+1$, and thus interpolation is usually needed to determine the cost value of this projection. This can result in an error of interpolation and can propagate through DP computation. Second, some projections can be out of the boundary of the state space, and thus it is a waste of computational resources to compute these projections. Third, most importantly, the projections rely on the forward dynamics model Eq. (2.12). The stiffness of the system requires the sampling time interval Δt to be very small (0.0005 sec) to make the discrete system stable. This also requires DP to have a large number of steps ($T/\Delta t$), which will be computationally intensive.

To address those issues, we propose a different method to generate and assign cost values to the candidate states, based on the specific drilling dynamics structure. Note that, enabled by the drill bit dynamics approximation in subsection 2.2.3, the discrete drilling system dynamics (Eq. (2.12)) can be partially inverted as:

$$\begin{cases} x_1(k) = x_1(k+1) - x_2(k)\Delta t \\ x_3(k) = x_3(k+1) - x_4(k)\Delta t \\ u_1(k) = \left(\dfrac{WOB(x_2, x_4) - Mg}{K_a} + x_1(k) + \dfrac{C_a}{K_a}x_2(k) - \dfrac{M}{K_a \Delta t}x_2(k) + \dfrac{M}{K_a \Delta t}x_2(k+1)\right) \\ u_2(k) = \left(\dfrac{TOB(x_2, x_4)}{K_t} + x_3(k) + \dfrac{C_t}{K_t}x_4(k) - \dfrac{I}{K_t \Delta t}x_4(k) + \dfrac{I}{K_t \Delta t}x_4(k+1)\right) \end{cases} \tag{2.15}$$

This partial inversion will not be feasible if directly using Eq. (2.9) without the depth of cut approximation as Eq. (2.11), since a time delay term is needed in Eq. (2.9), which is not known at step k as DP is computed in a backward fashion. We can denote this partially

inverted dynamics as:

$$[x_1(k), x_3(k), u_1(k), u_2(k)] = R\,[x_1(k+1), x_2(k+1), x_3(k+1), x_4(k+1), x_2(k), x_4(k)] \tag{2.16}$$

This indicates that x_1 and x_3 at current step k can be determined if $x_1(k+1)$, $x_2(k+1)$, $x_3(k+1)$, $x_4(k+1)$, $x_1(k)$ and $x_3(k)$ are given. Thus, instead of pre-determining the candidate state values as a combination of grids of x_1, x_2, x_3, and x_4, we only specify grids values for x_2 and x_4 at step k. For x_1 and x_3, we divide the planes of x_1 and x_3 into a number of regions (Fig. 2.6). At step k of the DP computation, since all the candidate state values at previous step $k+1$ are known, the values of $x_2(k)$ and $x_4(k)$ are calculated based on the mapping R (Eq. (2.16)). If the calculated $x_2(k)$ and $x_4(k)$ lie in any pre-determined region, then a candidate state for that region can be specified. If multiple mappings fall into the same region, then the mapping/projection with the lowest cost value is recorded. In this way, the candidate states at step k can be generated, and they can be connected with a candidate state at step $k+1$ as well. Thus, the cost value of the candidate states at step k can be directly determined.

This method has two benefits compared with standard DP. First, interpolation is not needed when having candidate states at step k connected with those at step $k+1$, which mitigates the optimization error. Second, most importantly, the partially inverted drilling dynamics model requires much less sampling steps to be stable. As shown in Fig. 2.7, to generate the same simulation result, the sampling interval for the partially inverted model is 0.5 sec, while that for the forward model needs to be smaller than 0.05 sec. Figure 2.8 is also given to demonstrate this phenomenon. It shows the rise of modeling error when the sampling time interval increases for the forward model (we limit the range of the sampling time interval shown in this plot due to the wide range of the error magnitude). It can also be seen that the modeling error is still large (note the vertical coordinate is in the log scale)

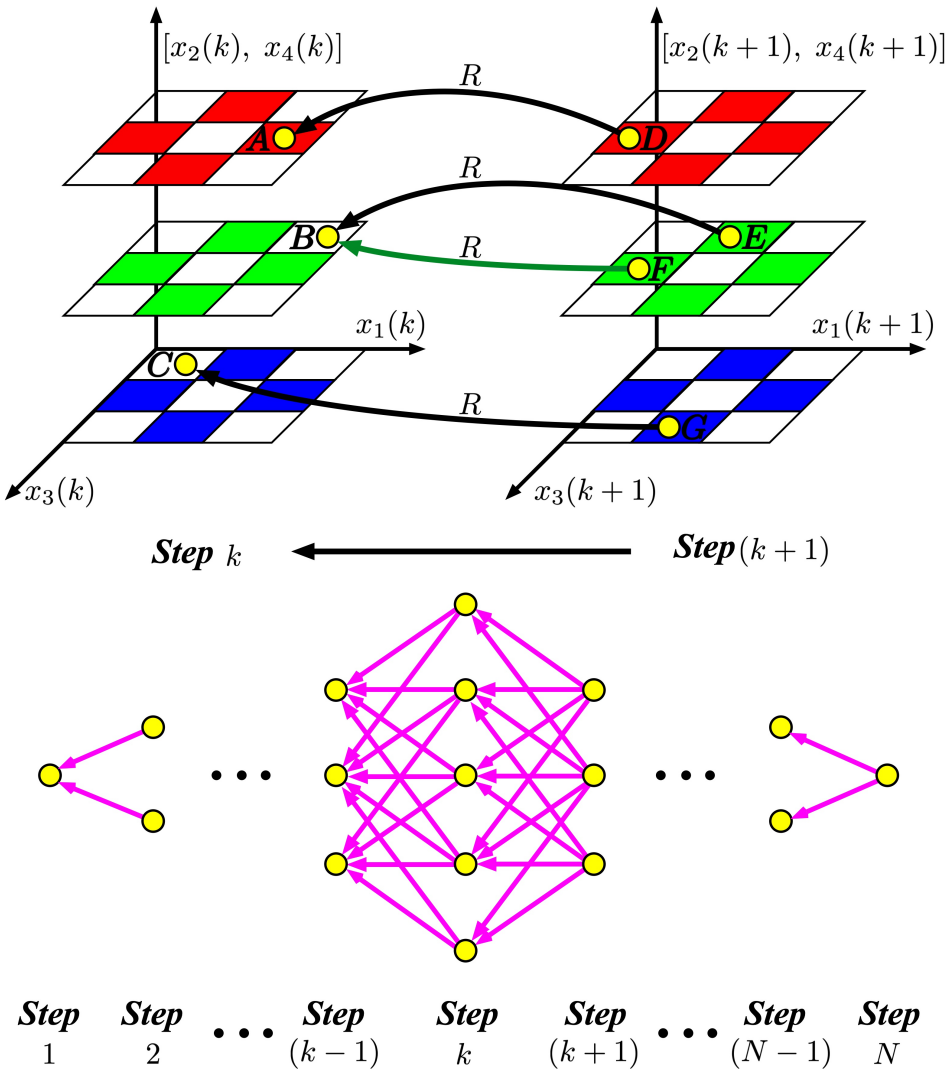

Figure 2.6 Computationally efficient dynamic programming state space gridding

for the forward model even if the sampling time interval is at 100 ms. This fact can also be verified by checking the eigenvalues of the Jacobian matrices of the two dynamics models. Note that, although not usable in regular dynamics simulation, the partial inverse model can be used in Dynamic Programming, since the computation is going backward and the states' values of step $k+1$ are known for DP operation at step k. This significantly reduces the DP computation time, and make this a more viable approach for efficient pre-drilling planning or even on-line control optimization.

Suppose that at step k, the total number of grids we pre-determined for $x_2(k)$ and $x_4(k)$

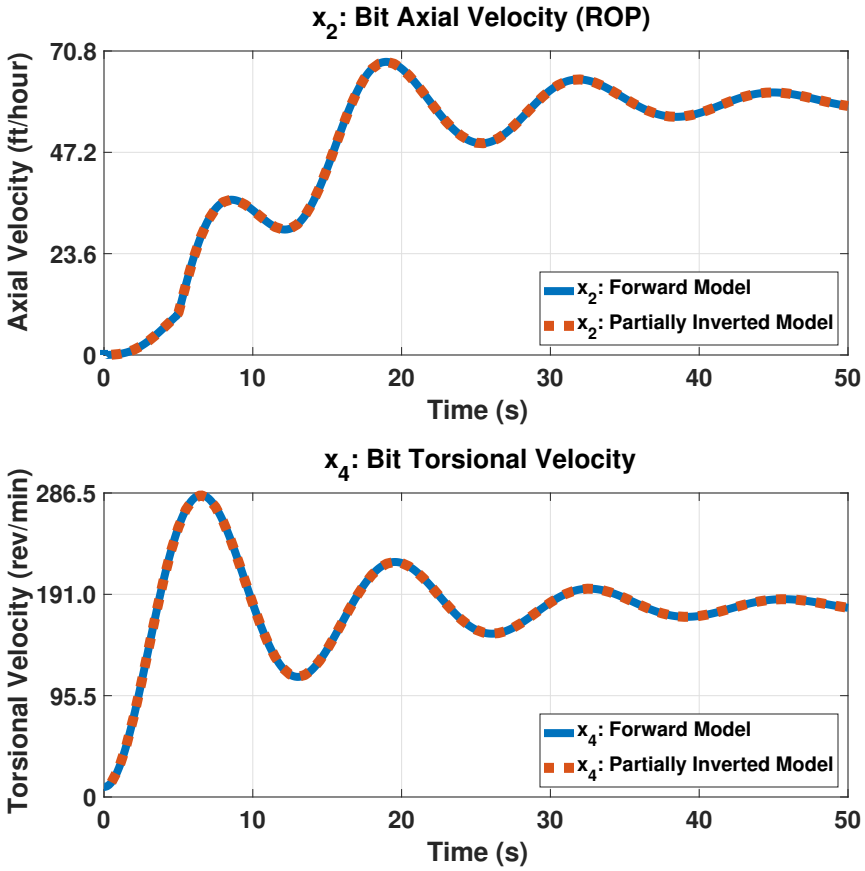

Figure 2.7 Forward model versus partially inverted model. The partially inverted model needs much less sampling rate compared with forward model.

is $L_2 \times L_4$ (Fig. 2.6). Then the algorithm at step k can be summarized as:

Step k^{th}, $h = 0$ **; for** $1 \leq i \leq L_2(k)$; $1 \leq j \leq L_4(k)$; $1 \leq m \leq L_{k+1}$;

$$[x_1(k), x_3(k), u_1(k), u_2(k)] = R\left[\boldsymbol{x}^m(k+1), x_2^i(k), x_4^j(k)\right] \tag{2.17}$$

$$\boldsymbol{x}_{temp}^h(k) = \left[x_1(k), x_2^i(k), x_3(k), x_4^j(k)\right] \tag{2.18}$$

$$index_1 = round(x_1(k)/L_1(k)) \tag{2.19}$$

$$index_3 = round(x_3(k)/L_3(k)) \tag{2.20}$$

$$\text{If} \quad node(index_1, i, index_3, j) = 0$$

$$J_{temp} =$$

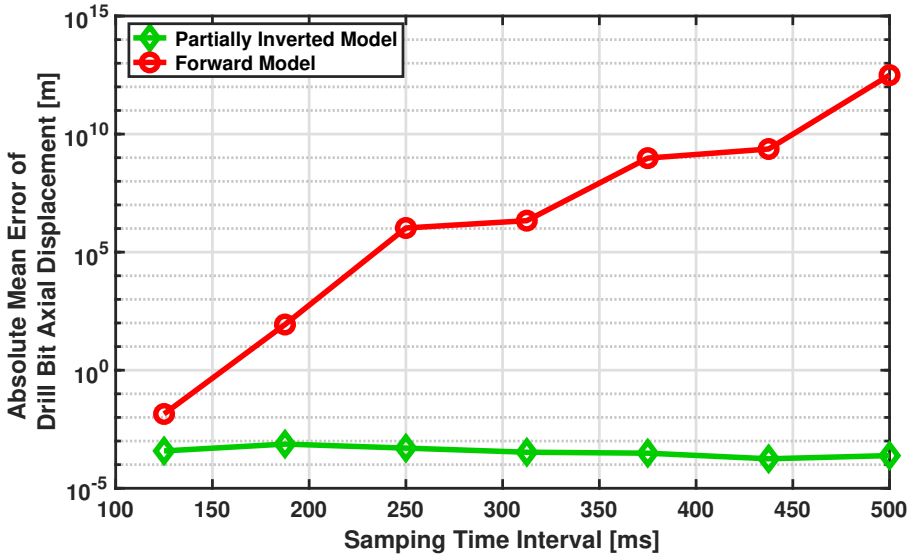

Figure 2.8 Model accuracy of the partially inverted model and forward model versus sampling rate.

$$\lambda_1\left[x_2^i(k) - v_m\right]^2 + \lambda_2\left[x_4^j(k) - w_m\right]^2 \tag{2.21}$$

$$h = h + 1 \tag{2.22}$$

If $node(index_1, i, index_3, j) \neq 0$

If $J_{temp} < J_k\left[\boldsymbol{x}_{temp}^h(k)\right]$

$$J_k\left[\boldsymbol{x}_{temp}^h(k)\right] = J_{temp} \tag{2.23}$$

$$\boldsymbol{x}(k) = \boldsymbol{x}_{temp}^h(k) \tag{2.24}$$

Once all the candidate states are assigned cost value, the state trajectory from initial step and final step with the minimum combined cost value can be identified, which leads to the optimal control inputs sequence $\left[\boldsymbol{u}(0), \boldsymbol{u}(1), \cdots, \boldsymbol{u}(N-1)\right]$.

2.3.3 Addressing Model Parameter Uncertainty in DP Searching

For the down-hole drilling process, some parameters of the dynamics model may be uncertain, either due to the complex working conditions or the changing rock formations. Being able to address these parameter uncertainties is also critical for DP based optimization.

In this subsection, the Mechanical (Intrinsic) Specific Energy (MSE) ϵ is considered as an example to study the robustness in DP searching. As a critical parameter in the bit/rock interaction, ϵ characterizes the energy needed to remove the unit volume of rocks. It highly depends on the down-hole rock property and is hard to know accurately in advance.

To account for the parameter variation, we can use a new cost function as the mean value of the cost values associated with the perturbed models:

$$J_{updated}(\boldsymbol{x}) = \frac{J_{pvm}(\boldsymbol{x}_{pvm}) + J(\boldsymbol{x}) + J_{pvp}(\boldsymbol{x}_{pvp})}{3} \tag{2.25}$$

where $J_{updated}$ denotes the updated cost function in the robust Dynamic Programming algorithm. $\boldsymbol{x}_{pvm}$ and J_{pvm} stand for the state and its cost function for a -10% parameter variation case. $\boldsymbol{x}_{pvp}$ and J_{pvp} represent the state and its cost function for a $+10\%$ parameter variation case. Using this cost function can have the Dynamic Programming search for a solution that is least affected by the uncertainty of the parameters.

2.4 Dynamic Programming Optimization Simulation Results

In this section, a series of simulations are conducted to validate the proposed approach. The simulation parameters are listed in Table 2.1. The optimized control inputs are first obtained using the computationally efficient Dynamic Programming algorithm. The optimal control solution is then validated using a higher-order dynamics model. The optimal control solution is also tested with a perturbed dynamics model using a range of perturbed ϵ values. Finally, the computational expenses of the optimization is tested to verify its efficacy for real-time solution.

As shown in Fig. 2.9 and Fig. 2.10, a set of optimized velocity trajectories of the drill bit is obtained using the proposed algorithm. The profile is enforced to stay close to its mean value except at the initial transient. This is to ensure the drill bit to be away from the stick-slip effect and also enable a smooth velocity profile to avoid much overshoot and vibration.

Table 2.1 Simulation parameters in customized DP optimization

Parameter	Value	Unit	Description
K_a	3.53×10^5	N/m	Axial stiffness
C_a	3.44×10^4	N·s/m	Axial damping
K_t	685.2	N·m/rad	Torsional stiffness
C_t	416.29	N·m·s/rad	Torsional damping
M	787215	kg	Mass
I	2863	kg·m^2	Moment of inertia
ϵ	77	MPa	Intrinsic specific energy
σ	45	MPa	Contact strength
ζ	0.64	-	Cutter face inclination
K_c	37.5	MN/m	Linear contact stiffness
$\gamma\mu$	0.7	-	-
δ	1.0	-	Geometry parameter of bit
a	0.15	m	Bit radius
n	5	-	Number of blades
l	3.6×10^{-3}	m	Total wear-flat length
d^*	1.2×10^{-3}	m	Threshold of the depth of cut
μ_c	0.5	-	Coulomb friction coefficient
μ_s	0.8	-	Static friction coefficient
γ_b	0.9	-	-
v_f	1.0	-	-

2.4.1 Optimal Control Validation Using a Higher Order Model

While the optimization is conducted based on a 4$^{\text{th}}$ order drilling dynamics model for computational efficiency purpose, to validate the control performance, we also test the optimized control inputs using a higher-order model (12$^{\text{th}}$ order) to demonstrate its efficacy. The higher order-model can capture the high-frequency components of the drilling dynamics compared with the 4$^{\text{th}}$ order model [114] [115]. It is composed of three main elements:

1. The top rotatory and upper drill pipes (M_1, I_1);
2. The lower drill pipes (M_2, I_2);
3. The drill collar and the bit (M_3, I_3).

The elasticity in the system is described by linear springs with axial stiffness, K_{a1} and K_{a2} , and torsional stiffness, K_{t1} and K_{t2}. The structural damping in the system is described

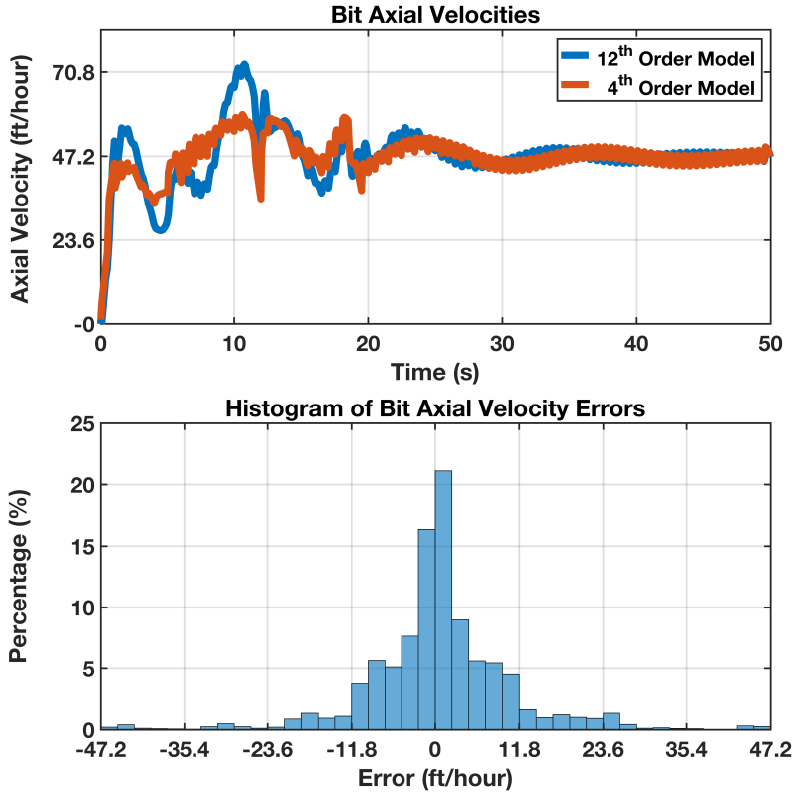

Figure 2.9 Controlled bit axial velocity using optimized control inputs from DP

by linear axial damping coefficients, C_{a1} and C_{a2} , and linear torsional damping coefficients, C_{t1} and C_{t2}.

$$M_1\ddot{x}_1(t) + C_{a1}\dot{x}_1(t) + K_{a1}x_1(t) = C_{a1}\dot{x}_2(t) + K_{a1}x_2(t) + M_1 g - F(t) \tag{2.26}$$

$$M_2\ddot{x}_2(t) + (C_{a1} + C_{a2})\dot{x}_2(t) + (K_{a1} + K_{a2})x_2(t)$$
$$= C_{a1}\dot{x}_1(t) + C_{a2}\dot{x}_3(t) + K_{a1}x_1(t) + K_{a2}x_3(t) + M_2 g \tag{2.27}$$

$$M_3\ddot{x}_3(t) + C_{a2}\dot{x}_3(t) + K_{a2}x_3(t) - M_3 g \tag{2.28}$$
$$= C_{a2}\dot{x}_2(t) + K_{a2}x_2(t) - WOB(\dot{x}_3(t), \dot{\theta}_3(t))$$

$$I_1\ddot{\theta}_1(t) + C_{t1}\dot{\theta}_1(t) + K_{t1}\theta_1(t) = C_{t1}\dot{\theta}_2(t) + K_{t1}\theta_2(t) + T(t) \tag{2.29}$$

$$I_2\ddot{\theta}_2(t) + (C_{t1} + C_{t2})\dot{\theta}_2(t) + (K_{t1} + K_{t2})\theta_2(t)$$
$$= C_{t1}\dot{\theta}_1(t) + C_{t2}\dot{\theta}_3(t) + K_{t1}\theta_1(t) + K_{t2}\theta_3(t) \tag{2.30}$$

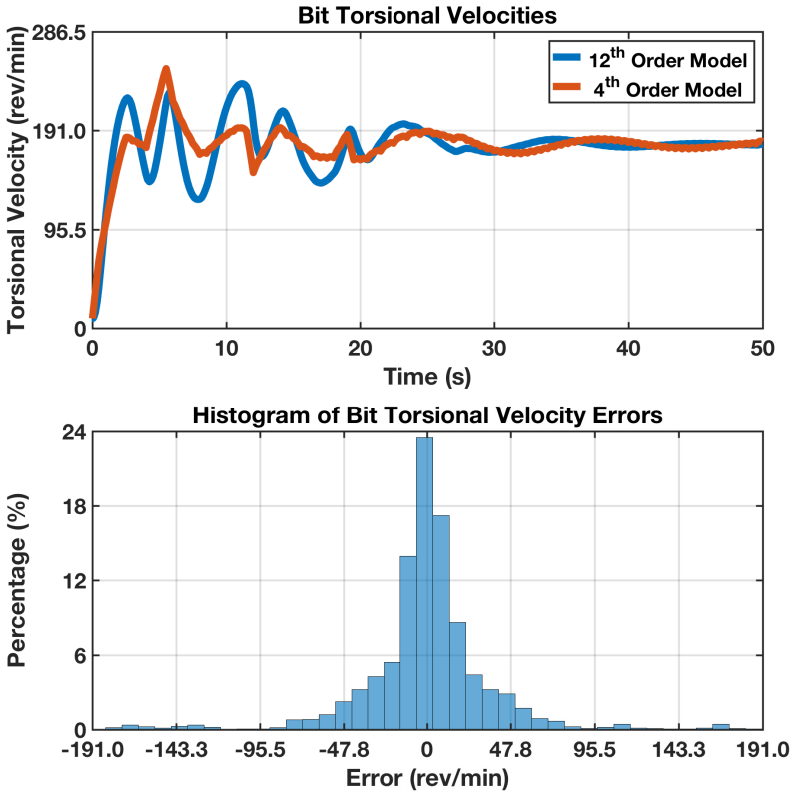

Figure 2.10 Controlled bit torsional velocity using optimized control inputs from DP

$$I_3\ddot{\theta}_3(t) + C_{t2}\dot{\theta}_3(t) + K_{t2}\theta_3(t) = C_{t2}\dot{\theta}_2(t) + K_{t2}\theta_2(t) - TOB(\dot{x}_3(t), \dot{\theta}_3(t)) \tag{2.31}$$

where F is the control axial force (the hook load), and T is the top drive torsional torque input.

Figure 2.9 and Figure 2.10 show the bit torsional velocity profiles using the DP inputs. Although the 12^{th} order model has a slightly different transient and more oscillations than the those of the 4^{th} order model, their general trends are very similar.

2.4.2 Parameter Variation Analysis

In this subsection, the control robustness is studied, by validating the control performance over a range of perturbed Intrinsic Specific Energy parameter ϵ of the bit-rock interaction. ϵ is perturbed from 150% to 250% of the nominal value 77 MPa.

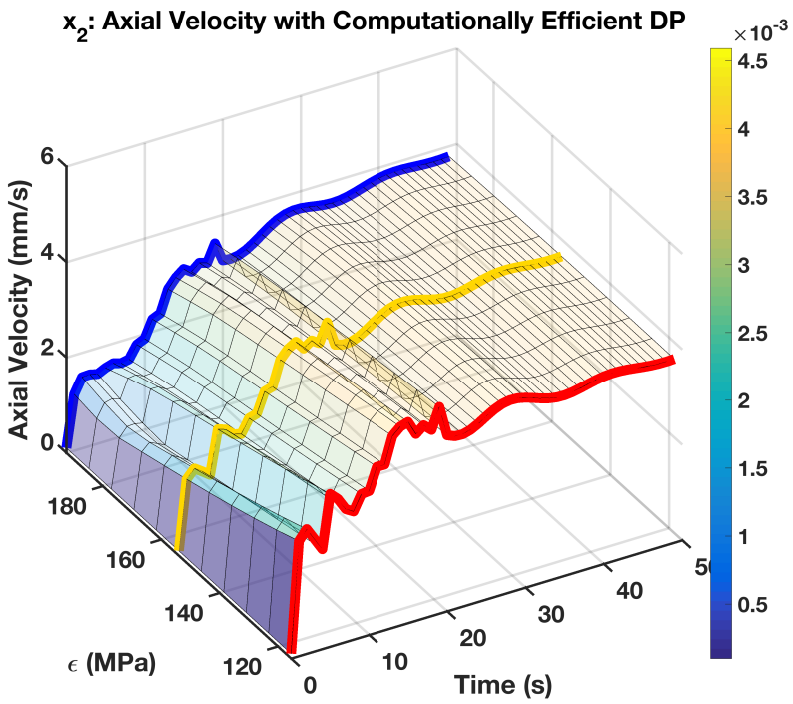

Figure 2.11 Bit axial velocity over varied parameter ϵ with computationally efficient dynamic programming optimized inputs

Figure 2.11 displays the controlled bit axial velocity with the perturbed ϵ. It can be seen that the effect on the axial velocity is monotonic with respect to the parameter variation. This fact is also observed when using the control inputs optimized with cost function considering the perturbation (Eq. (2.25)) (here we refer it as robust Dynamic Programming) as shown in Fig. 2.12. To further examine the effect of the perturbation, three perturbed cases are selected and shown on the same graph in Fig. 2.13 and Fig. 2.14. It can be seen that the control can still maintain the desired trend with the variation of ϵ. The control using the cost function considering the perturbation (Eq. (2.25)) shows a better performance in maintaining the perturbed trajectories close to a mean constant speed, while it tends to have a higher overshoot and more oscillations.

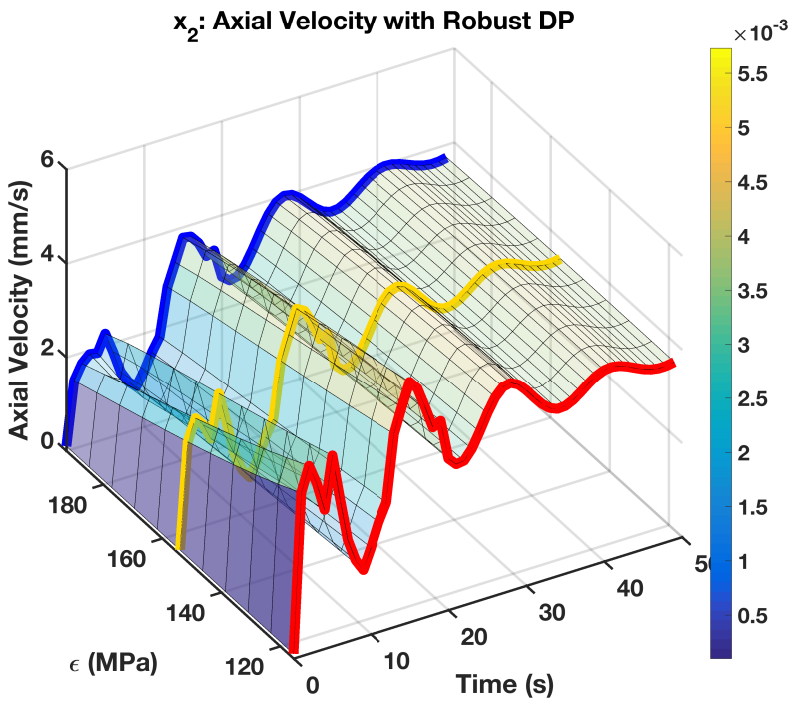

Figure 2.12 Bit axial velocity over varied parameter ϵ with robust dynamic programming optimized inputs

2.4.3 Computational Expense

The proposed optimization scheme can be used for efficient off-line synthesis, and can also be potentially implemented in a real-time scenario. To validate this, we test its computational efficiency as shown in Table 2.2. The computational time needed for the optimization is recorded for both a 20 sec drilling period and a 50 sec period. It can be seen that the computational time needed is almost proportional to the total drilling period considered. The computational expense has less dependence on the number of grids for x_1 and x_3, but more on that for x_2 and x_4. This is because we grid x_1 and x_3 into a number of regions, and will not exhaustively consider each gridded region if they are not reachable. This can significantly save the computational time.

From Fig. 2.15, it can also be seen that the calculation time much increases when considering perturbations in the cost function (here we denote it as robust Dynamic Program-

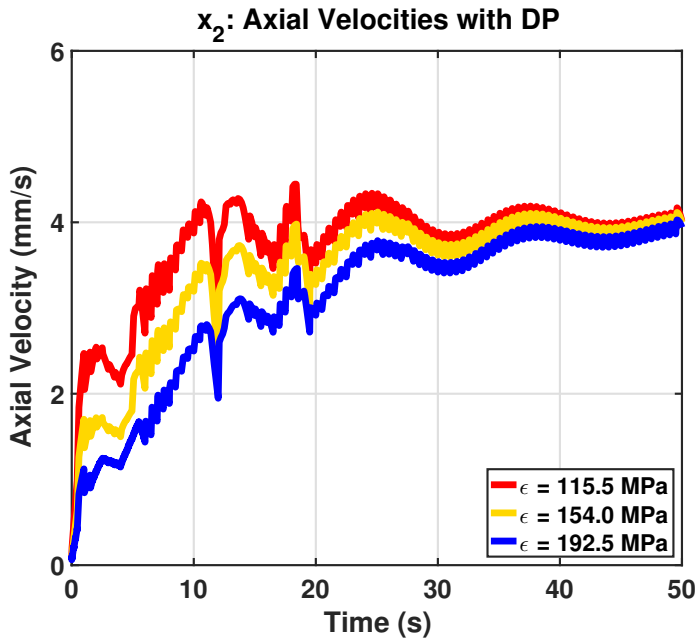

Figure 2.13 Bit axial speed over three perturbed ϵ (50, 150 and 200 percent perturbation) with computationally efficient dynamic programming optimized inputs

ming). This is because the robust Dynamic Programming needs to consider cost functions for a range of perturbed parameters. One of the focus for future work will be to study the balance between computational efficiency and level of robustness.

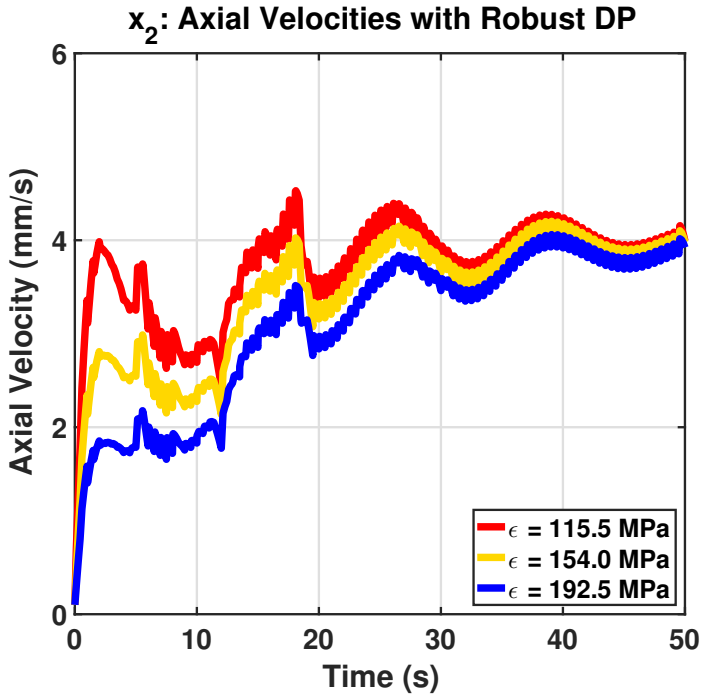

Figure 2.14 Bit axial speed over three perturbed ϵ (50, 150 and 200 percent perturbation) with robust dynamic programming optimized inputs

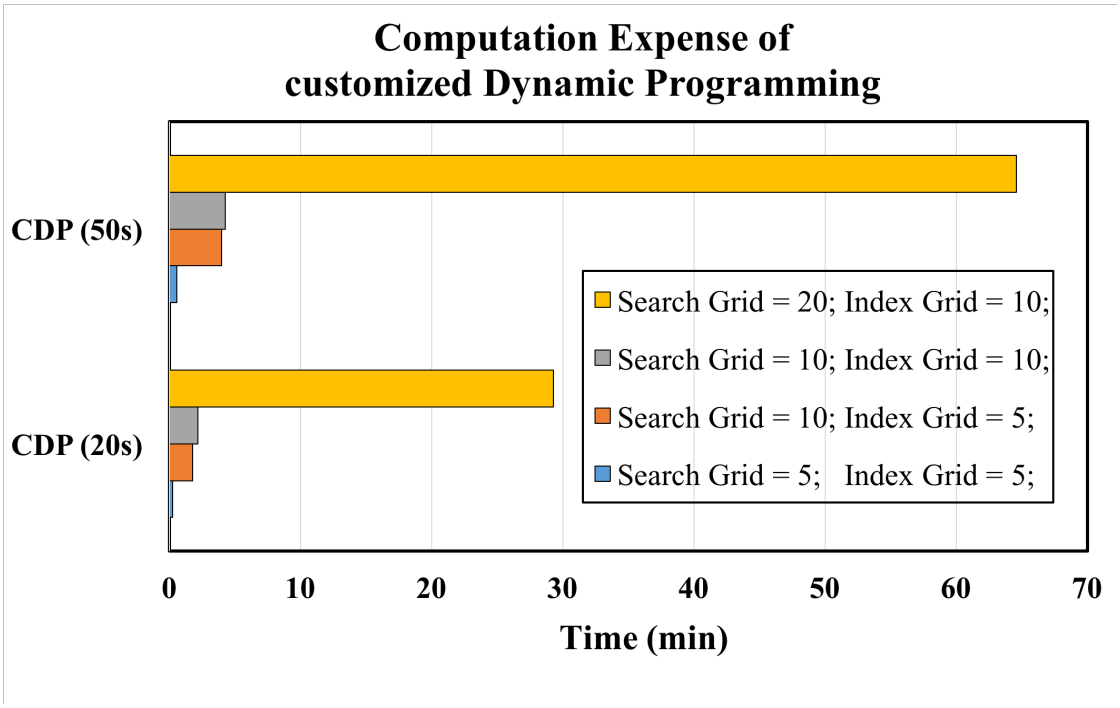

Figure 2.15 Computational expense of two DP approaches

2.5 Summary

This chapter presents the down-hole drilling process optimization using a computationally efficient Dynamic Programming algorithm. The proposed approach is enabled by an approximation of the drill bit model and a partial inversion of system dynamics. Compared with standard DP, it avoids interpolation error, saves computational resource by not considering non-reachable states, and does not need dense sampling between DP steps as a result of the partial inversion. For control validation, a higher-order model is used to verify the optimal control performance. Then the control robustness is also evaluated by having perturbations on the model parameters. The computational efficiency of the approach is tested as well, which demonstrates its potential application to either a pre-job planning or real-time drilling optimization scenario.

Table 2.2 Computational expense of customized dynamic programming

Type	**Search Grid** (x_2 **or** x_4)	**Index Grid** (x_1 **or** x_3)	**Calculation Time (min)**
Computationally Efficient Dynamic Programming (20 sec)	5	5	0.2232
	10	5	1.7482
	10	10	2.1657
	20	10	29.2758
Computationally Efficient Dynamic Programming (50 sec)	5	5	0.5643
	10	5	3.9637
	10	10	4.2417
	20	10	64.5777
Robust Dynamic Programming (20 sec)	5	5	7.7443
	10	5	30.6139
	10	10	32.0118
	20	10	170.5410
Robust Dynamic Programming (50 sec)	5	5	17.5077
	10	5	73.6872
	10	10	76.6379
	20	10	435.2070

3. CONTROL OF VERTICAL DOWN-HOLE DRILLING PROCESS USING AN EQUIVALENT INPUT DISTURBANCE APPROACH WITH A NEUTRAL-TYPE AXIAL-TORSIONAL COUPLED DYNAMICS MODEL*

While Chapter 2 provides a computationally efficient Dynamic Programming approach for the vertical drilling dynamics, the drawbacks using this proposed approach are obvious and can be stated in two manifolds. First, a simplified low-dimensional dynamics model is used in this DP scheme, which may not be able to accurately describe the drilling dynamics. Considering the large-axial-to-radius ratio of the drill string, one may use a higher-order lumped parameter model or a distributed parameter model to capture more transient details. Second, with a higher-order lumped parameter model, the proposed DP scheme can encounter the "*curse of dimensionality*," which restricts its applicability.

Therefore, this chapter proposed an equivalent input disturbance based approach to control the vertical down-hole drilling process using a distributed parameter model. To describe a drill string that is typically long with a large axial-to-radius ratio, a neutral type model is used to accurately capture the dynamics of this type of slender string structure. The axial-torsional coupling effect due to the bit-rock interaction is also included in the model. A new controller is then designed based on the coupled neutral model and the coupling effect is specifically addressed in the design. To address the uncertainty of the bit-rock interaction, the equivalent input disturbance method is used. A new Lyapunov-Krasovskii functional is proposed for the control design. To this end, a series of numerical simulation results are presented to demonstrate the effectiveness of the proposed control scheme.

*Reprinted with permission from "Drilling Control System Using an Equivalent Input Disturbance-Based Control With a Neutral-Type Axial-Torsional Coupled Dynamics Model," **C. Ke** and X. Song, *ASME Transactions on Journal of Dynamic Systems, Measurement and Control*, 141.12 (2019):121013, Copyright 2019 by ASME Publisher

3.1 Introduction

The down-hole drilling system is widely used in the oil and gas industry for well-bore creation and energy production. This system has several characteristics that differentiate its modeling from other engineering applications:

1. *Large axial-to-radius ratio*: the down-hole drilling system can extend to thousands of feet from the ground by connecting hundreds of drill pipes in series.

2. *Nonlinear nature at the bit/rock interaction interface*: the non-smooth characteristics in the bit/rock interaction can often lead to nonlinear behaviors such as bifurcations and periodic orbits (stick-slip and bit-bounce behaviors).

The stick-slip and bit-bounce behaviors are detrimental to the down-hole drilling system. Let alone the fact that PDC (polycrystalline diamond compact) bit is expensive, replacing a new bit requires a complete stop in the drilling operation, which can significantly decrease the production rate. Therefore, an effective and efficient control scheme to mitigate these vibrations is crucial. Moreover, control of drilling speed in the axial dimension is also important to ensure proper drilling rate of penetration. Given the above characteristics of the down-hole drilling system, to design such a control is not trivial, which motivates many of the recent studies on the modeling for the drill string and bit/rock interaction, as well as designing a valid control for the drilling system.

Figure 3.1 illustrates the schematic diagram of a vertical down-hole drilling system. This system normally consists of a power unit on surface, a long drill string (composed of a large number of inter-connected pipes) through the well-bore, and a down-hole drill bit for rock cutting. The main drilling power is generated on the surface, transmitting to the bit through the large scale drill string (pipe). There are two primary control inputs, the torsional torque from the heavy-duty motor to control the rock cutting force, and the axial force to regulate the bit axial motion.

By the dynamics model used for the drill string, current studies on the down-hole drilling

system can be classified into two categories: the lumped parameter system and the distributed parameter system. The lumped parameter system based control (modeling drill string as a number of spring mass damper systems) has been extensively studied and numerous methodologies have been proposed on the control design. This includes, but not limit to, H_∞ control [99], sliding mode control technique [113], back-stepping control [101], adaptive PID control scheme [116], and some optimization methods such as the genetic algorithm [102], Dynamic Programming [105] etc. Of these mentioned methodologies, some are based on torsional-only LPS dynamics [100] [117], and some are based on the axial-torsional coupled LPS dynamics [74] [111] [118] [119].

The distributed parameter system based control typically has the control design based on partial differential equations or models derived from PDEs. Compared with approaches based on a lumped parameter model, the distributed parameter system based method may capture more detailed high-frequency transient behavior of such a long string structure. For example, Saldivar. et al. worked on drilling control based on a neutral delay differential equations model [80], which is a type of DPS derived from PDEs. Different control methods are developed to suppress the torsional vibration, including the PID control [81], flatness based control [82], and linear matrix inequality based control [83], etc. However, the designed controllers mainly address torsional dynamics, without explicitly considering the control in the axial dimension. As shown in [8], the torsional and axial dynamics are indeed coupled in the drilling system, and thus the control design should explicitly consider the coupled dynamics to enable effective performance. Besides, controlling the drilling penetration rate also requires proper control in the axial dimension.

Thus, in this chapter, we will address the control for both the axial and torsional dimensions based on the NDDEs model with a coupled axial-torsional dynamics. To address the disturbance and uncertainty in the drill bit-rock interaction, we will use the equivalent input disturbance [120] [9] method. By proposing a new Lyapunov-Krasovskii functional, the stability of the NDDE system is ensured without the necessity of setting a tight boundary

constraint on the nonlinear external forces.

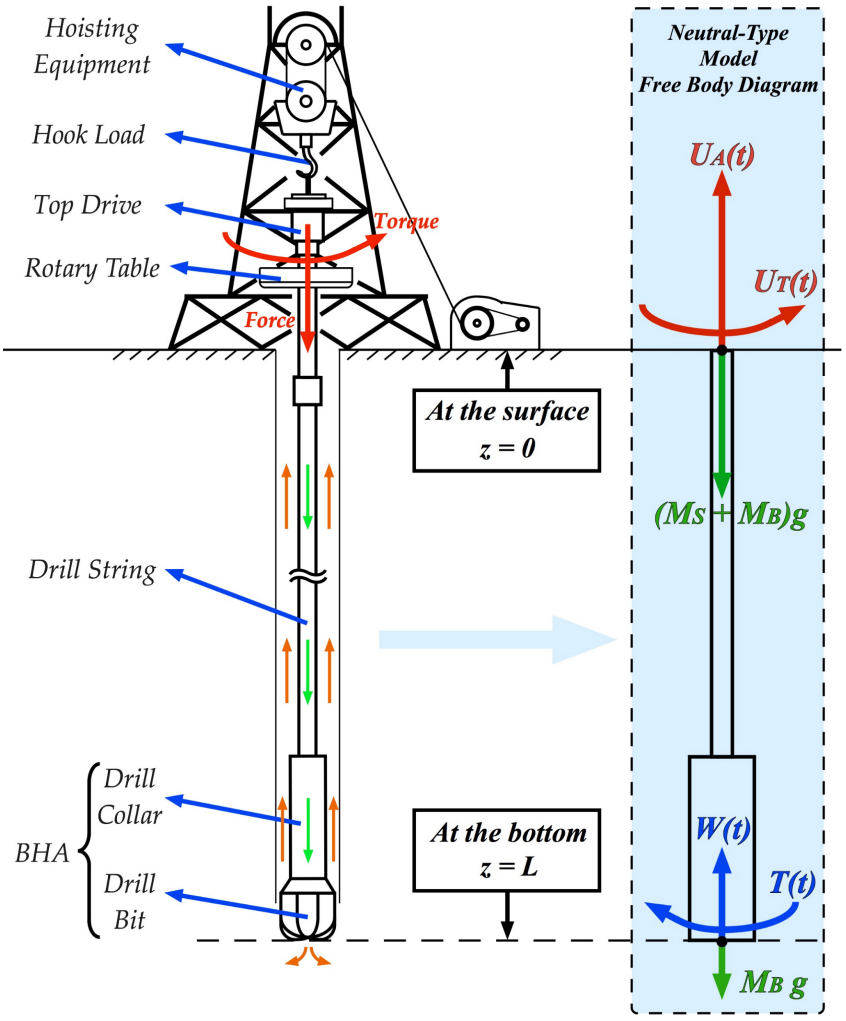

Figure 3.1 Freebody diagram of a vertical down-hole drilling system

The rest of this chapter is organized as follows. Section 3.2 presents the neutral-type axial-torsional coupled model for the down-hole drilling system, where the NDDE model for the drill string and bit/rock interaction model are described. Section 3.3 explains the equivalent input disturbance based control and its design structure. To determine the controller gain and observer gain, we propose a Lyapunov-Krasovskii functional in section 3.4 to prove the asymptotic stability of the overall system under feasible regions. In section 3.5, a series of

simulations are conducted to demonstrate the feasibility of the proposed EID based control scheme. The summary of this chapter is presented in section 3.6.

3.2 A Distributed Parameter Model for Vertical Down-Hole Drilling System

The vertical down-hole drilling dynamics model will be presented in this section. Firstly, to model the straight drill string, we introduce neutral delay differential equations and explain its derivation from partial differential equations. Then the bit/rock interaction model used in [119] [14] is presented to exhibit the axial-torsional coupling effect.

3.2.1 Neutral Type Model for Drill String

Drill string is the major component in the drilling system connecting the drilling power source on the surface with the down-hole drill bit. In this chapter, we assume a vertical well-bore drilling and neglect lateral motion since the axial/torsional dynamics are dominant. According to the wave propagation theory, an axial-torsional coupled distributed parameter model is presented in Eqs. (3.1-3.6) [81] [56] [121]:

$$\frac{\partial^2 Z}{\partial z^2}(z,t) = \frac{1}{c_A^2} \cdot \frac{\partial^2 Z}{\partial t^2}(z,t) \tag{3.1}$$

$$\frac{\partial^2 \Theta}{\partial z^2}(z,t) = \frac{1}{c_T^2} \cdot \frac{\partial^2 \Theta}{\partial t^2}(z,t) \tag{3.2}$$

subject to: $z \in [0, L], \ t \in [0, +\infty)$.

where Z and Θ denote axial and torsional displacement of the drilling pipe; L is the total length of the drill pipe; c_A and c_T denote axial and torsional wave speeds of the drill string:

$$c_A = \sqrt{\frac{E}{\rho}}, \quad c_T = \sqrt{\frac{G}{\rho}}$$

where E and G are Young's modulus and shear modulus; ρ is the density of the drill string.

At the bottom ($z = L$), the boundary conditions are:

$$EA\frac{\partial Z}{\partial z}(L,t) + M_B\frac{\partial^2 Z}{\partial t^2}(L,t) = -W(t) + M_B g \tag{3.3}$$

$$GJ\frac{\partial \Theta}{\partial z}(L,t) + I_B\frac{\partial^2 \Theta}{\partial t^2}(L,t) \quad = -T(t) \tag{3.4}$$

where A and J are cross-sectional area and geometric moment of inertia at the lowest part of the drill string; M_B and I_B are the mass and inertia of the lowest part of the drill string; $W(t)$ and $T(t)$ are the weight-on-bit and torque-on-bit induced by the bit/rock interaction, which are subject to nonlinear and complex geo-mechanics and will be described in subsection 3.2.2.

At the top ($z = 0$), the boundary conditions are:

$$EA\frac{\partial Z}{\partial z}(0,t) = \alpha_A\Big[\frac{\partial Z}{\partial t}(0,t) - U_A(t)\Big] + (M_S + M_B)g \tag{3.5}$$

$$GJ\frac{\partial \Theta}{\partial z}(0,t) = \alpha_T\Big[\frac{\partial \Theta}{\partial t}(0,t) - U_T(t)\Big] \tag{3.6}$$

where α_A and α_T stand for translational coefficient and angular coefficient; U_A and U_T represent axial and torsional control inputs on the ground; M_S is the mass of drill string.

By applying the *D'Alembert's* formula, hyperbolic partial differential equations above can be simplified into neutral delay differential equations [122] [123]. Assume that

$$\tau_1 = z/c_A,\ \ \gamma_A = t + \tau_1,\ \ \eta_A = t - \tau_1,$$

$$\tau_2 = z/c_T,\ \ \gamma_T = t + \tau_2,\ \ \eta_T = t - \tau_2.$$

Then the general solution of undamped wave propagation equations can be obtained as:

$$Z(z,t) = \Phi_A(\gamma_A) + \Psi_A(\eta_A) \tag{3.7}$$

$$\Theta(z,t) = \Phi_T(\gamma_T) + \Psi_T(\eta_T) \tag{3.8}$$

where Φ_A and Ψ_A are arbitrary continuous real-valued functions, denoting axial upwards and downwards traveling waves; Φ_T and Ψ_T stand for torsional upwards and downwards traveling waves.

Substitute the Eqs. (3.7, 3.8) into distributed parameter system Eqs. (3.1, 3.2) and apply to their boundary conditions of Eqs. (3.3-3.6), we acquire the neutral delay differential equations as follows:

$$\begin{cases} \ddot{Z}^B(t) = \Gamma_1 \ddot{Z}^B(t-2\tau_1) - \Gamma_2 \dot{Z}^B(t) - \Gamma_1\Gamma_2 \dot{Z}^B(t-2\tau_1) \\ \qquad\qquad -\dfrac{W(t)}{M_B} + \dfrac{\Gamma_1}{M_B} W(t-2\tau_1) + \Gamma_3 U_A(t-\tau_1) - \dfrac{\Gamma_3 M_S g}{\alpha_A} \\ \ddot{\Theta}^B(t) = \Upsilon_1 \ddot{\Theta}^B(t-2\tau_2) - \Upsilon_2 \dot{\Theta}^B(t) - \Upsilon_1\Upsilon_2 \dot{\Theta}^B(t-2\tau_2) \\ \qquad\qquad -\dfrac{T(t)}{I_B} + \dfrac{\Upsilon_1}{I_B} T(t-2\tau_2) + \Upsilon_3 U_T(t-\tau_2) \end{cases} \tag{3.9}$$

where $Z^B(t)$ represents the bit axial displacement at the current time; $\Theta^B(t)$ represents the bit torsional displacement; coefficients $\Gamma_1, \Gamma_2, \Gamma_3, \Upsilon_1, \Upsilon_2, \Upsilon_3$ are:

$$\Gamma_1 = \frac{c_A\alpha_A - EA}{c_A\alpha_A + EA},\ \ \Gamma_2 = \frac{EA}{c_A M_B},\ \ \Gamma_3 = \frac{2\alpha_A EA}{M_B(c_A\alpha_A + EA)},$$
$$\Upsilon_1 = \frac{c_T\alpha_T - GJ}{c_T\alpha_T + GJ},\ \ \Upsilon_2 = \frac{GJ}{c_T I_B},\ \ \Upsilon_3 = \frac{2\alpha_T GJ}{I_B(c_T\alpha_T + GJ)}.$$

and delay terms are:

$$\tau_1 = L\sqrt{\frac{E}{\rho}},\ \ \tau_2 = L\sqrt{\frac{G}{\rho}}. \tag{3.10}$$

3.2.2 Bit/Rock Interaction Model

A widely used bit/rock interaction model for the PDC bit was developed by Detournay et al. [8], in which experimental data are given to verify the efficacy of the model. $W(t)$

and $T(t)$ are determined by decomposing them into cutting components $W_c(t)$ and $T_c(t)$ and frictional components $W_f(t)$ and $T_f(t)$.

For the sake of simplicity, we refer $W(t)$ and $T(t)$ as below:

$$\begin{cases} W(t) = W_f(t) + W_c(t) = \Big[\dfrac{\sigma l_w R_b}{1 + e^{\left(a_1 \dot{Z}^B(t) + b_1\right)}} + \zeta \epsilon R_b d_{oc}(t)\Big]\mathbb{H}(d_{oc}(t)) \\ T(t) \ = T_f(t) + T_c(t) = \dfrac{1}{2}\mu\sigma\delta l_w R_b^2 \dfrac{\tanh\left(a_2 \dot{\Theta}^B(t) + b_2\right)}{1 + e^{\left(a_1 \dot{Z}^B(t) + b_1\right)}}\mathbb{H}(d_{oc}(t)) + \dfrac{1}{2}\epsilon R_b^2 d_{oc}(t)\mathbb{H}(d_{oc}(t)) \end{cases} \tag{3.11}$$

where $\zeta \in [0.5,\ 0.8]$ represents a constant dependent on bit geometry; ϵ is the intrinsic specific energy; R_b is the bit radius; d_{oc} denotes the depth of cut; $\mathbb{H}$ represents the Heaviside function; σ is maximum contact pressure at the wear-flat interface; l_w is equivalent wear-flat length; μ represents the coefficient of friction at the wear-flat rock interface; δ is the geometric parameter of the bit; the values of a_1, b_1, a_2, and b_2 are chosen as -20×10^4, -1.5, 70×10^3, 2 respectively.

Both of $W(t)$ and $T(t)$ are dependent on the depth of cut of the drill bit $d_{oc}(t)$, which is the effective engaging area between the blade front face and the rock.

The depth of cut is determined by the difference of the axial displacement of the blade considered (Blade B in Fig. 3.2, for example) and the height of the rock surface created by the adjacent blade (Blade A, for example). Mathematically, it can be written as:

$$\begin{cases} d_{oc} = n \cdot \left(Z^B(t) - Z^B(t - t_n)\right) \\ \Theta^B(t) - \Theta^B(t - t_n) = \dfrac{2\pi}{n} \end{cases} \tag{3.12}$$

where n denotes the number of blades.

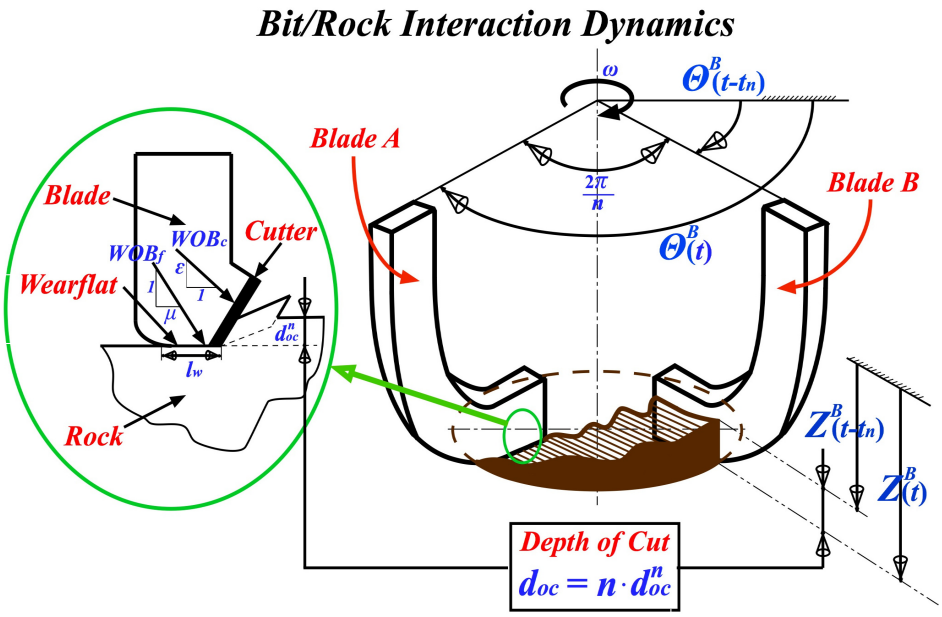

Figure 3.2 Axial-torsional coupled model for the down-hole drilling system (reprinted with permission) [8]

3.3 Equivalent Input Disturbance Based Controller Design

In this section, the state-space representation of the NDDE model derived from subsection 3.2.1 is presented. Then we construct the EID based control to suppress the axial-torsional coupled vibrations based on the NDDE model. The main idea is to estimate the unknown bit/rock interaction, and then incorporate them into the control inputs.

3.3.1 State-Space Representation for Neutral Delay Differential Equations

The system dynamics in Eq. (3.9) can be represented in the state-space as:

$$\begin{cases} \dot{\boldsymbol{x}}(t) = \boldsymbol{A}_0\boldsymbol{x}(t) + \boldsymbol{A}_1\boldsymbol{x}(t-h_1) + \boldsymbol{A}_2\boldsymbol{x}(t-h_2) + \boldsymbol{B}_d\boldsymbol{d}(t) \\ \qquad\quad +\boldsymbol{G}_1\dot{\boldsymbol{x}}(t-h_1) + \boldsymbol{G}_2\dot{\boldsymbol{x}}(t-h_2) + \boldsymbol{B}\boldsymbol{u}(t-\dfrac{h}{2}) \\ \boldsymbol{y}(t) = \boldsymbol{C}\boldsymbol{x}(t) \end{cases} \tag{3.13}$$

where $h_1 = 2\tau_1,\ h_2 = 2\tau_2$ are system time delays for the modeling accounting for wave propagation through the long drill string; $\boldsymbol{x}(t) = \begin{bmatrix} \dot{Z}^B(t) & \dot{\Theta}^B(t) \end{bmatrix}^T$ is the state variable; $\boldsymbol{d}(t)$ and $\boldsymbol{u}(t)$ represent the system external disturbance and control inputs:

$$\boldsymbol{d}(t) = \begin{bmatrix} -W(t) + \Gamma_1 W(t - h_1) \\ \\ -T(t) + \Upsilon_1 T(t - h_2) \end{bmatrix} \tag{3.14}$$

$$\boldsymbol{u}(t - \frac{h}{2}) = \begin{bmatrix} U_A(t - \dfrac{h_1}{2}) - M_S g \\ \\ U_T(t - \dfrac{h_2}{2}) \end{bmatrix} \tag{3.15}$$

where system matrices are:

$$\begin{aligned}
&\boldsymbol{A}_0 = \mathrm{diag}\begin{pmatrix} -\Gamma_2, & -\Upsilon_2 \end{pmatrix}, \quad \boldsymbol{B} = \mathrm{diag}\begin{pmatrix} \Gamma_3, & \Upsilon_3 \end{pmatrix}, \\
&\boldsymbol{B_d} = \mathrm{diag}\begin{pmatrix} 1/M_B, & 1/I_B \end{pmatrix}, \ \boldsymbol{C} = \mathrm{diag}\begin{pmatrix} 1, & 1 \end{pmatrix}, \\
&\boldsymbol{A}_1 = \mathrm{diag}\begin{pmatrix} -\Gamma_1\Gamma_2, & 0 \end{pmatrix}, \ \boldsymbol{G}_1 = \mathrm{diag}\begin{pmatrix} \Gamma_1, & 0 \end{pmatrix}, \\
&\boldsymbol{A}_2 = \mathrm{diag}\begin{pmatrix} 0, & -\Upsilon_1\Upsilon_2 \end{pmatrix}, \ \boldsymbol{G}_2 = \mathrm{diag}\begin{pmatrix} 0, & \Upsilon_1 \end{pmatrix}.
\end{aligned}$$

Since the characteristics equation of the closed-loop NDDE without input delay stays the same with the closed-loop NDDE with input delay [124], we follow similar procedures in [10] to neglect the input delay and facilitate the controller design in subsection 3.3.2. Therefore, the system state space equations are modified as:

$$\begin{cases} \dot{\boldsymbol{x}}(t) = \boldsymbol{A}_0\boldsymbol{x}(t) + \boldsymbol{A}_1\boldsymbol{x}(t - h_1) + \boldsymbol{A}_2\boldsymbol{x}(t - h_2) + \boldsymbol{B}_d\boldsymbol{d}(t) \\ \qquad\quad +\boldsymbol{G}_1\dot{\boldsymbol{x}}(t - h_1) + \boldsymbol{G}_2\dot{\boldsymbol{x}}(t - h_2) + \boldsymbol{B}\boldsymbol{u}(t) \\ \\ \boldsymbol{y}(t) = \boldsymbol{C}\boldsymbol{x}(t) \end{cases} \tag{3.16}$$

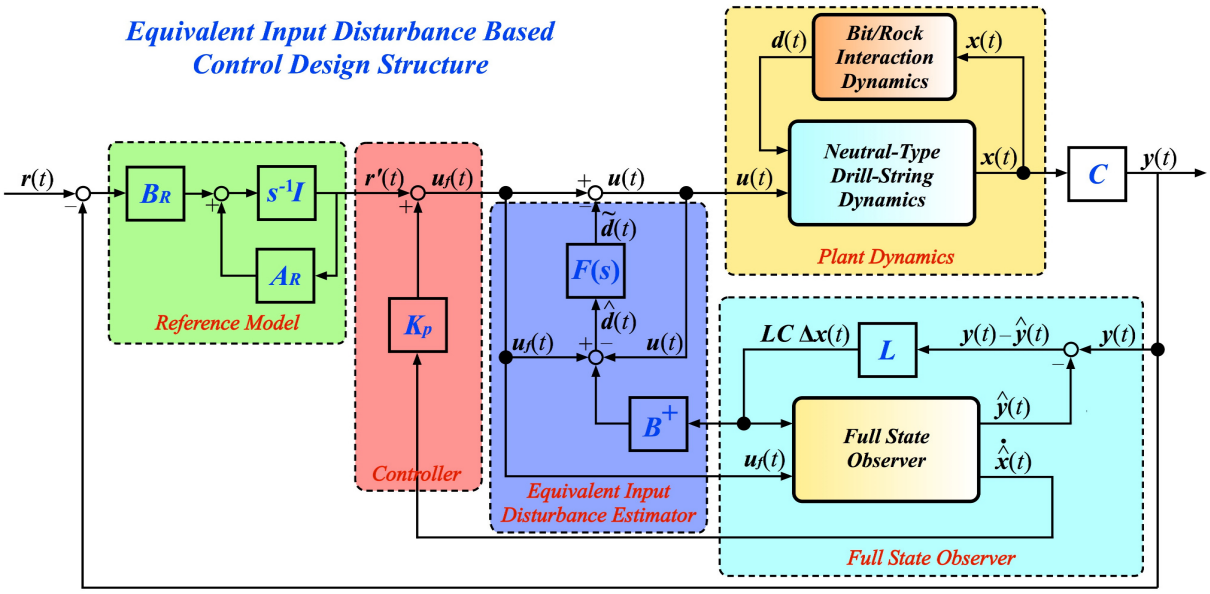

Figure 3.3 Control structure of equivalent input disturbance based control (reprinted with permission ©2011 IEEE) [9] [10]

Consider the equivalent input disturbance definition [9], suppose we have:

$$\boldsymbol{d}_e(t) = \boldsymbol{B}^{-1}\boldsymbol{B}_d\boldsymbol{d}(t) \tag{3.17}$$

Then Eq. (3.16) is transformed into:

$$\begin{cases} \dot{\boldsymbol{x}}(t) = \boldsymbol{A}_0\boldsymbol{x}(t) + \boldsymbol{A}_1\boldsymbol{x}(t-h_1) + \boldsymbol{A}_2\boldsymbol{x}(t-h_2) \\ \qquad\quad +\boldsymbol{G}_1\dot{\boldsymbol{x}}(t-h_1) + \boldsymbol{G}_2\dot{\boldsymbol{x}}(t-h_2) + \boldsymbol{B}\big[\boldsymbol{u}(t) + \boldsymbol{d}_e(t)\big] \\ \boldsymbol{y}(t) = \boldsymbol{C}\boldsymbol{x}(t) \end{cases} \tag{3.18}$$

where $\boldsymbol{d}_e(t)$ is the equivalent input disturbance vector of the external disturbance signal $\boldsymbol{d}(t)$.

3.3.2 Equivalent Input Disturbance Based Control Design

As shown in Fig. 3.3, the control system consists of a neutral-type down-hole drilling model, a reference trajectory internal model, a full state observer, a disturbance estimator,

and a feedback controller.

The state estimator is stated as below:

$$\begin{cases} \dot{\hat{\boldsymbol{x}}}(t) = \boldsymbol{A}_0\hat{\boldsymbol{x}}(t) + \boldsymbol{A}_1\hat{\boldsymbol{x}}(t-h_1) + \boldsymbol{A}_2\hat{\boldsymbol{x}}(t-h_2) + \boldsymbol{B}\boldsymbol{u}(t) \\ \qquad +\boldsymbol{G}_1\dot{\hat{\boldsymbol{x}}}(t-h_1) + \boldsymbol{G}_2\dot{\hat{\boldsymbol{x}}}(t-h_2) + \boldsymbol{L}\Big(\boldsymbol{y}(t) - \hat{\boldsymbol{y}}(t)\Big) \\ \hat{\boldsymbol{y}}(t) = \boldsymbol{C}\boldsymbol{x}(t) \end{cases} \tag{3.19}$$

where $\hat{\boldsymbol{x}}(t)$ is the observer state of $\boldsymbol{x}(t)$, $\boldsymbol{L}$ is the observer gain matrix.

The disturbance estimator $\hat{\boldsymbol{d}}(t)$ can be designed as:

$$\hat{\boldsymbol{d}}(t) = \boldsymbol{B}^{+}\boldsymbol{L}\boldsymbol{C}\Delta\boldsymbol{x}(t) + \boldsymbol{u}_f(t) - \boldsymbol{u}(t) \tag{3.20}$$

where

$$\boldsymbol{B}^{+} = \frac{\boldsymbol{B}^T}{\boldsymbol{B}^T\boldsymbol{B}}, \quad \Delta\boldsymbol{x}(t) = \boldsymbol{x}(t) - \hat{\boldsymbol{x}}(t)$$

To cancel out the measurement noise, a filter $\boldsymbol{F}(s)$ is designed to filter out the noise in $\hat{\boldsymbol{d}}(t)$:

$$\begin{cases} \dot{\boldsymbol{x}}_F(t) = \boldsymbol{A}_F\boldsymbol{x}_F(t) + \boldsymbol{B}_F(t)\hat{\boldsymbol{d}}(t) \\ \tilde{\boldsymbol{d}}(t) \ = \boldsymbol{C}_F\boldsymbol{x}_F(t) \end{cases} \tag{3.21}$$

where $\hat{\boldsymbol{x}}_F(t)$ is the filter state and $\tilde{\boldsymbol{d}}(t)$ represents the disturbance estimation after filtering.

Then the equivalent input disturbance based control can be designed as:

$$\boldsymbol{u}(t) = \boldsymbol{u}_f(t) - \tilde{\boldsymbol{d}}(t) \tag{3.22}$$

where $\boldsymbol{u}_f(t)$ is:

$$\boldsymbol{u}_f(t) = \boldsymbol{K}_p\hat{\boldsymbol{x}}(t) + \boldsymbol{r}'(t) \tag{3.23}$$

3.3.3 Closed-Loop System Dynamics

Therefore, the closed-loop system dynamics, including the state observer, system error dynamics, and filter dynamics, can be written as:

$$\begin{cases} \dot{\hat{\boldsymbol{x}}}(t) = \boldsymbol{A}_0\hat{\boldsymbol{x}}(t) + \boldsymbol{A}_1\hat{\boldsymbol{x}}(t-h_1) + \boldsymbol{A}_2\hat{\boldsymbol{x}}(t-h_2) + \boldsymbol{B}\boldsymbol{u}_f(t) \\ \qquad +\boldsymbol{G}_1\dot{\hat{\boldsymbol{x}}}(t-h_1) + \boldsymbol{G}_2\dot{\hat{\boldsymbol{x}}}(t-h_2) + \boldsymbol{L}\Big(\boldsymbol{y}(t) - \hat{\boldsymbol{y}}(t)\Big) \\ \Delta\dot{\boldsymbol{x}}(t) = (\boldsymbol{A}_0 - \boldsymbol{L}\boldsymbol{C})\Delta\boldsymbol{x}(t) + \boldsymbol{A}_1\Delta\boldsymbol{x}(t-h_1) + \boldsymbol{A}_2\Delta\boldsymbol{x}(t-h_2) \\ \qquad +\boldsymbol{G}_1\Delta\dot{\boldsymbol{x}}(t-h_1) + \boldsymbol{G}_2\Delta\dot{\boldsymbol{x}}(t-h_2) - \boldsymbol{B}\boldsymbol{C}_F\boldsymbol{x}_F(t) \\ \dot{\boldsymbol{x}}_F(t) = \boldsymbol{A}_F\boldsymbol{x}_F(t) + \boldsymbol{B}_F(t)\hat{\boldsymbol{d}}(t) \end{cases} \tag{3.24}$$

Define:

$$\boldsymbol{\xi}(t) = \begin{bmatrix} \hat{\boldsymbol{x}}^T(t) & \Delta\boldsymbol{x}^T(t) & \boldsymbol{x}_F^T(t) \end{bmatrix}^T$$

Then we have:

$$\dot{\boldsymbol{\xi}}(t) = \bar{\boldsymbol{A}}_0\boldsymbol{\xi}(t) + \bar{\boldsymbol{A}}_1\boldsymbol{\xi}(t-h_1) + \bar{\boldsymbol{A}}_2\boldsymbol{\xi}(t-h_2) + \bar{\boldsymbol{G}}_1\dot{\boldsymbol{\xi}}(t-h_1) + \bar{\boldsymbol{G}}_2\dot{\boldsymbol{\xi}}(t-h_2) \tag{3.25}$$

where the overall system matrices are:

$$\bar{\boldsymbol{A}}_0 = \begin{pmatrix} \boldsymbol{A}_0 + \boldsymbol{B}\boldsymbol{K}_p & \boldsymbol{L}\boldsymbol{C} & \boldsymbol{0} \\ \boldsymbol{0} & \boldsymbol{A}_0 - \boldsymbol{L}\boldsymbol{C} & -\boldsymbol{B}\boldsymbol{C}_F \\ \boldsymbol{0} & \boldsymbol{B}_F\boldsymbol{B}^+\boldsymbol{L}\boldsymbol{C} & \boldsymbol{A}_F + \boldsymbol{B}_F\boldsymbol{C}_F \end{pmatrix},$$

$$\bar{\boldsymbol{A}}_1 = \operatorname{diag}\Big(\boldsymbol{A}_1,\ \boldsymbol{A}_1,\ \boldsymbol{0}\Big),\ \bar{\boldsymbol{A}}_2 = \operatorname{diag}\Big(\boldsymbol{A}_2,\ \boldsymbol{A}_2,\ \boldsymbol{0}\Big),$$

$$\bar{\boldsymbol{G}}_1 = \operatorname{diag}\Big(\boldsymbol{G}_1,\ \boldsymbol{G}_1,\ \boldsymbol{0}\Big),\ \bar{\boldsymbol{G}}_2 = \operatorname{diag}\Big(\boldsymbol{G}_2,\ \boldsymbol{G}_2,\ \boldsymbol{0}\Big).$$

3.4 Closed-System Stability Analysis and Control Synthesis Using Lyapunov-Krasovskii Functional

In this section, the closed-loop system (Eq. (3.24)) stability will be analyzed using a new Lyapunov-Krasovskii functional, and the control synthesis can be achieved through a linear matrix inequality derived from the proposed Lyapunov-Krasovskii functional.

3.4.1 Preliminaries

Lemma 1. *Schur Complement [125]*

The following two expressions are equivalent:

$$\begin{bmatrix} \boldsymbol{Z}(x) & \boldsymbol{Y}(x) \\ \boldsymbol{Y}^T(x) & \boldsymbol{W}(x) \end{bmatrix} < 0 \quad \Leftrightarrow \quad \begin{cases} \boldsymbol{W}(x) < 0 \\ \boldsymbol{Z}(x) - \boldsymbol{Y}(x)\boldsymbol{W}^{-1}(x)\boldsymbol{Y}^T(x) < 0 \end{cases}$$

where $\boldsymbol{Z}(x) = \boldsymbol{Z}^T(x)$, $\boldsymbol{W}(x) = \boldsymbol{W}^T(x)$, *and* $\boldsymbol{Y}(x)$ *depend affinely on* x.

Lemma 2. *[126]*

For a given matrix $\boldsymbol{T} \in \mathbb{R}^{p\times n}$, *rank(*$\boldsymbol{T}$*)* $= p$, *for any matrix, the necessary and sufficient condition to the existence of* $\boldsymbol{T}\boldsymbol{X} = \bar{\boldsymbol{X}}\boldsymbol{T}$ *is that* $\boldsymbol{X}$ *can be decomposed into:*

$$\boldsymbol{X} = \boldsymbol{W} \begin{bmatrix} \bar{X}_{11} & 0 \\ 0 & \bar{X}_{22} \end{bmatrix} \boldsymbol{W}^T \tag{3.26}$$

where $\boldsymbol{W} \in \mathbb{R}^{n\times n}$ *is a unitary matrix,* $\bar{X}_{11} \in \mathbb{R}^{p\times p}, \bar{X}_{22} \in \mathbb{R}^{(n-p)\times(n-p)}$

3.4.2 Main Results

The stability of the close-loop system (Eq. (3.24)) can be given by the following theorem:

Theorem 1.

If there exist positive definite and symmetric matrices $\boldsymbol{Y}_{1j}$, $\boldsymbol{Y}_{2j}$, $\boldsymbol{M}_{1j}$, $\boldsymbol{M}_{2j}$ *(j = 1,2,3),* $\boldsymbol{X}_1$,

$\boldsymbol{X}_2$, $\boldsymbol{X}_{11}$, $\boldsymbol{X}_{22}$, $\boldsymbol{X}_3$ and appropriate matrices $\boldsymbol{W}_1$, $\boldsymbol{W}_2$ such that the linear matrix inequality in Eq. (3.27) holds,

$$\begin{bmatrix}
\boldsymbol{\Omega}_{11} & \boldsymbol{\Omega}_{12} & \boldsymbol{\Omega}_{13} & \boldsymbol{\Omega}_{14} & \boldsymbol{\Omega}_{15} & \boldsymbol{\Omega}_{16} & \boldsymbol{\Omega}_{17} & \boldsymbol{\Omega}_{18} & \boldsymbol{\Omega}_{19} \\
\star & -\boldsymbol{\Omega}_{22} & \mathbf{0} & \mathbf{0} & \mathbf{0} & \boldsymbol{\Omega}_{26} & \boldsymbol{\Omega}_{27} & \mathbf{0} & \mathbf{0} \\
\star & \star & -\boldsymbol{\Omega}_{33} & \mathbf{0} & \mathbf{0} & \boldsymbol{\Omega}_{36} & \boldsymbol{\Omega}_{37} & \mathbf{0} & \mathbf{0} \\
\star & \star & \star & -\boldsymbol{\Omega}_{44} & \mathbf{0} & \boldsymbol{\Omega}_{46} & \boldsymbol{\Omega}_{47} & \mathbf{0} & \mathbf{0} \\
\star & \star & \star & \star & -\boldsymbol{\Omega}_{55} & \boldsymbol{\Omega}_{56} & \boldsymbol{\Omega}_{57} & \mathbf{0} & \mathbf{0} \\
\star & \star & \star & \star & \star & -\boldsymbol{\Omega}_{66} & \mathbf{0} & \mathbf{0} & \mathbf{0} \\
\star & \star & \star & \star & \star & \star & -\boldsymbol{\Omega}_{77} & \mathbf{0} & \mathbf{0} \\
\star & \star & \star & \star & \star & \star & \star & -\boldsymbol{\Omega}_{88} & \mathbf{0} \\
\star & \star & \star & \star & \star & \star & \star & \star & -\boldsymbol{\Omega}_{99}
\end{bmatrix} < 0$$

where the elements of the linear matrix are:

$$\boldsymbol{\Omega}_{11} = \begin{bmatrix}
\boldsymbol{\Phi}_{11} & \boldsymbol{W}_2\boldsymbol{C} & \mathbf{0} \\
\star & \boldsymbol{\Phi}_{22} & \boldsymbol{\Phi}_{23} \\
\star & \star & \boldsymbol{\Phi}_{33}
\end{bmatrix},$$

where

$$\boldsymbol{\Phi}_{11} = \boldsymbol{A}_0\boldsymbol{X}_1 + \boldsymbol{X}_1\boldsymbol{A}_0^T + \boldsymbol{B}\boldsymbol{W}_1 + \boldsymbol{W}_1^T\boldsymbol{B}^T,$$

$$\boldsymbol{\Phi}_{23} = -\boldsymbol{B}\boldsymbol{C}_F\boldsymbol{X}_3 + \boldsymbol{C}^T\boldsymbol{W}_2^T\boldsymbol{B}^{+T}\boldsymbol{B}_F^T,$$

$$\boldsymbol{\Phi}_{22} = \boldsymbol{A}_0\boldsymbol{X}_2 + \boldsymbol{X}_2\boldsymbol{A}_0^T - \boldsymbol{W}_2\boldsymbol{C} + \boldsymbol{C}^T\boldsymbol{W}_2^T,$$

$$\boldsymbol{\Phi}_{33} = (\boldsymbol{A}_F + \boldsymbol{B}_F\boldsymbol{C}_F)\boldsymbol{X}_3 + \boldsymbol{X}_3(\boldsymbol{A}_F + \boldsymbol{B}_F\boldsymbol{C}_F)^T.$$

$$\boldsymbol{\Omega}_{12} = \begin{bmatrix} \boldsymbol{A}_1\boldsymbol{Y}_{11} & \boldsymbol{0} & \boldsymbol{0} \\ \star & \boldsymbol{A}_1\boldsymbol{Y}_{12} & \boldsymbol{0} \\ \star & \star & \boldsymbol{0} \end{bmatrix}, \quad \boldsymbol{\Omega}_{13} = \begin{bmatrix} \boldsymbol{A}_2\boldsymbol{Y}_{21} & \boldsymbol{0} & \boldsymbol{0} \\ \star & \boldsymbol{A}_2\boldsymbol{Y}_{22} & \boldsymbol{0} \\ \star & \star & \boldsymbol{0} \end{bmatrix},$$

$$\boldsymbol{\Omega}_{14} = \begin{bmatrix} \boldsymbol{G}_1\boldsymbol{M}_{11} & \boldsymbol{0} & \boldsymbol{0} \\ \star & \boldsymbol{G}_1\boldsymbol{M}_{12} & \boldsymbol{0} \\ \star & \star & \boldsymbol{0} \end{bmatrix}, \boldsymbol{\Omega}_{15} = \begin{bmatrix} \boldsymbol{G}_2\boldsymbol{M}_{21} & \boldsymbol{0} & \boldsymbol{0} \\ \star & \boldsymbol{G}_2\boldsymbol{M}_{22} & \boldsymbol{0} \\ \star & \star & \boldsymbol{0} \end{bmatrix},$$

$$\boldsymbol{\Omega}_{16} = \begin{bmatrix} \boldsymbol{X}_1\boldsymbol{A}_0^T + \boldsymbol{W}_1^T\boldsymbol{B}^T & \boldsymbol{0} & \boldsymbol{0} \\ \boldsymbol{C}^T\boldsymbol{W}_2^T & \boldsymbol{X}_2\boldsymbol{A}_0^T - \boldsymbol{C}^T\boldsymbol{W}_2^T & \boldsymbol{C}^T\boldsymbol{W}_2^T\boldsymbol{B}^{+T}\boldsymbol{B}_F^T \\ \boldsymbol{0} & \boldsymbol{X}_3\boldsymbol{C}_F^T\boldsymbol{B}^T & \boldsymbol{X}_3(\boldsymbol{A}_F + \boldsymbol{C}_F\boldsymbol{B}_F)^T \end{bmatrix}$$

$$\boldsymbol{\Omega}_{18} = \begin{bmatrix} \boldsymbol{X}_1 & \boldsymbol{0} & \boldsymbol{0} \\ \star & \boldsymbol{X}_2 & \boldsymbol{0} \\ \star & \star & \boldsymbol{X}_3 \end{bmatrix}, \quad \boldsymbol{\Omega}_{22} = \begin{bmatrix} \boldsymbol{Y}_{11} & \boldsymbol{0} & \boldsymbol{0} \\ \star & \boldsymbol{Y}_{12} & \boldsymbol{0} \\ \star & \star & \boldsymbol{Y}_{13} \end{bmatrix},$$

$$\boldsymbol{\Omega}_{33} = \begin{bmatrix} \boldsymbol{Y}_{21} & \boldsymbol{0} & \boldsymbol{0} \\ \star & \boldsymbol{Y}_{22} & \boldsymbol{0} \\ \star & \star & \boldsymbol{Y}_{23} \end{bmatrix}, \quad \boldsymbol{\Omega}_{44} = \begin{bmatrix} \boldsymbol{M}_{11} & \boldsymbol{0} & \boldsymbol{0} \\ \star & \boldsymbol{M}_{12} & \boldsymbol{0} \\ \star & \star & \boldsymbol{M}_{13} \end{bmatrix},$$

$$\boldsymbol{\Omega}_{55} = \begin{bmatrix} \boldsymbol{M}_{21} & \boldsymbol{0} & \boldsymbol{0} \\ \star & \boldsymbol{M}_{22} & \boldsymbol{0} \\ \star & \star & \boldsymbol{M}_{23} \end{bmatrix}, \quad \boldsymbol{\Omega}_{26} = \begin{bmatrix} \boldsymbol{Y}_{11}\boldsymbol{A}_1^T & \boldsymbol{0} & \boldsymbol{0} \\ \star & \boldsymbol{Y}_{12}\boldsymbol{A}_1^T & \boldsymbol{0} \\ \star & \star & \boldsymbol{0} \end{bmatrix},$$

$$\boldsymbol{\Omega}_{36} = \begin{bmatrix} \boldsymbol{Y}_{21}\boldsymbol{A}_2^T & \boldsymbol{0} & \boldsymbol{0} \\ \star & \boldsymbol{Y}_{22}\boldsymbol{A}_2^T & \boldsymbol{0} \\ \star & \star & \boldsymbol{0} \end{bmatrix}, \ \boldsymbol{\Omega}_{46} = \begin{bmatrix} \boldsymbol{M}_{11}\boldsymbol{G}_1^T & \boldsymbol{0} & \boldsymbol{0} \\ \star & \boldsymbol{M}_{12}\boldsymbol{G}_1^T & \boldsymbol{0} \\ \star & \star & \boldsymbol{0} \end{bmatrix},$$

$$\boldsymbol{\Omega}_{56} = \begin{bmatrix} \boldsymbol{M}_{21}\boldsymbol{G}_2^T & \boldsymbol{0} & \boldsymbol{0} \\ \star & \boldsymbol{M}_{22}\boldsymbol{G}_2^T & \boldsymbol{0} \\ \star & \star & \boldsymbol{0} \end{bmatrix},$$

$$\boldsymbol{\Omega}_{16} = \boldsymbol{\Omega}_{17}, \boldsymbol{\Omega}_{18} = \boldsymbol{\Omega}_{19}, \boldsymbol{\Omega}_{22} = \boldsymbol{\Omega}_{88}, \boldsymbol{\Omega}_{33} = \boldsymbol{\Omega}_{99}, \boldsymbol{\Omega}_{44} = \boldsymbol{\Omega}_{66},$$

$$\boldsymbol{\Omega}_{55} = \boldsymbol{\Omega}_{77}, \boldsymbol{\Omega}_{26} = \boldsymbol{\Omega}_{27}, \boldsymbol{\Omega}_{36} = \boldsymbol{\Omega}_{37}, \boldsymbol{\Omega}_{46} = \boldsymbol{\Omega}_{47}, \boldsymbol{\Omega}_{56} = \boldsymbol{\Omega}_{57}.$$

Then the neutral-type time-delay system in Eq. (3.24) is asymptotically stable with the controller proposed in Eq. (3.23). The singular values of $\boldsymbol{X}_2$ and $\boldsymbol{C}$ can be decomposed into:

$$\boldsymbol{X}_2 = \boldsymbol{V}\, diag(\boldsymbol{X}_{11}, \boldsymbol{X}_{22})\boldsymbol{V}^T, \ \ \boldsymbol{C} = \boldsymbol{U}[\boldsymbol{S}, \boldsymbol{0}]\boldsymbol{V}^T.$$

The state feedback control gain $\boldsymbol{K}_p$ and observer gain $\boldsymbol{L}$ are chosen as:

$$\boldsymbol{K}_p = \boldsymbol{W}_1\boldsymbol{X}_1^{-1}, \ \ \boldsymbol{L} = \boldsymbol{W}_2\boldsymbol{U}\boldsymbol{S}\boldsymbol{X}_{11}^{-1}\boldsymbol{S}^{-1}\boldsymbol{U}^T.$$

***Proof* 1.** *Consider the Lyapunov-Krasovskii functional candidate:*

$$\begin{aligned} V\big(\boldsymbol{\xi}(t)\big) = &\int_{t-h_1}^{t} \boldsymbol{\xi}^T(s)\boldsymbol{R}_1\boldsymbol{\xi}(s)ds + \int_{t-h_2}^{t} \boldsymbol{\xi}^T(s)\boldsymbol{R}_2\boldsymbol{\xi}(s)ds + \int_{t-h_1}^{t} \dot{\boldsymbol{\xi}}^T(s)\boldsymbol{N}_1\dot{\boldsymbol{\xi}}(s)ds \\ &+ \int_{t-h_2}^{t} \dot{\boldsymbol{\xi}}^T(s)\boldsymbol{N}_2\dot{\boldsymbol{\xi}}(s)ds + \boldsymbol{\xi}(t)^T\boldsymbol{P}\boldsymbol{\xi}(t), \end{aligned} \tag{3.27}$$

where

$$\begin{aligned} \boldsymbol{P} &= diag(\boldsymbol{P}_1, \boldsymbol{P}_2, \boldsymbol{P}_3), \\ \boldsymbol{R}_1 &= diag(\boldsymbol{R}_{11}, \boldsymbol{R}_{12}, \boldsymbol{R}_{13}), \quad \boldsymbol{R}_2 = diag(\boldsymbol{R}_{21}, \boldsymbol{R}_{22}, \boldsymbol{R}_{23}), \end{aligned}$$

$$\boldsymbol{N}_1 = diag(\boldsymbol{N}_{11}, \boldsymbol{N}_{12}, \boldsymbol{N}_{13}), \;\; \boldsymbol{N}_2 = diag(\boldsymbol{N}_{21}, \boldsymbol{N}_{22}, \boldsymbol{N}_{23}).$$

Take the derivative of the Lyapunov-Krasovskii functional candidate:

$$\begin{aligned}\dot{V}\Big(\boldsymbol{\xi}(t)\Big) = \boldsymbol{\xi}^T(t)(\boldsymbol{R}_1 + \boldsymbol{R}_2)\boldsymbol{\xi}(t) + \dot{\boldsymbol{\xi}}^T(t)(\boldsymbol{N}_1 + \boldsymbol{N}_2)\dot{\boldsymbol{\xi}}(t) + 2\boldsymbol{\xi}(t)^T\boldsymbol{P}\dot{\boldsymbol{\xi}}(t) \\ -\boldsymbol{\xi}^T(t-h_1)\boldsymbol{R}_1\boldsymbol{\xi}(t-h_1)\boldsymbol{\xi}^T(t-h_2)\boldsymbol{R}_2\boldsymbol{\xi}(t-h_2) \qquad (3.28)\end{aligned}$$

Given $\dot{\boldsymbol{\xi}}(t)$ in Eq. (3.25), substitute $\dot{\boldsymbol{\xi}}(t)$ into Eq. (3.28):

$$\begin{aligned}\dot{V}\Big(\boldsymbol{\xi}(t)\Big) &= \boldsymbol{\xi}^T(t)(\boldsymbol{R}_1 + \boldsymbol{R}_2)\boldsymbol{\xi}(t) - \boldsymbol{\xi}^T(t-h_1)\boldsymbol{R}_1\boldsymbol{\xi}(t-h_1) - \boldsymbol{\xi}^T(t-h_2)\boldsymbol{R}_2\boldsymbol{\xi}(t-h_2) \\ &+2\boldsymbol{\xi}(t)^T\boldsymbol{P}\Big[\bar{\boldsymbol{A}}_0\boldsymbol{\xi}(t) + \bar{\boldsymbol{A}}_1\boldsymbol{\xi}(t-h_1) + \bar{\boldsymbol{A}}_2\boldsymbol{\xi}(t-h_2) + \bar{\boldsymbol{G}}_1\dot{\boldsymbol{\xi}}(t-h_1) + \bar{\boldsymbol{G}}_2\dot{\boldsymbol{\xi}}(t-h_2)\Big] \\ &+\Big[\bar{\boldsymbol{A}}_0\boldsymbol{\xi}(t) + \bar{\boldsymbol{A}}_1\boldsymbol{\xi}(t-h_1) + \bar{\boldsymbol{A}}_2\boldsymbol{\xi}(t-h_2) + \bar{\boldsymbol{G}}_1\dot{\boldsymbol{\xi}}(t-h_1) + \bar{\boldsymbol{G}}_2\dot{\boldsymbol{\xi}}(t-h_2)\Big](\boldsymbol{N}_1 + \boldsymbol{N}_2) \\ &\times\Big[\bar{\boldsymbol{A}}_0\boldsymbol{\xi}(t) + \bar{\boldsymbol{A}}_1\boldsymbol{\xi}(t-h_1) + \bar{\boldsymbol{A}}_2\boldsymbol{\xi}(t-h_2) \\ &+\bar{\boldsymbol{G}}_1\dot{\boldsymbol{\xi}}(t-h_1) + \bar{\boldsymbol{G}}_2\dot{\boldsymbol{\xi}}(t-h_2)\Big] \qquad (3.29)\end{aligned}$$

Define:

$$\boldsymbol{\chi}(t) = \Big[\boldsymbol{\xi}(t) \quad \boldsymbol{\xi}(t-h_1) \quad \boldsymbol{\xi}(t-h_2) \quad \dot{\boldsymbol{\xi}}(t-h_1) \quad \dot{\boldsymbol{\xi}}(t-h_2)\Big]^T$$

Then Eq. (3.29) can be written in a matrix form as:

$$\begin{aligned}&\dot{V}\Big(\boldsymbol{\xi}(t)\Big) \\ &= \boldsymbol{\chi}^T\begin{bmatrix}(\boldsymbol{P}\bar{\boldsymbol{A}}_0 + \bar{\boldsymbol{A}}_0^T\boldsymbol{P} + \boldsymbol{R}_1 + \boldsymbol{R}_2) & \boldsymbol{P}\bar{\boldsymbol{A}}_1 & \boldsymbol{P}\bar{\boldsymbol{A}}_2 & \boldsymbol{P}\bar{\boldsymbol{G}}_1 & \boldsymbol{P}\bar{\boldsymbol{G}}_2 \\ \star & -\boldsymbol{R}_1 & \boldsymbol{0} & \boldsymbol{0} & \boldsymbol{0} \\ \star & \star & -\boldsymbol{R}_2 & \boldsymbol{0} & \boldsymbol{0} \\ \star & \star & \star & -\boldsymbol{N}_1 & \boldsymbol{0} \\ \star & \star & \star & \star & -\boldsymbol{N}_2\end{bmatrix}\boldsymbol{\chi}\end{aligned}$$

$$
\begin{aligned}
&+\boldsymbol{\chi}^T \begin{bmatrix} \bar{\boldsymbol{A}}_0^T \\ \bar{\boldsymbol{A}}_1^T \\ \bar{\boldsymbol{A}}_2^T \\ \bar{\boldsymbol{G}}_1^T \\ \bar{\boldsymbol{G}}_2^T \end{bmatrix} (\boldsymbol{N}_1 + \boldsymbol{N}_2) \begin{bmatrix} \bar{\boldsymbol{A}}_0^T \\ \bar{\boldsymbol{A}}_1^T \\ \bar{\boldsymbol{A}}_2^T \\ \bar{\boldsymbol{G}}_1^T \\ \bar{\boldsymbol{G}}_2^T \end{bmatrix}^T \boldsymbol{\chi} \\
&= \boldsymbol{\chi}^T \cdot \boldsymbol{\Lambda} \cdot \boldsymbol{\chi}
\end{aligned} \tag{3.30}
$$

where

$$
\boldsymbol{\Lambda} = \begin{bmatrix} \boldsymbol{A}^\star & \boldsymbol{P}\bar{\boldsymbol{A}}_1 & \boldsymbol{P}\bar{\boldsymbol{A}}_2 & \boldsymbol{P}\bar{\boldsymbol{G}}_1 & \boldsymbol{P}\bar{\boldsymbol{G}}_2 \\ \star & -\boldsymbol{R}_1 & \boldsymbol{0} & \boldsymbol{0} & \boldsymbol{0} \\ \star & \star & -\boldsymbol{R}_2 & \boldsymbol{0} & \boldsymbol{0} \\ \star & \star & \star & -\boldsymbol{N}_1 & \boldsymbol{0} \\ \star & \star & \star & \star & -\boldsymbol{N}_2 \end{bmatrix} + \begin{bmatrix} \bar{\boldsymbol{A}}_0^T \\ \bar{\boldsymbol{A}}_1^T \\ \bar{\boldsymbol{A}}_2^T \\ \bar{\boldsymbol{G}}_1^T \\ \bar{\boldsymbol{G}}_2^T \end{bmatrix} (\boldsymbol{N}_1 + \boldsymbol{N}_2) \begin{bmatrix} \bar{\boldsymbol{A}}_0^T \\ \bar{\boldsymbol{A}}_1^T \\ \bar{\boldsymbol{A}}_2^T \\ \bar{\boldsymbol{G}}_1^T \\ \bar{\boldsymbol{G}}_2^T \end{bmatrix}^T
$$

where $\boldsymbol{A}^\star = \boldsymbol{P}\bar{\boldsymbol{A}}_0 + \bar{\boldsymbol{A}}_0^T\boldsymbol{P} + \boldsymbol{R}_1 + \boldsymbol{R}_2$.

If $\boldsymbol{\Lambda}$ *is negative definite, then for a sufficiently small positive scalar* λ*, there exists* $\dot{V}\big(\boldsymbol{\xi}(t)\big) \leq -\lambda\|\boldsymbol{x}(t)\|$*, which ensures that the system (Eq. (3.18)) is asymptotically stable.*

By applying Lemma. 1, the matrix inequality becomes:

$$\begin{bmatrix} \boldsymbol{A}^{\star} & \boldsymbol{P}\bar{\boldsymbol{A}}_1 & \boldsymbol{P}\bar{\boldsymbol{A}}_2 & \boldsymbol{P}\bar{\boldsymbol{G}}_1 & \boldsymbol{P}\bar{\boldsymbol{G}}_2 & \bar{\boldsymbol{A}}_0^T & \bar{\boldsymbol{A}}_0^T \\ \star & -\boldsymbol{R}_1 & \mathbf{0} & \mathbf{0} & \mathbf{0} & \bar{\boldsymbol{A}}_1^T & \bar{\boldsymbol{A}}_1^T \\ \star & \star & -\boldsymbol{R}_2 & \mathbf{0} & \mathbf{0} & \bar{\boldsymbol{A}}_2^T & \bar{\boldsymbol{A}}_2^T \\ \star & \star & \star & -\boldsymbol{N}_1 & \mathbf{0} & \bar{\boldsymbol{G}}_1^T & \bar{\boldsymbol{G}}_1^T \\ \star & \star & \star & \star & -\boldsymbol{N}_2 & \bar{\boldsymbol{G}}_2^T & \bar{\boldsymbol{G}}_2^T \\ \star & \star & \star & \star & \star & -\boldsymbol{N}_1^{-1} & \mathbf{0} \\ \star & \star & \star & \star & \star & \star & -\boldsymbol{N}_2^{-1} \end{bmatrix} < 0$$

Applying Lemma. 1 again, the above matrix inequality is converted into:

$$\begin{bmatrix} \bar{\boldsymbol{A}}^{\star} & \boldsymbol{P}\bar{\boldsymbol{A}}_1 & \boldsymbol{P}\bar{\boldsymbol{A}}_2 & \boldsymbol{P}\bar{\boldsymbol{G}}_1 & \boldsymbol{P}\bar{\boldsymbol{G}}_2 & \bar{\boldsymbol{A}}_0^T & \bar{\boldsymbol{A}}_0^T & \boldsymbol{I} & \boldsymbol{I} \\ \star & -\boldsymbol{R}_1 & \mathbf{0} & \mathbf{0} & \mathbf{0} & \bar{\boldsymbol{A}}_1^T & \bar{\boldsymbol{A}}_1^T & \mathbf{0} & \mathbf{0} \\ \star & \star & -\boldsymbol{R}_2 & \mathbf{0} & \mathbf{0} & \bar{\boldsymbol{A}}_2^T & \bar{\boldsymbol{A}}_2^T & \mathbf{0} & \mathbf{0} \\ \star & \star & \star & -\boldsymbol{N}_1 & \mathbf{0} & \bar{\boldsymbol{G}}_1^T & \bar{\boldsymbol{G}}_1^T & \mathbf{0} & \mathbf{0} \\ \star & \star & \star & \star & -\boldsymbol{N}_2 & \bar{\boldsymbol{G}}_2^T & \bar{\boldsymbol{G}}_2^T & \mathbf{0} & \mathbf{0} \\ \star & \star & \star & \star & \star & -\boldsymbol{N}_1^{-1} & \mathbf{0} & \mathbf{0} & \mathbf{0} \\ \star & \star & \star & \star & \star & \star & -\boldsymbol{N}_2^{-1} & \mathbf{0} & \mathbf{0} \\ \star & \star & \star & \star & \star & \star & \star & -\boldsymbol{R}_1^{-1} & \mathbf{0} \\ \star & \star & \star & \star & \star & \star & \star & \star & -\boldsymbol{R}_2^{-1} \end{bmatrix} < 0$$

where $\bar{\boldsymbol{A}}^{\star} = \boldsymbol{P}\bar{\boldsymbol{A}}_0 + \bar{\boldsymbol{A}}_0^T\boldsymbol{P}$.

Assume:

$$\boldsymbol{X}_i = \boldsymbol{P}_i^{-1},\ \boldsymbol{Y}_{1i} = \boldsymbol{R}_{1i}^{-1},\ \boldsymbol{Y}_{2i} = \boldsymbol{R}_{2i}^{-1},\ \boldsymbol{M}_{1i} = \boldsymbol{N}_{1i}^{-1},\ \boldsymbol{M}_{2i} = \boldsymbol{N}_{2i}^{-1}.$$

Then

$$\begin{aligned}
&\boldsymbol{X} = diag\Big(\boldsymbol{X}_1, \boldsymbol{X}_2, \boldsymbol{X}_3\Big),\\
&\boldsymbol{Y}_1 = diag\Big(\boldsymbol{Y}_{11}, \boldsymbol{Y}_{12}, \boldsymbol{Y}_{13}\Big),\ \boldsymbol{Y}_2 = diag\Big(\boldsymbol{Y}_{21}, \boldsymbol{Y}_{22}, \boldsymbol{Y}_{23}\Big),\\
&\boldsymbol{M}_1 = diag\Big(\boldsymbol{M}_{11}, \boldsymbol{M}_{12}, \boldsymbol{M}_{13}\Big), \boldsymbol{M}_2 = diag\Big(\boldsymbol{M}_{21}, \boldsymbol{M}_{22}, \boldsymbol{M}_{23}\Big).
\end{aligned}$$

Now we left multiply and right multiply the above matrix by:

$$diag\Big(\boldsymbol{X},\ \boldsymbol{Y}_1, \boldsymbol{Y}_2, \boldsymbol{M}_1, \boldsymbol{M}_2,\ \boldsymbol{I},\ \boldsymbol{I},\ \boldsymbol{I},\ \boldsymbol{I}\Big) \tag{3.31}$$

We can obtain:

$$\begin{bmatrix}
\check{\boldsymbol{A}}^{\star} & \bar{\boldsymbol{A}}_1\boldsymbol{Y}_1 & \bar{\boldsymbol{A}}_2\boldsymbol{Y}_2 & \bar{\boldsymbol{G}}_1\boldsymbol{M}_1 & \boldsymbol{G}_2\boldsymbol{M}_2 & \boldsymbol{X}\bar{\boldsymbol{A}}_0^T & \boldsymbol{X}\bar{\boldsymbol{A}}_0^T & \boldsymbol{X} & \boldsymbol{X}\\
\star & -\boldsymbol{Y}_1 & \boldsymbol{0} & \boldsymbol{0} & \boldsymbol{0} & \boldsymbol{Y}_1\bar{\boldsymbol{A}}_1^T & \boldsymbol{Y}_1\bar{\boldsymbol{A}}_1^T & \boldsymbol{0} & \boldsymbol{0}\\
\star & \star & -\boldsymbol{Y}_2 & \boldsymbol{0} & \boldsymbol{0} & \boldsymbol{Y}_2\bar{\boldsymbol{A}}_2^T & \boldsymbol{Y}_2\bar{\boldsymbol{A}}_2^T & \boldsymbol{0} & \boldsymbol{0}\\
\star & \star & \star & -\boldsymbol{M}_1 & \boldsymbol{0} & \boldsymbol{M}_1\bar{\boldsymbol{G}}_1^T & \boldsymbol{M}_1\bar{\boldsymbol{G}}_1^T & \boldsymbol{0} & \boldsymbol{0}\\
\star & \star & \star & \star & -\boldsymbol{M}_2 & \boldsymbol{M}_2\bar{\boldsymbol{G}}_2^T & \boldsymbol{M}_2\bar{\boldsymbol{G}}_2^T & \boldsymbol{0} & \boldsymbol{0}\\
\star & \star & \star & \star & \star & -\boldsymbol{M}_1 & \boldsymbol{0} & \boldsymbol{0} & \boldsymbol{0}\\
\star & \star & \star & \star & \star & \star & -\boldsymbol{M}_2 & \boldsymbol{0} & \boldsymbol{0}\\
\star & \star & \star & \star & \star & \star & \star & -\boldsymbol{Y}_1 & \boldsymbol{0}\\
\star & \star & \star & \star & \star & \star & \star & \star & -\boldsymbol{Y}_2
\end{bmatrix} < 0$$

where $\check{\boldsymbol{A}}^{\star} = \bar{\boldsymbol{A}}_0\boldsymbol{X} + \boldsymbol{X}\bar{\boldsymbol{A}}_0^T$.

If we expand the above matrix, there will be multiple occurrences of $\boldsymbol{LCX}_2$ *and the above matrix is not an LMI. To convert the matrix above to an LMI, we apply Lemma. 2 by some matrix manipulations:*

$$\bar{\boldsymbol{X}}_2 = \boldsymbol{USX}_{11}\boldsymbol{S}^{-1}\boldsymbol{U}^T,\ \boldsymbol{CX}_2 = \bar{\boldsymbol{X}}_2\boldsymbol{C}.$$

We let

$$\boldsymbol{W}_1 = \boldsymbol{K}_p\boldsymbol{X}_1,\ \boldsymbol{W}_2 = \boldsymbol{L}\bar{\boldsymbol{X}}_2.$$

This completes the proof for Theorem 1.

Remark 1. *By using Lemma. 2, a set of new relations* $\bar{\boldsymbol{X}}_2 = \boldsymbol{USX}_{11}\boldsymbol{S}^{-1}\boldsymbol{U}^T$, $\boldsymbol{CX}_2 = \bar{\boldsymbol{X}}_2\boldsymbol{C}$, $\boldsymbol{W}_1 = \boldsymbol{K}_p\boldsymbol{X}_1,\ \boldsymbol{W}_2 = \boldsymbol{L}\bar{\boldsymbol{X}}_2$ *convert the above nonlinear matrix inequalities into linear matrix inequalities.*

Remark 2. *The LMI above can be used for stability analysis and control synthesis. There are multiple commercial software to solve the LMI. In this chapter, we use MATLAB LMI Toolbox to obtain feasible solutions.*

3.5 EID Based Control Simulation Results

In this section, a series of simulations are conducted to validate the proposed EID based control scheme. The simulation parameters are listed in Table 3.1. First, we employ the EID based controller to regulate the axial and torsional bit motions. After that, we add disturbance to the drill bit model to validate the robust performance of the proposed control scheme. Finally, we change the constant reference input to desired trajectories for a trajectory tracking problem.

In the simulations, the reference input is chosen as:

$$\boldsymbol{r}'(t) = \begin{bmatrix} 10\ \text{mm/s} \\ \\ 20\ \text{rad/s} \end{bmatrix}$$

Table 3.1 Simulation parameters in EID based control design

Parameter	Value	Description
α_A	6×10^5 Ns/m	Translation coefficient
α_T	8×10^2 Ns/rad	Angular coefficient
E	2.11×10^{11} N/m^2	Young's modulus
G	7.93×10^{10} Ns/m	Shear modulus
L	1000 m	Total length
D_o	0.12 m	Outer diameter
D_i	0.06 m	Inner diameter
A	8.5×10^{-3} m^2	Cross-sectional area
J	1.9×10^{-5} kg·m^2	Moment of inertia
ρ	7850 kg/m^3	Density
M_S	6.7×10^4 kg	Drill sting total mass
M_B	3×10^4 kg	Drill bit mass
I_B	67.5 kg·m^2	Drill bit moment of inertia
ζ	0.8	Cutter face inclination
ϵ	45 MPa	Intrinsic specific energy
σ	45 MPa	Contact strength
δ	1.0	Bit geometry parameter
R_b	0.15 m	Bit radius
n	5	Number of blades
l_w	1.2×10^{-3} m	Total wear-flat length

Then $\boldsymbol{A}_R = \mathbf{0}$. The reference matrix $\boldsymbol{B}_R$ is selected as:

$$\boldsymbol{B}_R = \begin{bmatrix} 1 & 0 \\ 0 & 0.05 \end{bmatrix} \tag{3.32}$$

The low-pass filter $\boldsymbol{F}(s)$ is chosen as:

$$\boldsymbol{F}(s) = \begin{bmatrix} \dfrac{200}{s+200} & 0 \\ 0 & \dfrac{100}{s+100} \end{bmatrix}$$

From $\boldsymbol{F}(s)$, $\boldsymbol{A}_F$, $\boldsymbol{B}_F$, and $\boldsymbol{C}_F$ can be obtained as:

$$\boldsymbol{A}_F = \begin{bmatrix} -201 & 0 \\ 0 & -101 \end{bmatrix}, \quad \boldsymbol{B}_F = \begin{bmatrix} 200 & 0 \\ 0 & 100 \end{bmatrix}, \quad \boldsymbol{C}_F = \begin{bmatrix} 1 & 0 \\ 0 & 1 \end{bmatrix}.$$

Then the output matrix $\boldsymbol{C} = \text{diag}(1, 1)$, and $\boldsymbol{C}$ is decomposed to get $\boldsymbol{U} = \text{diag}(1, 1)$, $\boldsymbol{V} = \text{diag}(1, 1)$. Therefore, $\bar{\boldsymbol{X}}_2 = \boldsymbol{X}_{11}$.

The control input gain $\boldsymbol{K}_p$ and observer gain $\boldsymbol{L}$ are obtained as:

$$\boldsymbol{K}_p = \begin{bmatrix} 0.4735 & 0 \\ 0 & 0.7008 \end{bmatrix}, \quad \boldsymbol{L} = \begin{bmatrix} 199.3022 & 0 \\ 0 & 357.6114 \end{bmatrix}.$$

3.5.1 EID Based Controller Performance

The equivalent input disturbance based controller is applied in this subsection. As shown in Fig. 3.4, the bit rate of penetration can quickly reach the desired bit axial velocity at around 5 sec. At the initial 5 sec, the bit ROP exhibits large transient as large as 0.09 m/s. Then it quickly converges to the reference value after some damped oscillations. After 5 sec, the ROP converges with less than 1% error. As illustrated in Fig. 3.4, the torsional velocity is also stabilized at around $30 \sim 40$ sec.

3.5.2 EID Based Controller Performance under Uncertainties

In the down-hole drilling operations, there will always be uncertainties either in the bit rock cutting process or in the data measurements. Therefore, we will also test the EID based controller's performance under these uncertainties. We add the white-noise in the neutral-type time-delay model to model the drill bit uncertainties.

As demonstrated in Fig. 3.5, the EID controller maintains very similar velocity profiles in Fig. 3.4. The rate of penetration converges to its desired value after 5 sec, and the drill bit torsional velocity reaches its stable region under $30 \sim 40$ sec. This demonstrates that

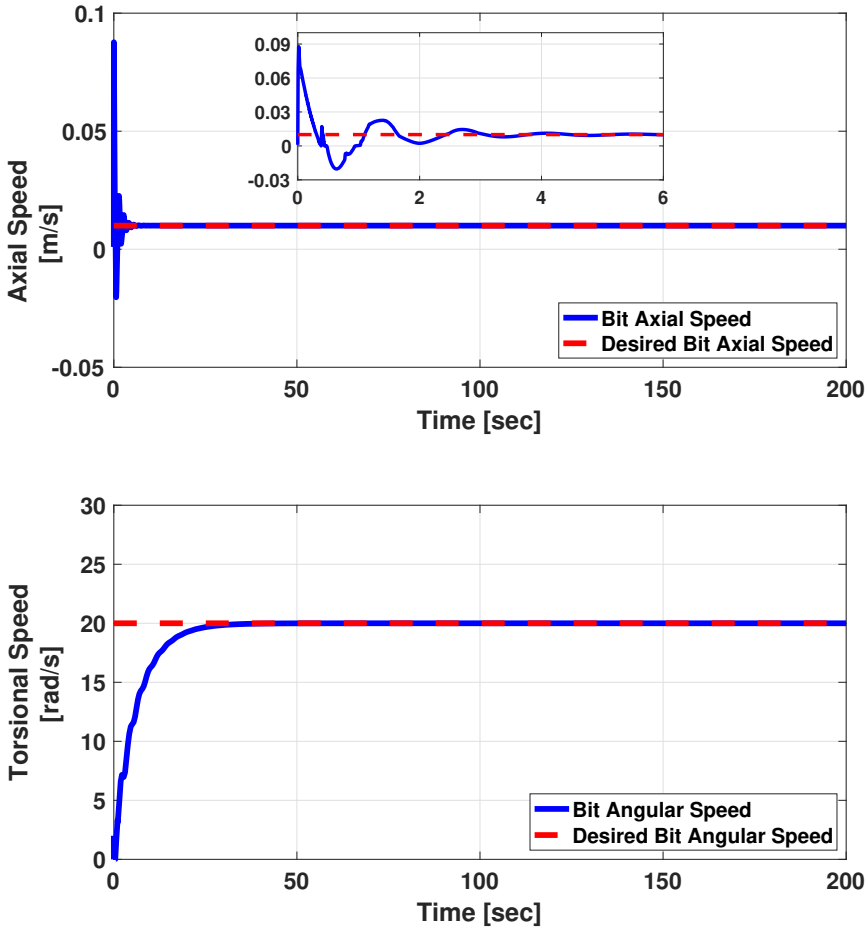

Figure 3.4 Drill bit velocity profiles (with EID based control)

the equivalent input disturbance controller can efficiently reject disturbance and maintain robustness under uncertainties.

3.5.3 Trajectory Tracking Performance of the EID Based Controller

In this subsection, we define a desired non-constant trajectory reference $\boldsymbol{r}'(t)$ as below:

$$\boldsymbol{r}'(t) = \begin{bmatrix} r_1'(t), & r_2'(t) \end{bmatrix}^T \tag{3.33}$$

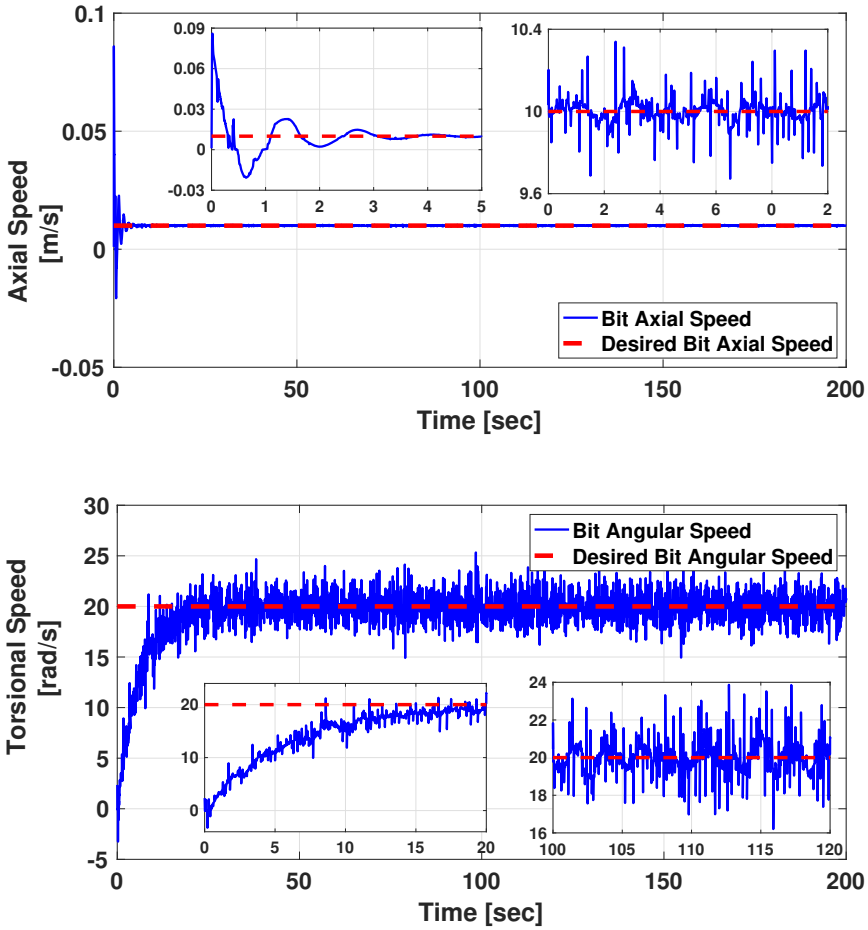

Figure 3.5 Drill bit velocity profile under uncertainties.

where the axial reference $r_1(t)$ is set to be sinusoidal; and the torsional reference $r_2(t)$ is set to be multiple ramps:

$$r_1'(t) = 3v + 0.5v\sin(\frac{\pi t}{20}) \tag{3.34}$$

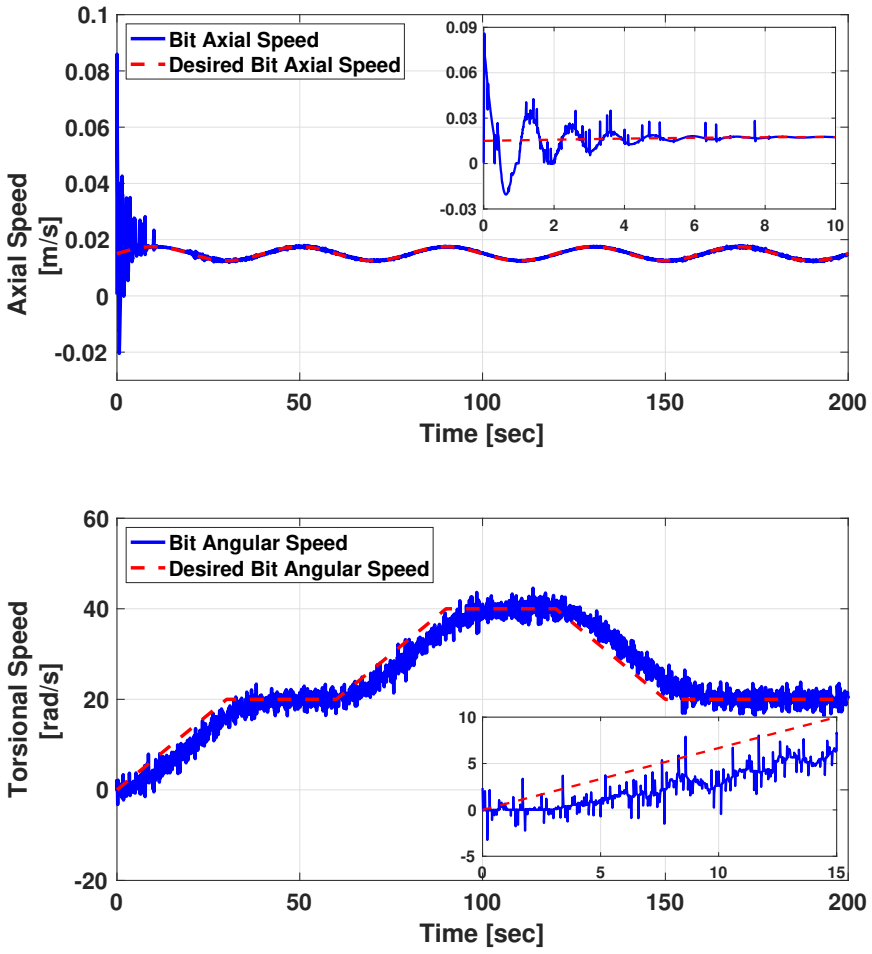

Figure 3.6 Drill bit velocity profile under uncertainties with sinusoidal axial trajectory and torsional ramp trajectories (with EID based control).

$$r_2'(t) = \begin{cases} \omega t/30 & \text{if } t \in [0, 30) \\ \omega & \text{if } t \in [30, 60) \\ \omega t/30 - \omega & \text{if } t \in [60, 90) \\ 2\omega & \text{if } t \in [90, 120) \\ -\omega t/30 + 6\omega & \text{if } t \in [120, 150) \\ \omega & \text{if } t \in [150, 200] \end{cases} \tag{3.35}$$

where $v = 5$ mm/s and $\omega = 20$ rad/s.

Figure 3.6 demonstrates the controller performance. The red dashed line stands for the desired trajectory reference and the blue line shows the drill bit speed response under the EID controller. It is evident that the actual bit speed follows the reference trajectory. Figure 3.7 shows the hook load and top drive torque associated with the drill bit velocity profile in Fig. 3.6.

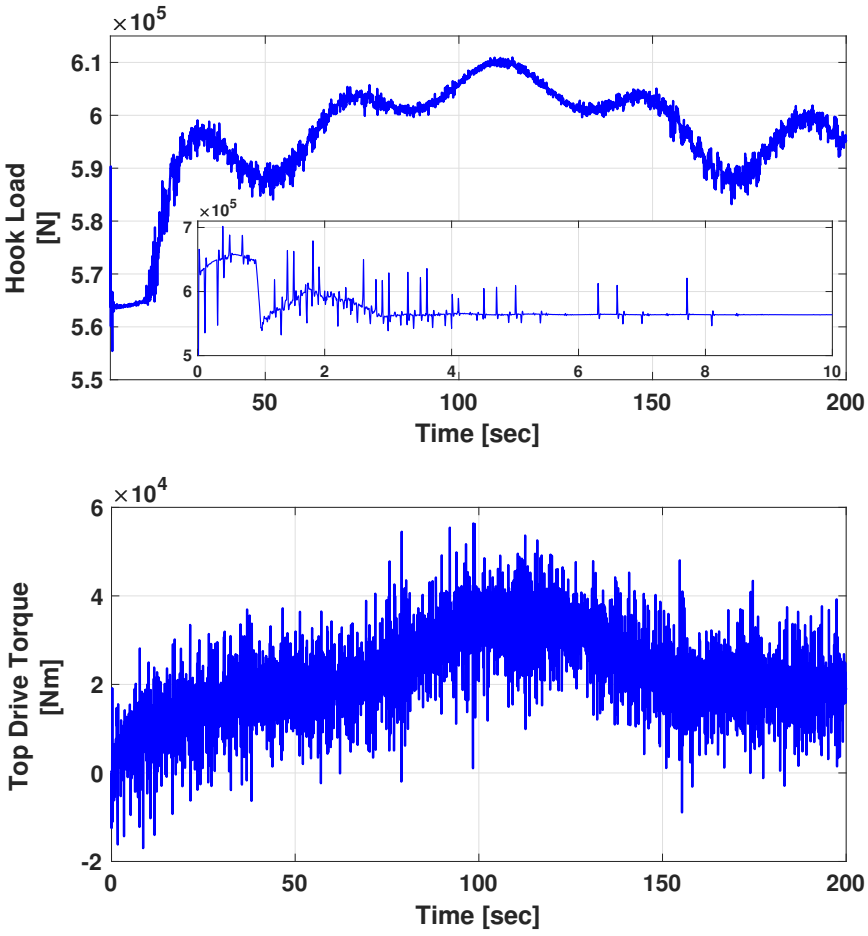

Figure 3.7 Hook load and top drive torque.

3.5.4 Sensitivity Analysis

Sensitivity analysis is also conducted by varying the parameters of the model used in the simulation while keeping the same controller.

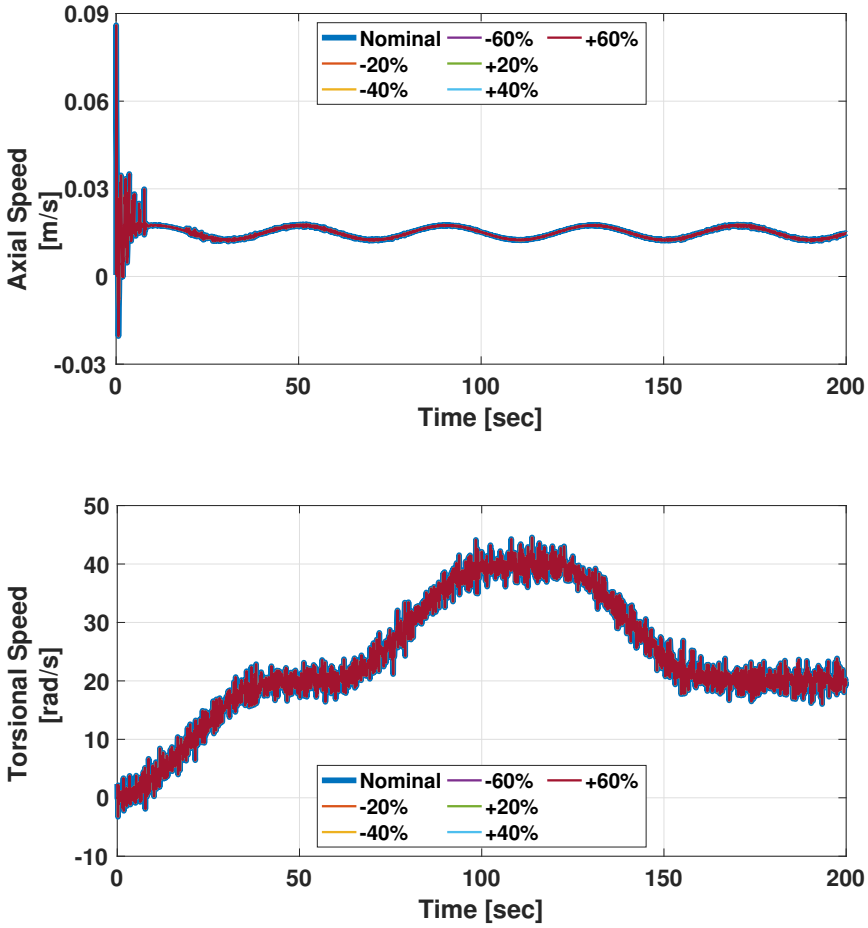

Figure 3.8 Robustness of EID controller with different ϵ.

Figure 3.8 shows the bit velocity profile with different ϵ. This shows the EID controller is insensitive to the intrinsic specific energy ϵ. A similar sensitivity analysis has also been conducted for other bit parameters σ, ζ, and a similar conclusion can be made.

3.6 Summary

This chapter proposes an equivalent input disturbance based control for the down-hole drilling process based on a neutral type dynamics model with axial-torsional coupled dynamics. As an essential part of the down-hole drilling system, the bit/rock interaction poses nonlinearity for the system dynamics. In this chapter, we treat the nonlinear bit/rock interaction dynamics as an external disturbance to the neutral-type system, and use a disturbance estimator to eliminate the complex and uncertain bit/rock interaction. We then propose a Lyapunov-Krasovskii functional for closed-loop system stability analysis and control synthesis. By solving the linear matrix inequalities derived from the Lyapunov-Krasovskii functional, feasible solutions can be found. The simulation results demonstrate that the EID based controller is effective and efficient to have the drill bit speed converge to its desired speed, maintain robustness under uncertainties, and also ensure convergence in trajectory tracking. Finally, it should be noted that the full state observer design needed in EID is a nontrivial task by itself given the high uncertainties associated with the drilling process. Further works will be pursued to ensure its robustness and accuracy in our future research.

4. CONTROL OF DIRECTIONAL DOWN-HOLE DRILLING PROCESS BASED ON DUAL HEURISTIC PROGRAMMING

After investigating the optimization and control of the vertical down-hole drilling system in Chapter 2 and Chapter 3, we shift our attention to the optimization and control of the directional down-hole drilling system. While DP can be customized for the vertical drilling control problem, it is computationally infeasible to be used in the directional drilling system, which inevitably has way more order. Therefore, we apply the approximate dynamic programming framework for the directional drilling control problem in this chapter.

Specifically, a single-neuron-adaptive-critic dual heuristic programming based controller is proposed for trajectory tracking and rate of penetration control of the directional down-hole drilling process. A finite element dynamics model is firstly customized and further formulated into the optimal control problem, then the DHP based controller is constructed in the finite receding horizon. Instead of searching all the states' and inputs' spaces, the SNAC-DHP approach uses one neural network to approximate the gradient of the cost-to-go function to obtain the optimal control inputs. The greatest advantage of using this approach is that the computational expenses will mostly depend on the convergence of the neural network no matter how many states and inputs this system has. Therefore, this approach can be used to solve the optimal control problem of the very high-dimensional system such as the directional drilling system. To this end, a series of simulations are conducted to evaluate the efficacy of this proposed controller. The robustness of this controller is also discussed, and the computational expenses also show the potential to apply this approach to other high-dimensional control problems.

4.1 Introduction

The productions of shale oil and natural gas were not feasible until recent technological breakthroughs such as directional drilling and hydraulic fracturing. As the critical com-

ponent for exploring down-hole energy resources, the down-hole drilling system has long suffered from detrimental vibrations such as "*stick-slip*," "*bit-bounce*," and "*whirl*," which cause energy dissipation, non-optimal production rate, and excessive wear of bit, bottom-hole-assembly, and drill string. Therefore, more optimal and reliable control is greatly needed for accurate trajectory tracking, mitigating vibrations, enhancing energy efficiency, and preventing drilling failures [14]. With the trend of deeper wells and more complex drilling environments, solving this control problem becomes increasingly challenging.

As shown in Fig. 4.1, the directional down-hole drilling system consists of a power unit on the surface, a long drill string connected by hundreds of pipes (can be over $10,000$ feet long in a 3-D space), bottom-hole-assembly (contains measurement sensors, and some may have actuations), and a down-hole drill bit for rock cutting. After the drilling power is generated on the surface, it forces the entire drill string and drill bit to both penetrate and rotate, which transmits the power from the surface through the drill string to the drill bit. Therefore, we consider the hook load force and top drive torque to be the primary control inputs of the down-hole drilling system, and the bit torsional and axial velocity to be the control outputs separated thousands of feet away from the control inputs. At the same time, with the large axial-to-radius ratio of the drill string as well as the nonlinearity in the bit-rock interaction, the down-hole drilling dynamics is generally considered as a nonlinear system with high-dimensional states. All these mentioned make the control design significantly more challenging.

Most of the existing studies on drilling control have focused on vertical drilling and can be divided into two categories: the lumped parameter system (LPS) models and the distributed parameter system models. For LPS models, a variety of control schemes are developed including (but not limited to) adaptive PID control [116], H_∞ robust control [99] [127], nonlinear control techniques such as sliding mode control [128] [117] [129] and back-stepping control [101] [130], etc. For the DPS models, control schemes such as linear matrix inequality based control [131], flatness based control [82], delayed PID control [132] are used.

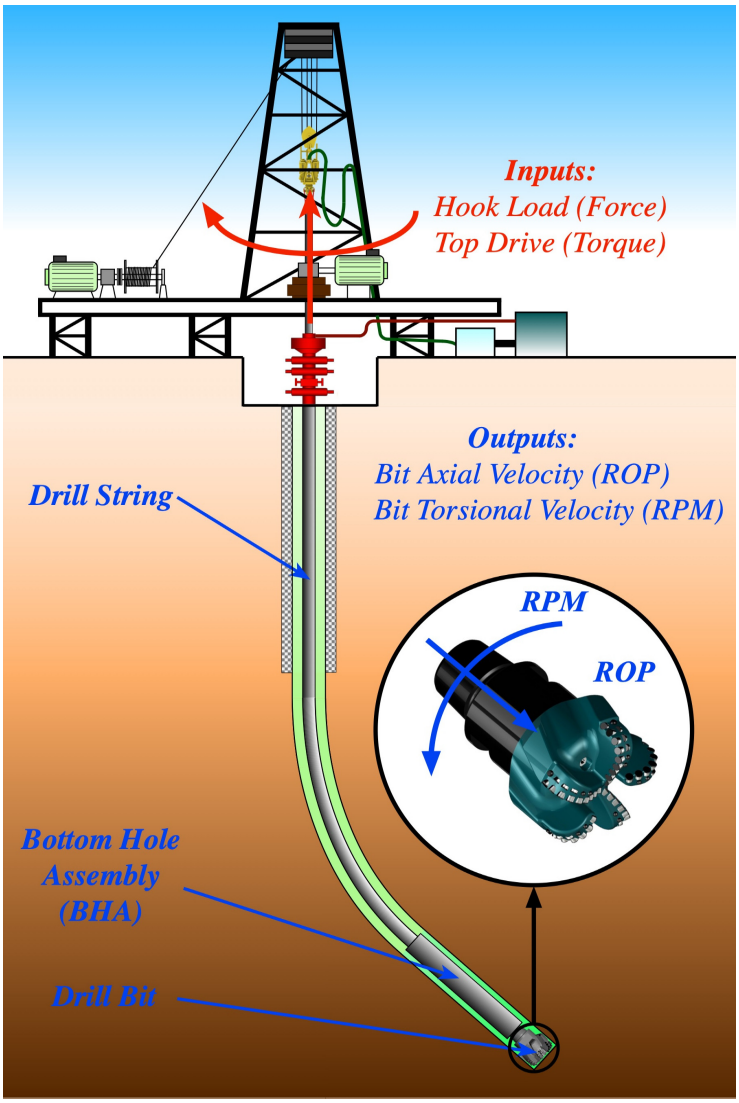

Figure 4.1 Schematic diagram of directional down-hole drilling system

However, the studies of the directional drilling control are very limited. Due to the large axial-to-radius ratio and complex three-dimensional geometry, the directional drilling dynamics can be either described as the partial differential equations [133], or the approximations of the PDEs such as finite element method [14] [134] [135], finite segment method (FSM) [136], finite difference method [137], etc. However, to design a proper controller for PDEs or high-dimensional ODEs models is non-trivial. For PDEs models, approaches such as the "*backstepping design*" [104] [138] and the "*predictor feedback design*" [139] are

generally used. The drawbacks of using the PDEs models for control design are in two manifolds. First, it needs a very specific form to design a proper controller. Second, if any additional boundary condition is added to the existing model, a complete controller redesign is needed. This is not only time consuming, but also challenging. For high-dimensional ODEs models, a majority of the designs used the proportional-integral controller to regulate the vibrations, such as [135] and [140]. Two types of stick-slip mitigation approach, "*soft torque/soft speed*" and "*Ztorque*," are commonly used [141], but their control performance can be degraded when the working conditions are changing. While more advanced nonlinear control schemes such as the Dynamic Programming approach [105] [119] have been developed for low-dimensional vertical drilling control, it is computationally intractable to directly implement it into a directional drilling control problem because of the so-called "*curse of dimensionality*" [109] [142].

In this chapter, we propose an approximate dynamic programming framework to solve the high-dimensional directional drilling control problem. Instead of searching for the "*optimal*" solution in all the discretized state and action spaces, the approximate dynamic programming framework uses the neural networks (NNs) as the function approximators to enable the optimal solution structure in an "*adaptive critic*" (AC) scheme [143]. After training these function approximators, the optimal control solution can be found when the neural network weights are converged. Compared to searching all the spaces in the traditional DP approach, the training of the neural network is considered relatively cheap in computational expenses, which is especially useful to deal with a high-dimensional control problem. To further reduce the computational expense, one type of ADP scheme, the single-neuron-adaptive-critic dual heuristic programming approach, is used in this chapter. The benefit of using SNAC-DHP is that it only requires training one neural network for the co-state, which is inherently more computationally efficient for the control design of high-dimensional systems such as the directional down-hole drilling system.

There are two main contributions in this chapter. First, the SNAC-DHP is applied to the

directional drilling control for the first time, which enables a computationally efficient control design for a high-dimensional dynamical system. Second, customized model approximation and non-dimensionalization are given in this paper to ensure efficient convergence in the control synthesis.

The organization of this chapter is listed as follows. In section 4.2, a directional drilling dynamics finite element model is presented. In section 4.3, the proposed model is customized for the implementation of the SNAC-DHP approach. In section 4.4, a series of simulations are conducted to demonstrate the feasibility of this ADP control scheme. In the end, the summary is drawn.

4.2 Problem Statement

As a widely-used modeling approach for the down-hole drilling system in the industry [69] [135] [144] [145], the finite element method has many advantages to model a geometrically complex structure with complex boundary conditions. Therefore, in this section, we construct a FEM dynamics model for the control design in section 4.3. As shown in Fig. 4.2, the entire drill string (Segment AD) can be modeled by the finite element method using a finite number of nodes.

4.2.1 Finite Element Model of Drill String

As shown in Fig. 4.2, the whole drill string is modeled by FEM, where the local motion vector $\boldsymbol{U}^i$ for node i contains 2 variables and can be denoted as:

$$\boldsymbol{U}_i^l(t) = \left[x_i^l(t),\ \alpha_i^l(t)\right]^T \tag{4.1}$$

where superscript l denotes the local coordinate variable; subscript $i \in [1, 2, \cdots, N]$ denotes the i^{th} node of the FEM nodes; thus x_i^l and α_i^l represent the local axial displacement and the local torsional displacement for node i, and the orientation of variables above can be found in Fig. 4.2.

The motion dynamics of the element (from node i to node $i+1$) can, therefore, be given

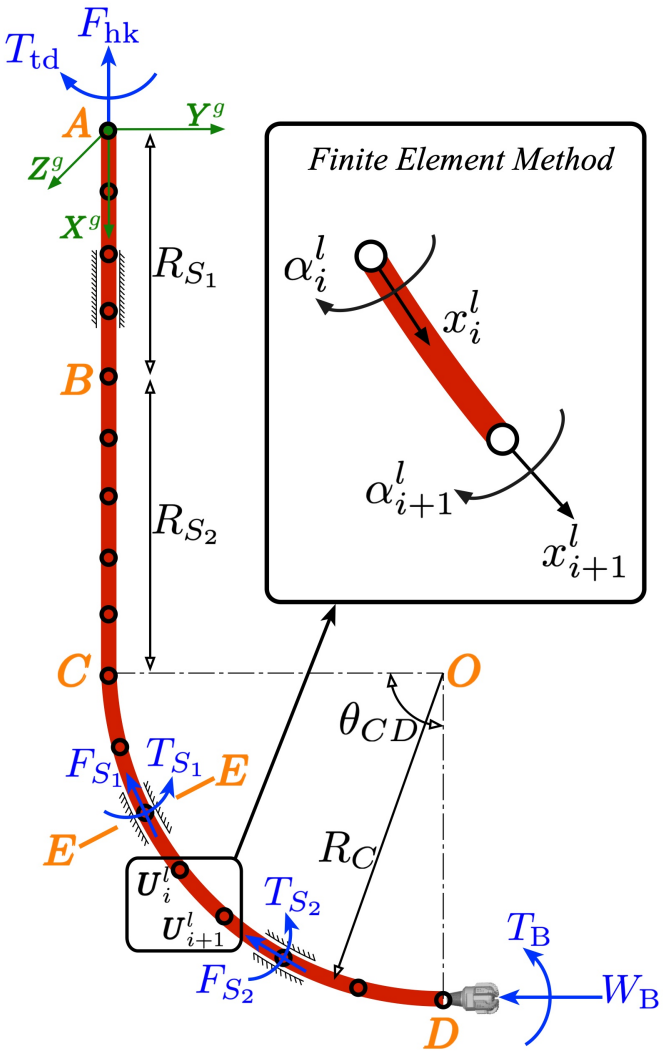

Figure 4.2 Schematic diagram of the finite element model of the directional drilling dynamics

as [146]:

$$\boldsymbol{M}^l\ddot{\boldsymbol{U}}^l_{\{i-i+1\}}(t)+\boldsymbol{D}^l\dot{\boldsymbol{U}}^l_{\{i-i+1\}}(t)+\boldsymbol{K}^l\boldsymbol{U}^l_{\{i-i+1\}}(t)=\boldsymbol{F}^l_{\{i-i+1\}}(t) \tag{4.2}$$

where $\boldsymbol{U}^l_{\{i-i+1\}}=\left[\boldsymbol{U}^l_i;\ \boldsymbol{U}^l_{i+1}\right]\in\mathbb{R}^{4\times1}$, $\boldsymbol{M}^l,\boldsymbol{D}^l,\boldsymbol{K}^l\in\mathbb{R}^{4\times4}$ are the inertia, damping, and stiffness matrices under the local coordinate for node i and i+1, and their detailed expressions can be found in [146]; $\boldsymbol{D}^l=\alpha_0\boldsymbol{M}^l+\beta_0\boldsymbol{K}^l$ is assumed to be the Raleigh damping; $\boldsymbol{F}^l_{\{i-i+1\}}\in\mathbb{R}^{4\times1}$ is the local external force and torque vector exerted on node i and node $i+1$.

The local coordinate motion vector $\boldsymbol{U}^l_{\{i-i+1\}}$ can be related to the global coordinate motion vector $\boldsymbol{U}^g_{\{i-i+1\}}$ as:

$$\boldsymbol{U}^l_{\{i-i+1\}}(t) = \boldsymbol{R}_i \cdot \boldsymbol{U}^g_{\{i-i+1\}}(t) \tag{4.3}$$

$$\boldsymbol{R}_i = \text{diag}\left[\boldsymbol{T}_i,\ \ \boldsymbol{T}_i,\ \ \boldsymbol{T}_i,\ \ \boldsymbol{T}_i\right],\ \boldsymbol{T}_i = \cos\left(x^l_i, X^g\right) \tag{4.4}$$

where $\cos\left(x^l_i, X^g\right)$ is the cosine of the angle between local coordinate axis x^l_i and global coordinate axis X^g (see Fig. 4.2), and the detailed derivations can be found in [14].

Therefore, Eq. (4.2) can be expressed in the global coordinate as:

$$\left(\boldsymbol{R}_i^T \boldsymbol{M}^l \boldsymbol{R}_i\right) \ddot{\boldsymbol{U}}^g_{\{i-i+1\}}(t) + \left(\boldsymbol{R}_i^T \boldsymbol{D}^l \boldsymbol{R}_i\right) \dot{\boldsymbol{U}}^g_{\{i-i+1\}}(t) + \left(\boldsymbol{R}_i^T \boldsymbol{K}^l \boldsymbol{R}_i\right) \boldsymbol{U}^g_{\{i-i+1\}}(t) = \left(\boldsymbol{R}_i^T\right) \boldsymbol{F}^l_{\{i-i+1\}}(t) \tag{4.5}$$

With Eq. (4.5), the augmented finite element dynamics of all the nodes can be written as:

$$\boldsymbol{M}^g \ddot{\boldsymbol{U}}^g(t) + \boldsymbol{D}^g \dot{\boldsymbol{U}}^g(t) + \boldsymbol{K}^g \boldsymbol{U}^g(t) = \boldsymbol{F}^g_{\text{ext}}(t) \tag{4.6}$$

where $\boldsymbol{M}^g$, $\boldsymbol{D}^g$, $\boldsymbol{K}^g$ are the global inertia, damping, and stiffness matrices as:

$$\boldsymbol{M}^g = \sum_{i=1}^{N} \boldsymbol{R}_i^T \boldsymbol{M}^l \boldsymbol{R}_i,\ \ \boldsymbol{D}^g = \sum_{i=1}^{N} \boldsymbol{R}_i^T \boldsymbol{D}^l \boldsymbol{R}_i,\ \ \boldsymbol{K}^g = \sum_{i=1}^{N} \boldsymbol{R}_i^T \boldsymbol{K}^l \boldsymbol{R}_i.$$

where $\boldsymbol{U}^g \in \mathbb{R}^{N_0 \times 1} (N_0 = 2N)$ is the state vector that includes all the nodes from Point A to Point D; $\boldsymbol{F}^g_{\text{ext}} \in \mathbb{R}^{N_0 \times 1}$ denotes the global external force vector, which is explained in detail in the following subsection.

4.2.2 External Forces of the Directional Down-Hole Drilling System

The external forces $\boldsymbol{F}^g_{\text{ext}}$ include surface control inputs (hook load and top drive torque), drill string/well-bore contact force and torque, bit/rock interaction force and torque, and the gravitational force.

4.2.2.1 Drill String/Well-bore Contact Model

Due to the inevitable contact of the curved drill string with the well-bore, the contact forces between the drill string and well-bore should be modeled. We assume that the critical contact forces are those in the axial and torsional direction since the axial and torsional dynamics are dominant in the drill string motion. Thus, only axial and torsional contact forces/torques are considered and the lateral ones are mainly to maintain the string in the well-bore. For drill string/well-bore contact location i, the axial force F_{S_i} and torsional torque T_{S_i} are given as:

$$\begin{cases} F_{S_i}(t) = \mu_w F^n_{S_i}(t)\cos(\phi_i(t)), \\ F^t_{S_i}(t) = \mu_w F^n_{S_i}(t)\sin(\phi_i(t)), \\ F^n_{S_i}(t) = -k_w \Delta(t)\mathbb{H}(\Delta(t)), \\ T_{S_i}(t) = R_w F^t_{S_i}(t). \end{cases} \tag{4.7}$$

where μ_w is the coefficient of friction between the well-bore and stabilizers; R_w is the radius of the stabilizer; $F^n_{S_i}$ and $F^t_{S_i}$ are normal and tangential components of the lateral force acting on the stabilizers, and are modeled using the Hertz contact theorem (see [135] [47] for details); k_w is the stiffness coefficient; $\mathbb{H}$ represents the Heaviside function; Δ is the elastic deformation; ϕ_i is the angle characterized by the relative moving direction of the stabilizer

with respect to the well-bore, and their cosine and sine functions are given as:

$$\begin{cases} \cos(\phi_i(t)) = \dfrac{\dot{x}_i^l(t)}{\sqrt{(\dot{x}_i^l(t))^2 + (R_w\dot{\alpha}_i^l(t))^2}}, \\ \sin(\phi_i(t)) = \dfrac{R_w\dot{\alpha}_i^l(t)}{\sqrt{(\dot{x}_i^l(t))^2 + (R_w\dot{\alpha}_i^l(t))^2}}. \end{cases} \tag{4.8}$$

4.2.2.2 Bit/Rock Interaction Model

A polycrystalline diamond compact bit/rock interaction model developed by Detournay et al. [8] is used in this chapter as:

$$\begin{cases} W_{\mathrm{B}}(t) = W_{\mathrm{B}_f}(t) + W_{\mathrm{B}_c}(t), \\ T_{\mathrm{B}}(t) = T_{\mathrm{B}_f}(t) + T_{\mathrm{B}_c}(t) \end{cases} \tag{4.9}$$

where W_{B} and T_{B} stand for the weight-on-bit and torque-on-bit, and they can be decomposed into the frictional component W_{B_f}, T_{B_f} and the cutting component W_{B_c}, T_{B_c}, respectively:

$$\begin{cases} W_{\mathrm{B}_f}(t) = \sigma l_w R_b d(t)/d^*, \\ W_{\mathrm{B}_c}(t) = \zeta\epsilon R_b d(t)\mathbb{H}(d(t)) \\ T_{\mathrm{B}_f}(t) = 0.5\mu\gamma R_b W_{\mathrm{B}_f}(t), \\ T_{\mathrm{B}_c}(t) = 0.5\epsilon R_b^2 d(t)\mathbb{H}(d(t)). \end{cases} \tag{4.10}$$

where σ is the maximum contact pressure at the wear-flat interface; l_w is the equivalent wear-flat length; R_b is the bit radius; ζ represents the bit geometry constant; ϵ is the intrinsic specific energy; μ represents the coefficient of friction at the wear-flat rock interface; γ is the geometric parameter of the bit; d^* is the critical depth of cut; d is the axial depth of cut,

and can be obtained as:

$$\begin{cases} d(t) = n_0\Big[x_N^l(t) - x_N^l(t-\tau_0)\Big] \\ \alpha_N^l(t) - \alpha_N^l(t-\tau_0) = 2\pi/n_0 \end{cases} \tag{4.11}$$

where x_N^l and α_N^l are bit axial and torsional displacement; τ_0 is the time delay used to model the motion gap between two neighboring blades on the bit [111].

As previously stated in subsection 2.2.3, the state-dependent representation of the axial depth of cut (Eq. (5.26)) can be approximated as:

$$d(t) = 2\pi \frac{\dot{x}_N^l(t)}{\dot{\alpha}_N^l(t)} \tag{4.12}$$

Note that the bit torsional velocity $\dot{\alpha}_N^l$ should be away from zero to avoid singularity in this approximation.

4.2.3 State Space Representation of the Directional Drilling Dynamics Model

In this subsection, the state space representation of the directional drilling dynamics model is formulated. Assume a new variable as:

$$\boldsymbol{z}(t) = [z_1, z_2, \cdots, z_{N_0}]^T = [\boldsymbol{U}^g(t);\ \dot{\boldsymbol{U}}^g(t)] \tag{4.13}$$

Then we can transform Eq. (4.6) into the following form as:

$$\frac{d}{dt}\boldsymbol{z}(t) = \boldsymbol{A}^g\boldsymbol{z}(t) + \boldsymbol{B}^g\boldsymbol{F}_{\text{ext}}^g(t) \approx \boldsymbol{A}_d^g\boldsymbol{z}(t) + \boldsymbol{B}_d^g\boldsymbol{F}_{\text{ext}}^g(t) \tag{4.14}$$

where $\boldsymbol{A}^g$ and $\boldsymbol{B}^g$ are the system matrices as:

$$\boldsymbol{A}^g = \begin{bmatrix} \boldsymbol{0} & \boldsymbol{I} \\ -\dfrac{\boldsymbol{K}^g}{\boldsymbol{M}^g} & -\dfrac{\boldsymbol{D}^g}{\boldsymbol{M}^g} \end{bmatrix}, \boldsymbol{B}^g = \begin{bmatrix} \boldsymbol{0} & -\dfrac{1}{\boldsymbol{M}^g} \end{bmatrix}^T.$$

$\boldsymbol{A}_d^g$ and $\boldsymbol{B}_d^g$ are the numerical approximations of $\boldsymbol{A}^g$ and $\boldsymbol{B}^g$ using the Taylor series expansion as:

$$\boldsymbol{A}_d^g = \sum_{i=0}^{m_t} (\boldsymbol{A}^g)^i \frac{(dt)^i}{i!}, \quad \boldsymbol{B}_d^g = \sum_{i=1}^{m_t} (\boldsymbol{A}^g)^{i-1} (\boldsymbol{B}^g) \frac{(dt)^i}{i!}. \tag{4.15}$$

where dt is the interval of the time samplings; m_t is the truncation number of the Taylor series expansion.

4.3 Optimal Control Design Using Dual Heuristic Programming

In this section, some preliminary procedures are conducted to facilitate the implementation of the dual heuristic programming approach. Then the optimal control problem for the directional drilling system is formulated, and the dual heuristic programming based controller is designed in the finite receding horizon.

4.3.1 Preliminary Procedures

In this subsection, some modifications are made based on the existing directional drilling dynamics model. Particularly, an approximate depth of cut and the non-dimensionalization of the state-space representation are adopted to ensure that all the system states are within the same level of magnitude, which ensures the fast training convergence of the neural network in the DHP based control design [147].

4.3.1.1 A Modification of the Depth of Cut Representation

As one of the common issues in the DHP based control design, the singularity can make the neural network hard to converge. This is because the infinitely large values of some states

will be used as the NN training basis and further result in divergence. In this example, the depth of cut representation in Eq. (4.12) becomes invalid when the bit torsional velocity is close to zero. To avoid this problem, a modification is made to the representation of the depth of cut as:

$$d(t) \approx 2\pi \frac{\dot{x}_N^l(t)}{\dot{\alpha}_N^l(t)} = 2\pi \frac{z_{\{N_0-1\}}(t)}{z_{N_0}(t)} \approx \begin{cases} 2\pi \dfrac{z_{\{N_0-1\}}(t)}{z_{N_0}(t)}, & \text{if } z_{N_0}(t) > \omega^\star \\ 2\pi \dfrac{z_{\{N_0-1\}}(t)}{\omega^\star}, & \text{otherwise} \end{cases} \tag{4.16}$$

where $\omega^\star$ is the critical torsional velocity.

Note that the approximated representation $2\pi \frac{\dot{x}_N^l(t)}{\dot{\alpha}_N^l(t)}$ is only valid when the torsional velocity is away from zero (properly controlled) [119]. As for the approximation in Eq. (4.16), the denominator is restricted within a minimum threshold to avoid the singularity in the system dynamics, which ensures a faster convergence rate in the neural network training process. Since the model with this modification is only used for control design (properly controlled), the above approximations are reasonably made to guarantee a faster convergence rate of the DHP based control design.

4.3.1.2 Non-dimensionalization of the Directional Drilling Dynamics Model

As a useful tool to assure the convergence of the neural network, the non-dimensionalization makes the magnitude of every state fall into the range of -1 to 1. Since these states will be used as the neural network basis functions, this procedure helps the neural network converge faster and more easily.

Assume a square matrix $\boldsymbol{\mathscr{P}} \in \mathscr{R}^{N_0 \times N_0}$ that contains all the maximum absolute value of each state in all the diagonal entries as:

$$\boldsymbol{\mathscr{P}} = \text{diag}\Big[\mathscr{P}_1, \mathscr{P}_2, \cdots, \mathscr{P}_{N_0}\Big] \tag{4.17}$$

Then we can define the non-dimensionalized state $\bar{z}_i$ as:

$$\bar{z}_i = \frac{z_i}{\mathscr{P}_i}, \quad i \in \{1, 2, \cdots, N_0\} \tag{4.18}$$

Since $\boldsymbol{\mathscr{P}}$ is non-singular, the non-dimensionalized drilling dynamics can be represented as:

$$\frac{d}{dt}\bar{\boldsymbol{z}}(t) = \left(\boldsymbol{\mathscr{P}}^{-1}\boldsymbol{A}_d^g\boldsymbol{\mathscr{P}}\right)\bar{\boldsymbol{z}}(t) + \left(\boldsymbol{\mathscr{P}}^{-1}\boldsymbol{B}_d^g\right)\boldsymbol{F}_{\text{ext}}^g(t) \tag{4.19}$$

where $\boldsymbol{\mathscr{P}}^{-1}\boldsymbol{A}_d^g\boldsymbol{\mathscr{P}}$ is the numerical approximation of the Jacobian matrix in the modified non-dimensionalized system dynamics.

4.3.2 Trajectory Tracking Control Problem Formulation

The non-dimensionalization model of drilling is in the control-affine form given as:

$$\dot{\bar{\boldsymbol{z}}} = f(\bar{\boldsymbol{z}}) + g(\bar{\boldsymbol{z}})\boldsymbol{u} \tag{4.20}$$

where $f : \mathbb{R}^{N_0 \times N_0} \to \mathbb{R}^{N_0}$ and $g : \mathbb{R}^{N_0} \to \mathbb{R}^2$ are functions to describe the non-dimensionalized drilling dynamics; $\bar{\boldsymbol{x}} \in \mathbb{R}^{N_0}$ and $\boldsymbol{u} \in \mathbb{R}^2$ are the non-dimensionalized state vector and the control input.

Suppose the reference signal in the local coordinate is given as:

$$\boldsymbol{r}^l(t) = [\overbrace{x_d, \alpha_d, \cdots, x_d, \alpha_d}^{N_0}, \overbrace{v_d, \omega_d, \cdots, v_d, \omega_d}^{N_0}]^T \tag{4.21}$$

where x_d and α_d are the desired local displacement for axial and torsional motion; v_d and ω_d are the desired local velocity for axial and torsional motion.

Thus we can transform the local reference signal into the global reference signal as:

$$\boldsymbol{r}^g(t) = \sum_{i=1}^{N} \boldsymbol{R}_i \cdot \boldsymbol{r}_i^l(t) \tag{4.22}$$

where $\boldsymbol{R}_i \in \mathbb{R}^{4\times4}$ is the rotation matrix mentioned in subsection 4.2.1; $\boldsymbol{r}_i^l(t) \in \mathbb{R}^{4\times1}$ is the local reference signal in a single finite element.

Then the non-dimensionalized reference signal in the global coordinate is stated as:

$$\bar{\boldsymbol{r}}(t) = \left[\frac{r_1^g(t)}{\mathscr{P}_1}, \frac{r_2^g(t)}{\mathscr{P}_2}, \cdots, \frac{r_{N_0}^g(t)}{\mathscr{P}_{N_0}}\right]^T \tag{4.23}$$

Therefore, the optimal solution of the above continuous-time (CT) system is to minimize the cost function below:

$$\begin{aligned} J = &\frac{1}{2}\Big[\bar{\boldsymbol{z}}(t_f) - \bar{\boldsymbol{r}}(t_f)\Big]^T \bar{\boldsymbol{S}}\Big[\bar{\boldsymbol{z}}(t_f) - \bar{\boldsymbol{r}}(t_f)\Big] + \\ &\frac{1}{2}\int_{t_0}^{t_f} \Big\{\Big[\bar{\boldsymbol{z}}(t) - \bar{\boldsymbol{r}}(t)\Big]^T \bar{\boldsymbol{Q}}\Big[\bar{\boldsymbol{z}}(t) - \bar{\boldsymbol{r}}(t)\Big] + \boldsymbol{u}(t)^T \bar{\boldsymbol{R}}\boldsymbol{u}(t)\Big\} dt \end{aligned} \tag{4.24}$$

where t_0 and t_f are the initial time and final time; $\bar{\boldsymbol{Q}} : \mathbb{R}^{N_0} \to \mathbb{R}$ is positive semi-definite and penalizes the states; $\bar{\boldsymbol{R}} \in \mathbb{R}^{2\times2}$ is positive definite and penalizes the control inputs; $\bar{\boldsymbol{S}} : \mathbb{R}^{N_0} \to \mathbb{R}$ is positive semi-definite and penalizes the final states. Once the minimal cost-to-go function is obtained, the optimal solution of the Eq. (4.20) can be found.

Since the discrete-time (DT) system is needed mostly for practical implementations, we derive the discrete-time system dynamics as follows:

$$\bar{\boldsymbol{z}}_{k+1} = f(\bar{\boldsymbol{z}}_k) + g(\bar{\boldsymbol{z}}_k)\boldsymbol{u}_k \tag{4.25}$$

where $k \in \mathbb{K}$ denotes the discrete-time index and $\mathbb{K} \in [0, 1, \cdots, n-1]$; $n = \frac{(t_f - t_0)}{dt}$ is the number of time samplings; $\bar{\boldsymbol{z}}_k$ and $\boldsymbol{u}_k$ are the state vector and the control input at discrete-time $k \cdot dt$.

Accordingly, the cost function for discrete-time systems can be related to the future state as:

$$J = \frac{1}{2}\sum_{k=0}^{n-1}\Big\{\Big[\bar{\boldsymbol{z}}_k - \bar{\boldsymbol{r}}_k\Big]^T \boldsymbol{Q}\Big[\bar{\boldsymbol{z}}_k - \bar{\boldsymbol{r}}_k\Big] + \boldsymbol{u}_k^T \boldsymbol{R}\boldsymbol{u}_k\Big\}dt + \frac{1}{2}\Big[\bar{\boldsymbol{z}}_n - \bar{\boldsymbol{r}}_n\Big]^T \boldsymbol{S}\Big[\bar{\boldsymbol{z}}_n - \bar{\boldsymbol{r}}_n\Big] \tag{4.26}$$

where $\boldsymbol{Q}$, $\boldsymbol{R}$, $\boldsymbol{S}$ are the penalty functions used in the discrete-time system for the states, control inputs, and final states, respectively: $\boldsymbol{Q} = \bar{\boldsymbol{Q}}dt$, $\boldsymbol{R} = \bar{\boldsymbol{R}}dt$, $\boldsymbol{S} = \bar{\boldsymbol{S}}dt$; $\bar{\boldsymbol{r}}_k$ is the discrete tracking reference signal.

We define the cost-to-go function $J_k(\bar{\boldsymbol{z}}_k)$ at the current step k as:

$$J_k(\bar{\boldsymbol{z}}_k) = \frac{1}{2}\Big[\bar{\boldsymbol{z}}_n - \bar{\boldsymbol{r}}_n\Big]^T \boldsymbol{S}\Big[\bar{\boldsymbol{z}}_n - \bar{\boldsymbol{r}}_n\Big] + \frac{1}{2}\sum_{j=k}^{n-1}\Big(\Big[\bar{\boldsymbol{z}}_k - \bar{\boldsymbol{r}}_k\Big]^T \boldsymbol{Q}\Big[\bar{\boldsymbol{z}}_k - \bar{\boldsymbol{r}}_k\Big] + \boldsymbol{u}_j^T \boldsymbol{R}\boldsymbol{u}_j\Big) \tag{4.27}$$

Thus the cost function recursion relationship from step $k+1$ to step k can be rewritten as:

$$J_k(\bar{\boldsymbol{z}}_k) = \frac{1}{2}\Big[\bar{\boldsymbol{z}}_k - \bar{\boldsymbol{r}}_k\Big]^T \boldsymbol{Q}\Big[\bar{\boldsymbol{z}}_k - \bar{\boldsymbol{r}}_k\Big] + \frac{1}{2}\boldsymbol{u}_k^T \boldsymbol{R}\boldsymbol{u}_k + J_{k+1}(\bar{\boldsymbol{z}}_{k+1}),\ \forall k \in \mathbb{K} \tag{4.28}$$

with the final cost-to-go function $J_n(\bar{\boldsymbol{z}}_n) = \frac{1}{2}\Big[\bar{\boldsymbol{z}}_n - \bar{\boldsymbol{r}}_n\Big]^T \boldsymbol{S}\Big[\bar{\boldsymbol{z}}_n - \bar{\boldsymbol{r}}_n\Big]$.

According to Bellman's "*Principle of Optimality* [109]," the optimal solution of the Hamilton-Jacobian-Bellman (HJB) equation minimizes the cost-to-go function $J_k(\bar{\boldsymbol{z}}_k)$. Here, we denote the optimal cost-to-go function as $J_k^\star(\bar{\boldsymbol{z}}_k)$ given by:

$$J_k^\star(\bar{\boldsymbol{z}}_k) = \min\left\{\frac{1}{2}\Big[\bar{\boldsymbol{z}}_k - \bar{\boldsymbol{r}}_k\Big]^T \boldsymbol{Q}\Big[\bar{\boldsymbol{z}}_k - \bar{\boldsymbol{r}}_k\Big] + \frac{1}{2}\boldsymbol{u}_k^T \boldsymbol{R}\boldsymbol{u}_k\right\} + J_{k+1}\Big(f(\bar{\boldsymbol{z}}_k) + g(\bar{\boldsymbol{z}}_k)\boldsymbol{u}_k\Big) \tag{4.29}$$

Define the co-state vector at step k as:

$$\boldsymbol{\lambda}_k = \frac{\partial J_k(\bar{\boldsymbol{z}}_k)}{\partial \bar{\boldsymbol{z}}_k} \tag{4.30}$$

Take the derivative of Eq. (4.28), we can rewrite the recursive relation of the co-state as:

$$\boldsymbol{\lambda}_k = \boldsymbol{Q}\Big(\bar{z}_k - \bar{\boldsymbol{r}}_k\Big) + \boldsymbol{A}_k^T \boldsymbol{\lambda}_{k+1} \tag{4.31}$$

where $\boldsymbol{A}_k = \frac{\partial \bar{\boldsymbol{z}}_{k+1}}{\partial \bar{\boldsymbol{z}}_k}$ is the Jacobian matrix of the non-dimensionalized directional drilling dynamics and can be approximated as $\boldsymbol{\mathscr{P}}^{-1}\boldsymbol{A}_d^g\boldsymbol{\mathscr{P}}$ (see subsection 4.3.1).

Note that the final cost-to-go function is firstly given as:

$$J_n(\bar{\boldsymbol{z}}_n) = \frac{1}{2}\Big[\bar{\boldsymbol{z}}_n - \bar{\boldsymbol{r}}_n\Big]^T \boldsymbol{S}\Big[\bar{\boldsymbol{z}}_n - \bar{\boldsymbol{r}}_n\Big] \tag{4.32}$$

Take the derivative of Eq. (4.33), the co-state at the final step is represented as:

$$\boldsymbol{\lambda}_n = \boldsymbol{S}\Big(\bar{\boldsymbol{z}}_n - \bar{\boldsymbol{r}}_n\Big) \tag{4.33}$$

The optimal control input $\boldsymbol{u}_k^\star$ satisfies the Bellman optimality condition $\frac{J_k(\bar{\boldsymbol{z}}_k)}{\boldsymbol{u}_k} = 0$, and can be calculated as:

$$\boldsymbol{u}_k^\star = -\boldsymbol{R}^{-1} g(\bar{\boldsymbol{z}}_k) \frac{J_{k+1}(\bar{\boldsymbol{z}}_{k+1})}{\bar{\boldsymbol{z}}_{k+1}} = -\boldsymbol{R}^{-1} g(\bar{\boldsymbol{z}}_k) \boldsymbol{\lambda}_{k+1} \tag{4.34}$$

4.3.3 Dual Heuristic Programming Algorithm

While both the traditional DP and DHP (one type of approximate dynamic programming) solve a complicated optimal control problem by breaking down into multiple subproblems, their approaches to obtain the optimal solution are inherently different.

This can be illustrated in Fig. 4.3. In traditional DP, first, all the states and inputs are discretized at each step. Then each grid at step $k+1$ will be projected into the state at step k using the discrete-time system dynamics and discretized control inputs. Of all the projections, we recorded the minimum cost-to-go and the control input (u_k'') as our optimal solution at this step. After obtaining the optimal solution for all the steps, the

overall optimal control solution can be formulated. The disadvantage using the traditional DP is that the computational expenses will increase exponentially when dealing with high-dimensional systems, which is called the "*curse of dimensionality*."

In contrast, DHP uses a neural network to approximate the gradient of the cost-to-go (refer to the co-state vector $\boldsymbol{\lambda}_{k+1}$), and the optimal control input can be found in Eq. (4.34). As a result, the computational expenses will not depend on the system dimension, and thus this approach does not suffer from the "*curse of dimensionality*."

In DHP based control design, the co-state vector $\boldsymbol{\lambda}_{k+1}$ can be approximated as a neural network as:

$$\boldsymbol{\lambda}_{k+1} = \boldsymbol{W}_k^T \phi(\bar{\boldsymbol{z}}_k), \;\; k \in \{0, 1, \cdots, n-1\} \tag{4.35}$$

where $\boldsymbol{W} \in \mathbb{R}^{p \times N_0}$ is the neural network weight matrix; $\phi : \mathbb{R}^{N_0} \to \mathbb{R}^p$ is the smooth basis function; p stands for the number of neural network basis/neurons.

Combine Eq. (4.31) and Eq. (4.33), we have the final condition $\boldsymbol{\lambda}_n^t$ as:

$$\boldsymbol{\lambda}_n^t = \boldsymbol{S}\Big(\bar{\boldsymbol{z}}_n - \bar{\boldsymbol{r}}_n\Big) \tag{4.36}$$

where superscript t stands for the number of trials in the neural network training process.

And the recursive relation at step $k+1$ can be rewritten as:

$$\boldsymbol{\lambda}_{k+1}^t = \boldsymbol{Q}\Big(\bar{\boldsymbol{z}}_{k+1} - \bar{\boldsymbol{r}}_{k+1}\Big) + \boldsymbol{A}_{k+1}^T \boldsymbol{\lambda}_{k+2}^t \tag{4.37}$$

Since the state at step $k+1$ can be stated in system dynamics as:

$$\bar{\boldsymbol{z}}_{k+1} = f(\bar{\boldsymbol{z}}_k) - g(\bar{\boldsymbol{z}}_k)\boldsymbol{R}^{-1} g(\bar{\boldsymbol{z}}_k)^T \boldsymbol{W}_k^T \phi(\bar{\boldsymbol{z}}_k) \tag{4.38}$$

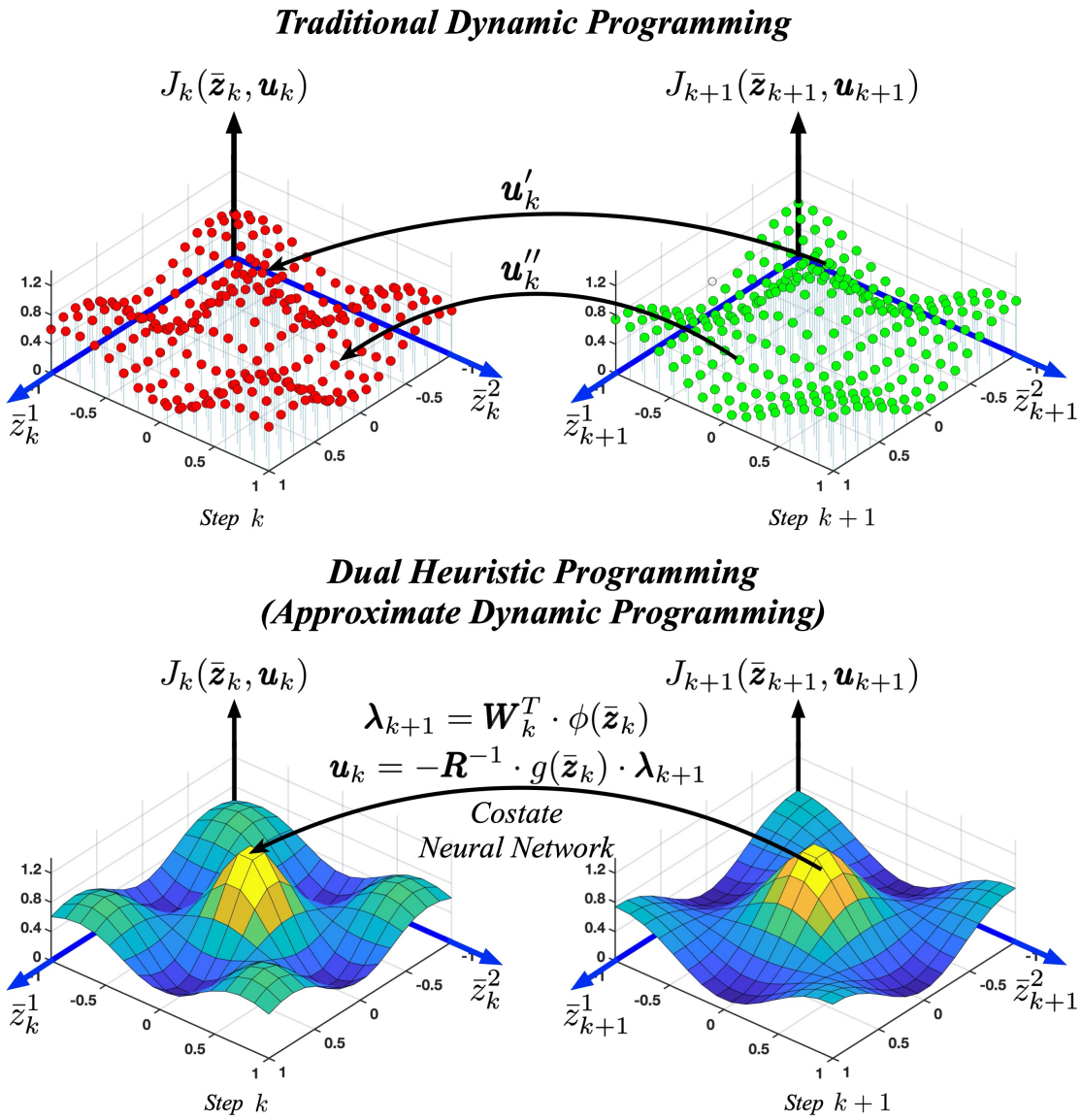

Figure 4.3 Comparison between the traditional dynamic programming and the dual heuristic programming (one type of approximate dynamic programming)

Substitute Eq. (4.38) into Eq. (4.36) and Eq. (4.37), we have:

$$\lambda_n^t = S\Big[f(\bar{z}_{n-1}) - g(\bar{z}_{n-1})R^{-1}g(\bar{z}_{n-1})^T \times W_{n-1}^T\phi(\bar{z}_{n-1}) - \bar{r}_n\Big] \tag{4.39}$$

$$\lambda_{k+1}^t = Q\Big[f(\bar{z}_k) - g(\bar{z}_k)R^{-1}g(\bar{z}_k)^T W_k^T\phi(\bar{z}_k) - \bar{r}_{k+1}\Big] + A_{k+1}^T W_{k+1}^T \phi\Big(f(\bar{z}_k) - g(\bar{z}_k)R^{-1}g(\bar{z}_k)^T W_k^T\phi(\bar{z}_k)\Big),$$

$$k \in \{0, 1, \cdots, n-2\} \tag{4.40}$$

Replace the co-state in the form of a neural network in Eq. (4.35), we can obtain Eqs. (4.39, 4.40) to create an iteration scheme (refer to [143] for the convergence proof) to find the neural network weight matrix $\boldsymbol{W}_k^T$ as:

$$\boldsymbol{W}_{n-1}^{i+1^T}\phi(\bar{\boldsymbol{z}}_{n-1}) = \boldsymbol{S}\Big[f(\bar{\boldsymbol{z}}_{n-1}) - g(\bar{\boldsymbol{z}}_{n-1})\boldsymbol{R}^{-1}g(\bar{\boldsymbol{z}}_{n-1})^T \times \boldsymbol{W}_{n-1}^T\phi(\bar{\boldsymbol{z}}_{n-1}) - \bar{\boldsymbol{r}}_n\Big] \tag{4.41}$$

$$\begin{aligned}\boldsymbol{W}_k^{i+1^T}\phi(\bar{\boldsymbol{z}}_k) \quad &= \boldsymbol{Q}\Big[f(\bar{\boldsymbol{z}}_k) - g(\bar{\boldsymbol{z}}_k)\boldsymbol{R}^{-1}g(\bar{\boldsymbol{z}}_k)^T\boldsymbol{W}_k^T\phi(\bar{\boldsymbol{z}}_k) - \bar{\boldsymbol{r}}_{k+1}\Big] \\ &+\boldsymbol{A}_{k+1}^T\boldsymbol{W}_{k+1}^T\phi\Big(f(\bar{\boldsymbol{z}}_k) - g(\bar{\boldsymbol{z}}_k)\boldsymbol{R}^{-1}g(\bar{\boldsymbol{z}}_k)^T\boldsymbol{W}_k^T\phi(\bar{\boldsymbol{z}}_k)\Big), \;\; k \in \{0, 1, \cdots, n-2\}\end{aligned} \tag{4.42}$$

where superscript in $\boldsymbol{W}_{n-1}^{i+1^T}$ denotes the training index of the neural network weight matrix.

During the training process, we define the training error vector at step k as the difference between the co-state at the $(t+1)^{\text{th}}$ iteration ($\boldsymbol{\lambda}_{k+1}^{t+1}$) and the co-state at the t^{th} iteration ($\boldsymbol{\lambda}_{k+1}^{t}$) as:

$$\boldsymbol{e}_k(\bar{\boldsymbol{z}}_k)^t = \boldsymbol{\lambda}_{k+1}^{t+1} - \boldsymbol{\lambda}_{k+1}^{t} \tag{4.43}$$

If the training error $\boldsymbol{e}_k(\bar{\boldsymbol{z}}_k)^t$ is becoming smaller and smaller, it means the neural network is converging. A threshold can be set to indicate that the neural network is trained. We denote $\boldsymbol{e}_k(\bar{\boldsymbol{z}}_k)$ as the converged training error given as:

$$\boldsymbol{e}_k(\bar{\boldsymbol{z}}_k) = \boldsymbol{\lambda}_{k+1} - \boldsymbol{\lambda}_{k+1}^{t} = \boldsymbol{W}_k^T\phi(\bar{\boldsymbol{z}}_k) - \boldsymbol{\lambda}_{k+1}^{t} \tag{4.44}$$

Then we can end the training trials at step k and proceed to the next time step.

Here, we summarize the SNAC-DHP algorithm in Algorithm 1 (N_I is the number of neural network training iterations).

Algorithm 1: Dual Heuristic Programming Algorithm [143]

initialization: initial guess $\boldsymbol{W}_{n-1}^{0}$;
for $j = 1 : N_I$ **do**
  Select random states $\boldsymbol{z}_{n-1}$;
  Calculate co-state $\boldsymbol{\lambda}_{n}^{t}$;
  Train NN weight $\boldsymbol{W}_{n-1}$ using $\boldsymbol{z}_{n-1}$ and $\boldsymbol{\lambda}_{n}^{t}$;
end
initialization: initial guess $\boldsymbol{W}_{k}^{0}$;
for $k = n-2$ *to* $k = 1$ **do**
  Select random states $\boldsymbol{z}_{k}$;
  Calculate co-state $\boldsymbol{\lambda}_{k+1}^{t}$;
  for $j = 1 : N_I$ **do**
    if $\boldsymbol{e}_k(\bar{\boldsymbol{z}}_k) <$ *threshold* **then**
      NN is converged, save $\boldsymbol{W}_{k}^{j}$;
    else
      Iterate and check error condition ;
    end
  end
end

4.4 Dual Heuristic Programming Simulation Results

In this section, a series of simulations are conducted to test the effectiveness of the proposed controller based on the dual heuristic programming. First, three different references are provided to test the trajectory tracking performance of this controller. Then the robustness of the proposed controller is studied using the varied parameter ϵ (intrinsic specific mechanical energy). In the end, the computational expenses are studied to show the advantages of this method in solving the high-dimensional optimal control problem.

The penalty matrices in the cost function (stated in Eq. (4.24)) are given as:

$$\boldsymbol{R} = \mathrm{diag}\Big[r_1^p, \quad r_2^p\Big],$$

$$\boldsymbol{Q} = \mathrm{diag}\Big[q_1^p, \quad q_2^p, \quad 0, \quad \cdots, \quad 0, \quad q_{N_1+1}^p, \quad q_{N_1+2}^p, \quad 0, \quad \cdots, \quad 0,$$
$$q_{2N_1+N_2-1}^p, \quad q_{2N_1+N_2}^p, \quad 0, \quad \cdots, \quad 0, \quad q_{N_0-1}^p, \quad q_{N_0}^p, \quad 0, \quad \cdots, \quad 0\Big],$$

$$\boldsymbol{S} = \text{diag}\Big[s_1^p,\ \ s_2^p,\ \ 0,\ \ \cdots,\ \ 0,\ \ s_{N_1+1}^p,\ \ s_{N_1+2}^p,\ \ 0,\ \ \cdots,\ \ 0,$$
$$s_{2N_1+N_2-1}^p,\ \ s_{2N_1+N_2}^p,\ \ 0,\ \ \cdots,\ \ 0,\ \ s_{N_0-1}^p,\ \ s_{N_0}^p,\ \ 0,\ \ \cdots,\ \ 0\Big]. \tag{4.45}$$

The co-state at step $k+1$ can be approximated as:

$$\boldsymbol{\lambda}_{k+1} = \boldsymbol{W}_k^T \phi(\bar{\boldsymbol{z}}) = W_k^{0^T} + \sum_{i=1}^{N} W_k^{i^T} \bar{z}_i \tag{4.46}$$

where $\phi(\bar{\boldsymbol{z}})$ is the function approximator basis: $\phi(\bar{\boldsymbol{z}}) = [1, \bar{z}_1, \bar{z}_2, \cdots, \bar{z}_{N_0}]^T$. According to the Weierstrass approximation theorem, this polynomial function approximator "*can approximate any continuously differentiable function to any degree of precision* [147] [148]."

And all the parameters of the drilling dynamics model used in this section are listed in Table 5.1 in Chapter 5.

4.4.1 Stick-slip and Bit-bounce Behaviors

In the practical operations, "*stick-slip*" describes the undesired phenomenon that the drill bit completely stops due to the excessive friction force and then suddenly slips to release the stored torsional energy. This behavior can do harm to the drilling components and pose a negative impact to the production rate. As shown in Fig. 4.4, the bit torsional velocity can exceed up to 2 or 3 times of the top drive torsional velocity. This is especially dangerous for the drill bit as well as the drill string since frequent torsional deformation may cause premature failures of the essential components of the drilling system. Similarly, the undesirable behavior in the axial dimension (called "*bit-bounce*") can also occur, which forces the bit to periodically collide with the rock and damage the drill bit.

4.4.2 Trajectory Tracking Performance Using the DHP-Based Optimal Controller

In this subsection, the designed DHP based controller is validated using the original finite element model. The previous mentioned "*stick-slip*" and "*bit-bounce*" phenomena will disappear, and the bit axial and torsional velocities will track the desired trajectories. In

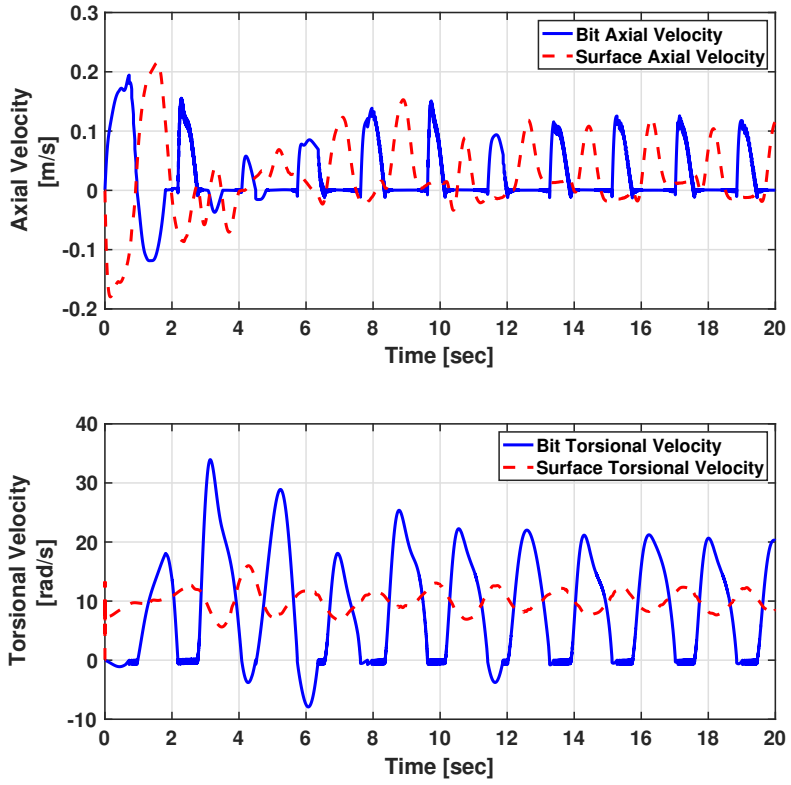

Figure 4.4 Stick-slip and bit-bounce behaviors of the drill bit motions

these simulations, the hyper-parameters used in the DHP control design are listed in Table 4.1 (N_S is the number of samples to train the neural network).

Table 4.1 Hyper-parameters used in dual heuristic programming based control design

Symbol	Value	Symbol	Value
N_I	20	s_1^p, s_2^p	1
N_S	200	$s_{N_1+1}^p, s_{N_1+2}^p$	1
r_1^p	10^{-11}	$q_{2N_1+N_2-1}^p, q_{N_0-1}^p,$	10^{10}
r_2^p	10^{-11}	$q_{2N_1+N_2}^p, q_{N_0}^p$	10^8
q_1^p, q_2^p	10	$s_1^p, s_{N_1+1}^p$	10^9
$q_{N_1+1}^p, q_{N_1+2}^p$	10	$s_2^p, s_{N_1+2}^p$	10^7

Figure 4.5 shows the evolution of the weights at step $N-1$ over neural network training iterations. Obviously, we can observe that the neural network weights are converged after 4 iterations. Figure 4.6 plots the trained weights over the simulation time (see the weights from the final time to the initial time since the optimal control problem is formulated in the finite receding horizon). It shows that the trained NN weight matrix (calculated control inputs) makes the system stabilized in about 2 sec.

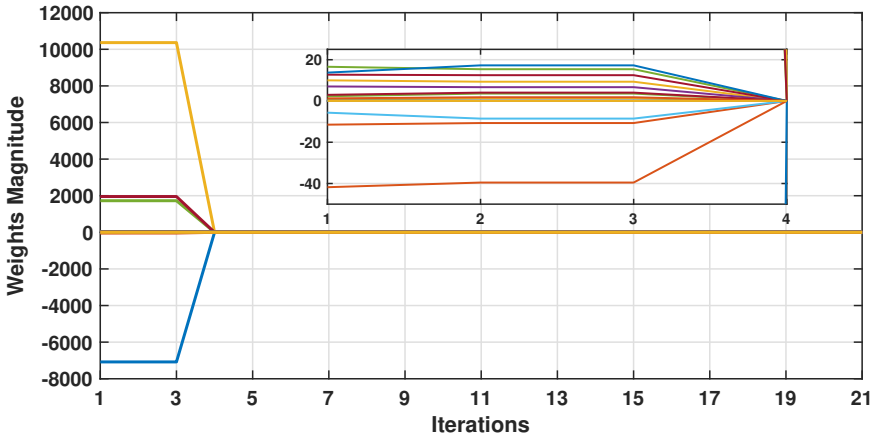

Figure 4.5 Weights versus iterations during neural network training

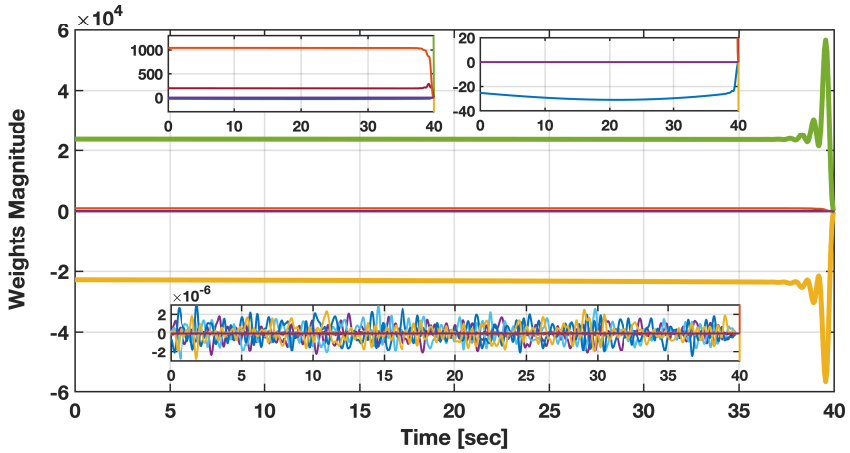

Figure 4.6 Trained weights versus time

Figure 4.7 shows the step response of drill bit axial and torsional velocities using the dual heuristic programming based controller (The desired bit axial and torsional velocities are selected as $v_d = 10$ mm/s and $\omega_d = 20$ rad/s). The result also shows that a burst occurs in the bit axial velocity from $0 \sim 2$ sec, and a quick jump is also observed in the bit torsional velocity right after a short stuck period from 0 to 2 sec. Eventually, both the bit axial and torsional velocities are stabilized to reach the desired constant references at around 5 sec.

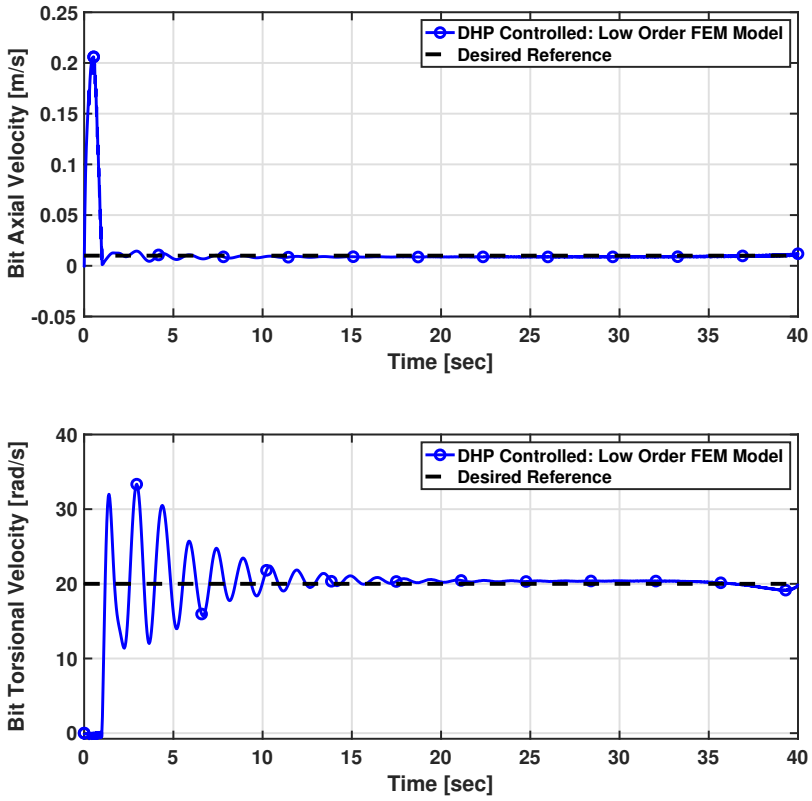

Figure 4.7 Step response of drilling states using DHP based controller

We've also tested the trajectory tracking performance given a ramp and a sinusoid reference (the units of v_d and ω_d are mm/s and rad/s), and the results are shown in Fig. 4.8 and Fig. 4.9.

The sinusoid reference is given as:

$$\begin{cases} v_d = 20 + 10\sin(0.1\pi t), \\ \omega_d = 40 + 20\sin(0.1\pi t). \end{cases} \tag{4.47}$$

The ramp reference is given as:

$$v_d = \begin{cases} 10, & \text{if} \quad 0 \le t < 0.25t_f \\ 10 + \frac{10(t-0.25t_f)}{0.25t_f}, & \text{if} \quad 0.25t_f \le t < 0.5t_f \\ 20, & \text{if} \quad 0.5t_f \le t < 0.75t_f \\ 20 - \frac{10(t-0.75t_f)}{0.25t_f}. & \text{if} \quad 0.75t_f \le t < t_f \end{cases} \tag{4.48}$$

$$\omega_d = \begin{cases} 20, & \text{if} \quad 0 \le t < 0.25t_f \\ 20 + \frac{20(t-0.25t_f)}{0.25t_f}, & \text{if} \quad 0.25t_f \le t < 0.5t_f \\ 40, & \text{if} \quad 0.5t_f \le t < 0.75t_f \\ 40 - \frac{20(t-0.75t_f)}{0.25t_f}. & \text{if} \quad 0.75t_f \le t < t_f \end{cases} \tag{4.49}$$

Similarly, the results in Fig. 4.8 and Fig. 4.9 show that the bit velocities will be stabilized shortly, and it will take around $5 \sim 10$ sec to track the desired references. Considering the average length of the drilling operations (usually takes hours or days), this controller is fast enough for the practical use.

The control efforts for three different reference tracking scenarios are provided in Fig. 4.10 and Fig. 4.11. For the axial control, results show that a large control effort happens during the first $0 \sim 3$ sec, which results in the fast jump of the bit axial velocity at that time. Meanwhile, a relatively large torque is maintained during the first $0 \sim 3$ sec to start rotating the drill string to the desired speed, and quickly decrease during $3 \sim 6$ sec to eliminate the rotating speed overshoot. When the bit axial/torsional velocities become stable after $6 \sim 8$ sec, both the axial and torsional efforts are stabilized.

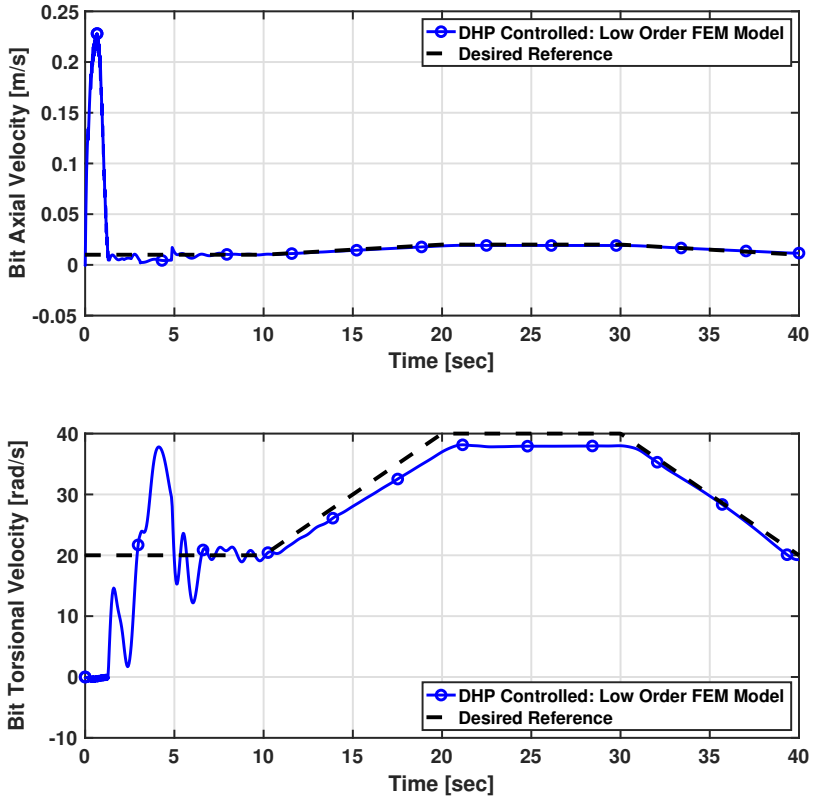

Figure 4.8 Trajectory tracking performance under DHP based controller given a ramp reference

4.4.3 Parameter Variation Analysis

In this subsection, the robustness of the proposed DHP based controller is investigated. The robustness performance is validated using a perturbed intrinsic specific energy parameter ϵ (ranging from 50% to 300% of the nominal value 45 MPa).

Figure 4.12 shows the bit velocity response over the varied parameter ϵ using the same DHP based controller. The result shows that the DHP based controller maintains robustness when the bit-rock interaction parameter ϵ is varied.

4.4.4 Computational Expense

Due to the "*curse of dimensionality*," the traditional DP is computationally intractable for the high-dimensional systems even though it provides a procedural approach to solve

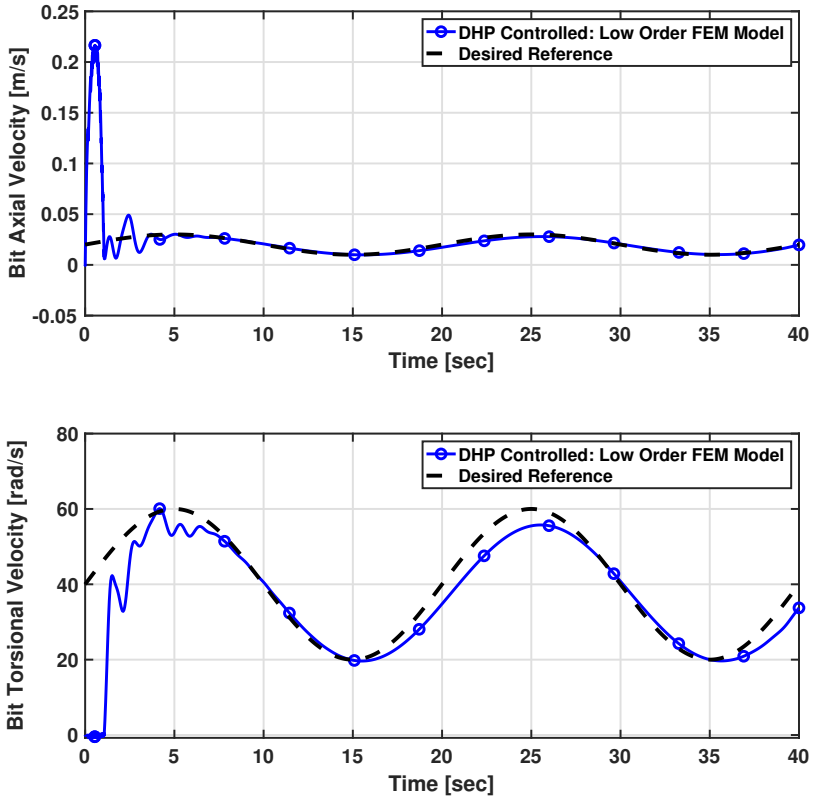

Figure 4.9 Trajectory tracking performance under DHP based controller given a sinusoid reference

the optimal control problem. The dual heuristic programming (one type of approximate dynamic programming), however, is computationally feasible to solve these high-dimensional optimal control problems because the principle behind DHP is inherently different from the traditional DP. Rather than comparing and storing all the discrete values of cost-to-go functions, DHP uses a single neural network to approximate the gradient of the cost-to-go function. Therefore, the computational expenses will directly depend on the neural network training speed, rather than the system dimension.

In this subsection, a laptop environment (CPU: i7-9750H 2.6GHz 6-core, RAM: 16GB) is used to study the computational expenses of the proposed dual heuristic programming based control algorithm, and we summarize the results in Table 4.2.

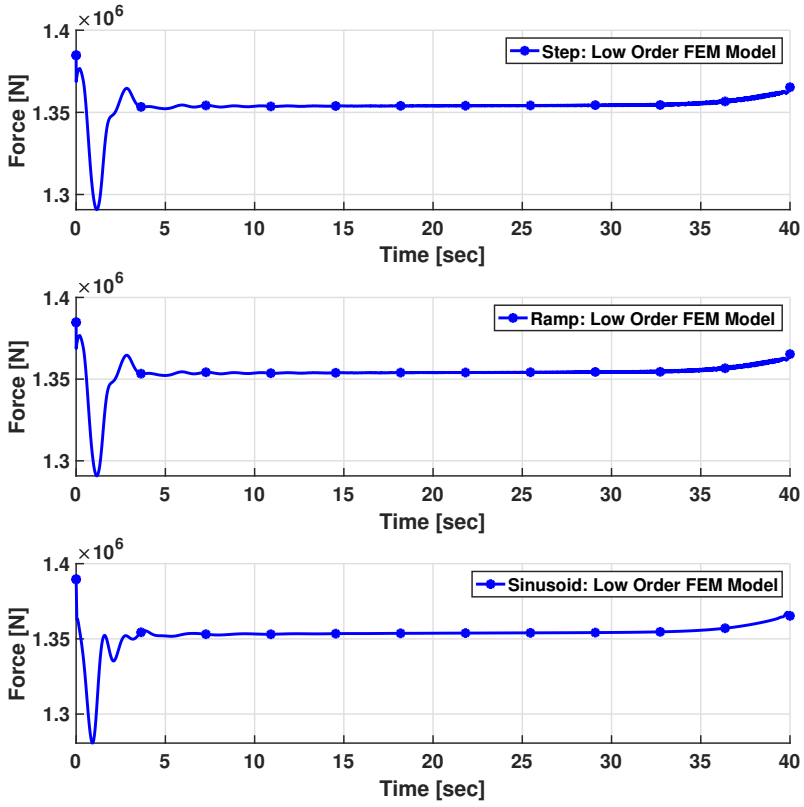

Figure 4.10 Axial control efforts for three different references

Table 4.2 Computational expenses using traditional dynamic programming and dual heuristic programming

Method	Time Interval	State No.	Samples	Simulation (40 s)
DP [119]	0.05 s	4	$10 \times 10 \times 10 \times 10$	259.91 s
DP [119]	0.05 s	4	$20 \times 20 \times 10 \times 10$	3516.27 s
DHP	0.001 s	24	100	148.69 s
DHP	0.001 s	24	200	157.30 s
DHP	0.001 s	80	200	233.68 s

Table 4.2 and Figure 4.13 compare the computational expenses between the DP and DHP (ADP) with different time intervals. The result shows the differences between the computationally efficient DP proposed in [119] and the proposed DHP based control in the

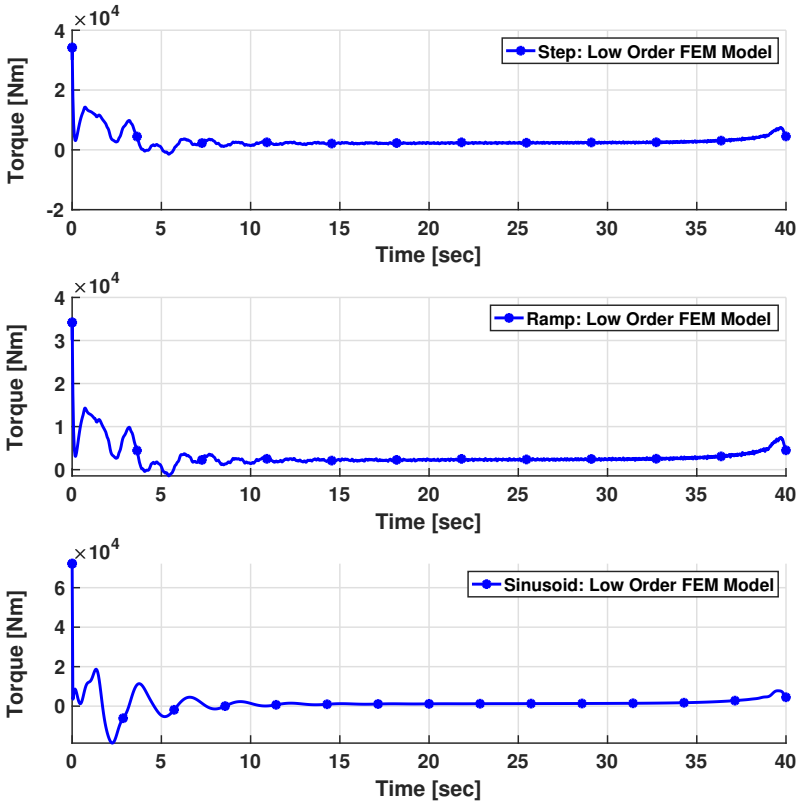

Figure 4.11 Torsional control efforts for three different references

following:

- The computationally efficient DP has a much larger time interval (0.05 sec) than the DHP control proposed in this chapter (0.001 sec).

- The DHP based control can deal with a much higher dimension (24 and 80 number of states are tested) than the computationally efficient DP (4 states in [119]).

- The computational expenses in DP are very sensitive to the discretization density, while the computational expenses using DHP are not very sensitive to the number of samples.

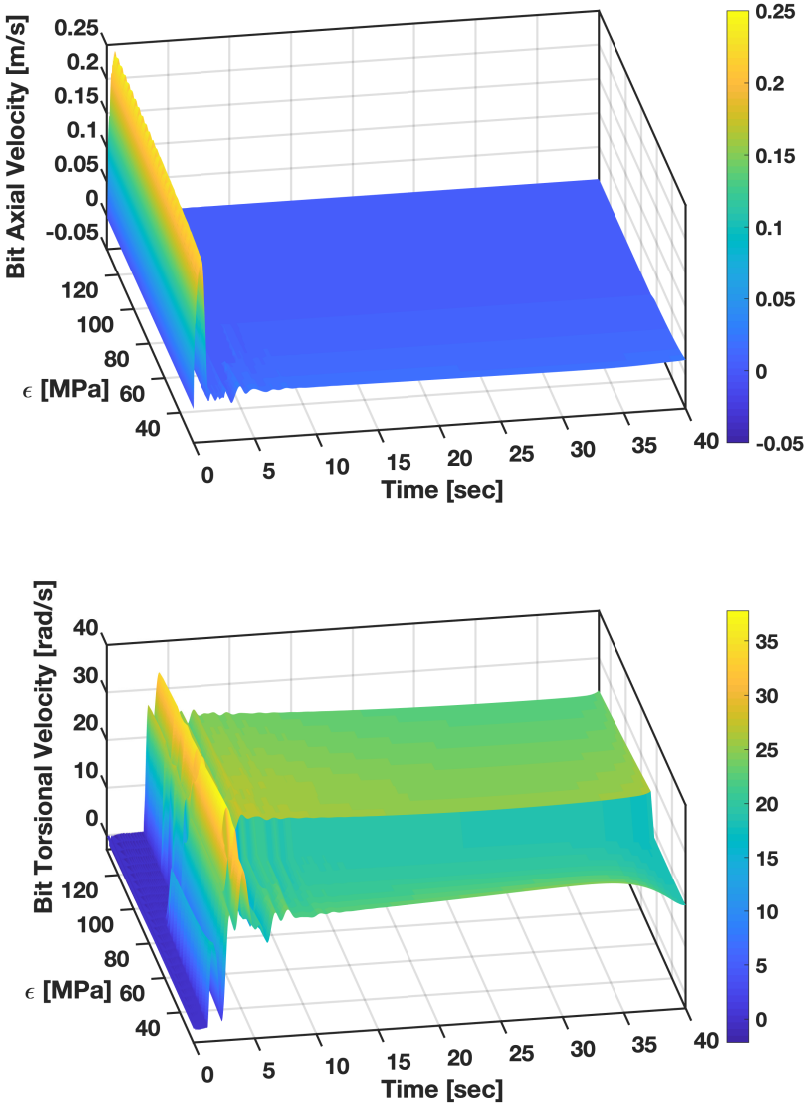

Figure 4.12 Bit velocity response over varied parameter ϵ with DHP based controller

This demonstrates that the DHP based control can effectively solve the high dimensional optimal control problem without having a significant increase in the computational efforts.

4.5 Summary

A dual heuristic programming based controller is designed using a FEM directional down-hole drilling dynamics model. One of the advantages of using DHP is that it can be used to overcome the "*curse of dimensionality*" in a high-dimensional optimal control problem. To train the neural network faster in the DHP control design, some customizations have been made to the original directional down-hole drilling dynamics. In the end, a series of simulation results demonstrate that the proposed DHP based controller can effectively eliminate the vibrations in both axial and torsional dimensions, accurately track desired trajectories, as well as maintain robustness with parameter variations.

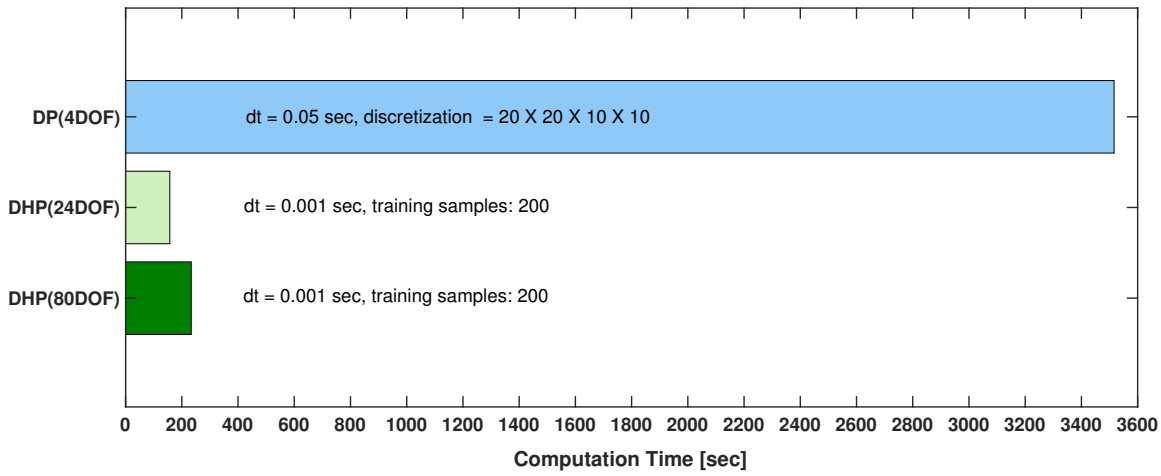

Figure 4.13 Computational expenses comparison using DP and DHP(ADP)

5. A HYBRID DIRECTIONAL DRILLING DYNAMICS MODEL INTEGRATING FINITE ELEMENT AND TRANSFER MATRIX*

With the DHP based controller designed in Chapter 4, a high-fidelity yet computationally efficient higher-order directional drilling dynamics model is also needed for control validation. This dynamics model should be in high-fidelity, and can also be conveniently integrated into a real-time testbed such as software-in-the-loop (SIL) system and hardware-in-the-loop (HIL) system. Therefore, we develop a hybrid directional drilling dynamics model in this chapter.

Due to the long dimension of the drill string, a traditional drilling dynamics model based on pure numerical methods such as the finite element method may require a large number of meshes, which induces high computational intensity. By using a hybrid method combining the finite element method and the transfer matrix method, the order of the model can be significantly reduced. Meanwhile, the sensitivity analysis is conducted to ascertain the number of states needed to accurately describe the directional drilling dynamics. To this end, simulation results are presented to prove that the proposed hybrid modeling method can effectively capture the dominant modes of the large scale drill string dynamics, and a computationally-efficient and high-fidelity hybrid model can be reached for further real-time control validation in the software-in-the-loop system or hardware-in-the-loop system.

5.1 Introduction

Recent advancements in directional drilling and hydraulic fracking technologies have enabled a more efficient and cost-effective recovery of unconventional energy resources, such as shale oil and gas. This trend has significantly increased the accessible global energy reserve since the unconventional resources were hard to extract decades ago. This trend also urges

*Reprinted with permission from "Computationally Efficient Down-Hole Drilling System Dynamics Modeling Integrating Finite Element and Transfer Matrix," by **C. Ke** and X. Song, *ASME Transactions on Journal of Dynamic Systems, Measurement and Control* 139.12 (2017): 121003, Copyright 2017 by ASME Publisher

further research and developments in down-hole energy exploration and production technologies. Particularly for the directional drilling systems, which drill a three-dimensional well-bore to reach the oil and gas reservoir, major research efforts have recently been spent on automating the drilling process with accurate trajectory control, vibration mitigation, and reliable down-hole condition monitoring. These needs also motivate research on a reliable and real-time drilling dynamics model for state observer design [112] and real-time control synthesis.

As shown in Fig. 5.1, the directional drilling system is typically composed of power and actuation units on the top end (surface), a drill string connecting the top drive to the bottom-hole-assembly, drill collars, BHA that houses down-hole electronics and actuation systems, and drill bits at the bottom. In particular, the drill string is typically very long (can be over ten thousand feet) and can have three-dimensional curved geometry. This feature makes a computationally efficient dynamics modeling challenging. For a wide class of numerical modeling methods such as finite element methods [135], modal methods, and finite rigid body [149] approaches, a large number of meshes are inevitably required and thus result in high computational burden. Thus, many existing works on drilling dynamics modeling are for off-line analysis or pre-job planning [150]. On the other hand, some other control-oriented modeling works are either only for vertical drilling [80], or modeling the entire string using only one or a few spring-mass-dampers [2] [111], which can significantly degrade the modeling accuracy [42]. Therefore, a directional drilling dynamics model that has both computational-efficiency and high-fidelity is important for further research on real-time control and down-hole condition monitoring.

To enable such a model for directional drilling, we adopt two strategies in this chapter. The first is to use a hybrid modeling method integrating a numerical solution with an analytical solution. Despite being long and three-dimensional, many segments of the drill string are close to a piecewise straight slender beam. The straight portion can be analytically modeled using TMM and thus can be addressed in a computationally efficient fashion. The

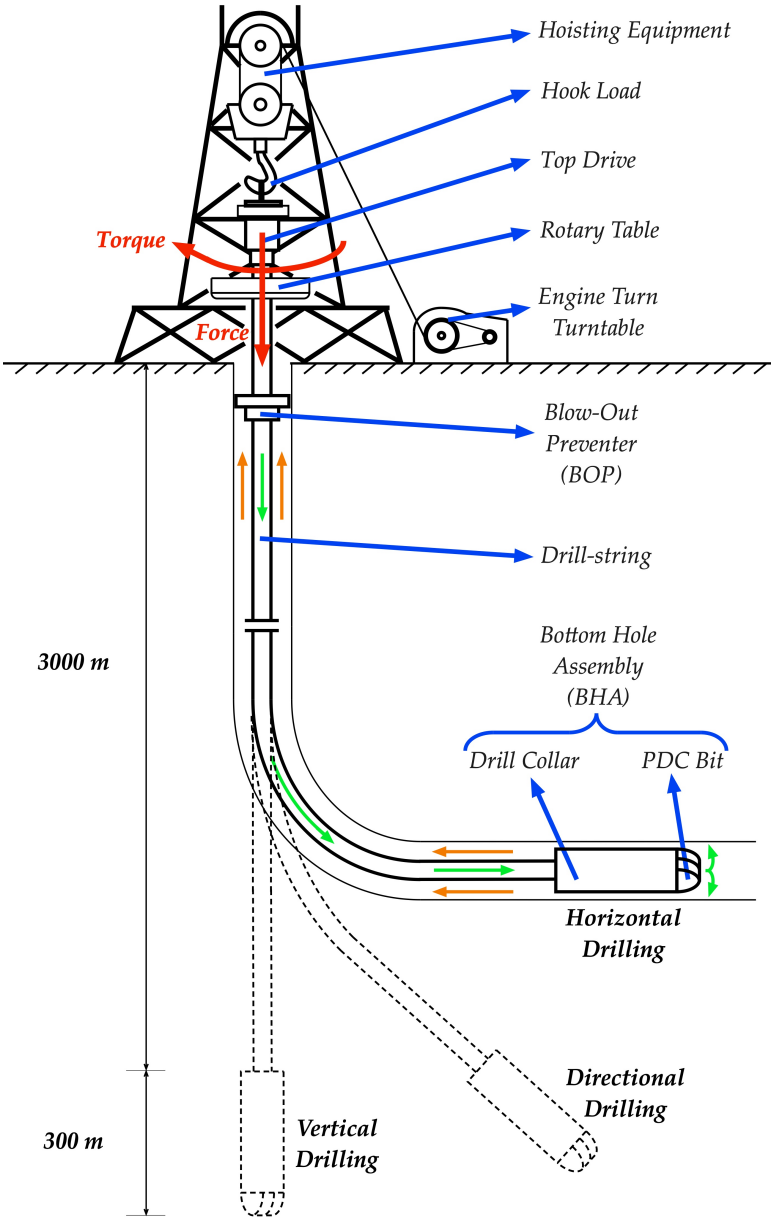

Figure 5.1 Schematics diagram of the directional down-hole drilling system

curved portion can be numerically modeled using FEM for higher fidelity. The two modeling techniques can be integrated through a hybrid modeling method. Second, to further reduce the model order, we will use the hybrid model with an adequate number of nodes in the control design. To determine the number of nodes needed for an accurate modeling result in this chapter, we compare the simulation results using the proposed hybrid model in different

node numbers. The simulation results show that the proposed hybrid model can effectively replicate the critical vibrational phenomenon observed in drilling fields, and a consistent result can be achieved using the hybrid model in different node numbers.

The organization of this chapter is listed as follows. In section 5.2, an overview of the hybrid model integrating finite element and transfer matrix is presented. Section 5.3 shows a series of numerical simulation results in terms of modeling accuracy, sensitivity, and computational efficiency of the hybrid model. To this end, a summary of this chapter is presented.

5.2 Directional Drilling Dynamics Modeling Using a Hybrid Method Integrating Finite Element and Transfer Matrix

The directional drilling dynamics is first modeled using a hybrid modeling method, which integrates the transfer matrix method and the finite element method. The basic idea is to divide a geometrically complex drill string into several "*curved segments*" and "*straight segments*."

As shown in Fig. 5.2, the straight and uniform portion (Segment BC) can be modeled by the transfer matrix method and the curved (Segment CD) or non-uniform portion (Segment AB) (the top portion containing the top drive and rig elements) can be modeled by finite element method. TMM offers an "*analytical*" solution for a single dimension beam structure under the wave-propagation theory, so it is computationally efficient. However, this approach can be effective only when the object to be modeled is straight or slightly curved and has a constant cross-sectional area and a uniform material property. On the other hand, FEM is well-established for systems with complex structures [69] [135] [144] [145] but can be computationally intensive for large scale systems. Combining them together results in a hybrid method that can lower the order of the dynamical model while maintaining the modeling accuracy. Due to the long dimensionality and large axial-to-radial ratio of the drill string geometry, such a hybrid method fits well for the directional drilling dynamics modeling.

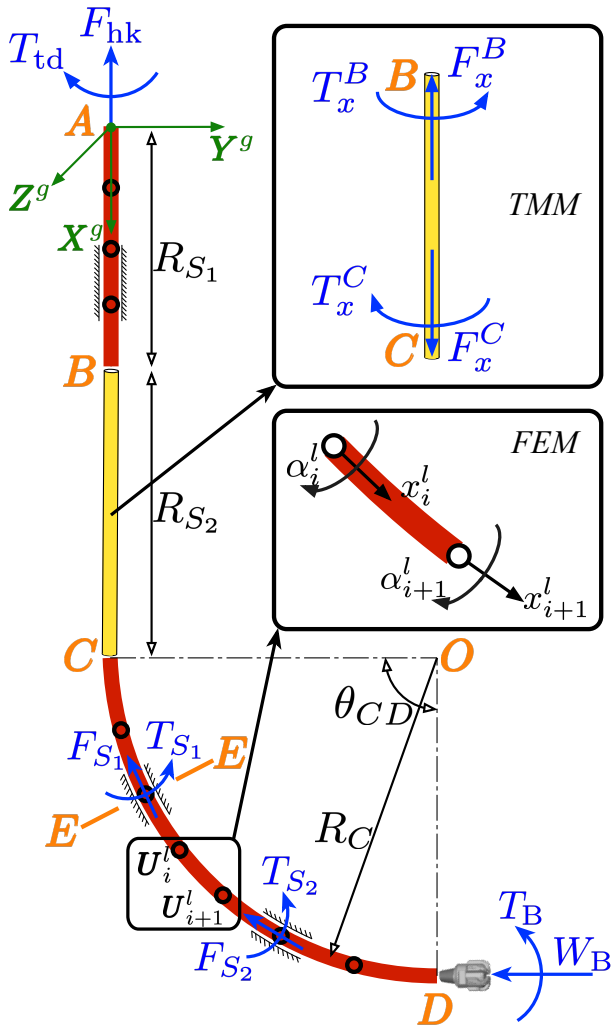

Figure 5.2 Schematics of the computationally efficient directional drilling dynamics modeling integrating FEM and TMM

5.2.1 Finite Element Model for the Curved Segments of Drill String

As shown in Fig. 5.2, in the segment modeled by FEM, the local motion vector $\boldsymbol{U}^i$ for node i contains 2 variables and can be denoted as:

$$\boldsymbol{U}_i^l(t) = \left[x_i^l(t),\ \alpha_i^l(t)\right]^T \tag{5.1}$$

where superscript l denotes the local coordinate variable; subscript $i = (1, 2, \cdots, N)$ denotes the i^{th} node of of all the nodes; thus x_i^l and α_i^l represent the local axial displacement and the

local torsional displacement for node i, and the orientation of variables above can be found in Fig. 5.2.

The motion dynamics of the element (from node i to node $i+1$) can, therefore, be given as [146]:

$$\boldsymbol{M}^l \ddot{\boldsymbol{U}}^l_{\{i-i+1\}}(t) + \boldsymbol{D}^l \dot{\boldsymbol{U}}^l_{\{i-i+1\}}(t) + \boldsymbol{K}^l \boldsymbol{U}^l_{\{i-i+1\}}(t) = \boldsymbol{F}^l_{\{i-i+1\}}(t) \tag{5.2}$$

where $\boldsymbol{U}^l_{\{i-i+1\}} = \left[\boldsymbol{U}^l_i;\ \boldsymbol{U}^l_{i+1}\right] \in \mathbb{R}^{4\times 1}$, $\boldsymbol{M}^l, \boldsymbol{D}^l, \boldsymbol{K}^l \in \mathbb{R}^{4\times 4}$ are the inertia, damping and stiffness matrices under the local coordinate for node i and i+1, and their detailed expressions can be found in [146]; $\boldsymbol{D}^l = \alpha_0 \boldsymbol{M}^l + \beta_0 \boldsymbol{K}^l$ is assumed to be the Raleigh damping; $\boldsymbol{F}^l_{\{i-i+1\}} \in \mathbb{R}^{4\times 1}$ is the local external force and torque vector exerted on node i and node $i+1$.

The local coordinate motion vector $\boldsymbol{U}^l_{i-i+1}$ can be related to the global coordinate motion vector $\boldsymbol{U}^g_{i-i+1}$ as:

$$\boldsymbol{U}^l_{i-i+1}(t) = \boldsymbol{R}_i \boldsymbol{U}^g_{i-i+1}(t) \tag{5.3}$$

$$\boldsymbol{R}_i = \mathrm{diag}\left[\boldsymbol{T}_i,\ \ \boldsymbol{T}_i,\ \ \boldsymbol{T}_i,\ \ \boldsymbol{T}_i\right],\ \boldsymbol{T}_i = \cos\left(x^l_i, X^g\right) \tag{5.4}$$

where $\cos\left(x^l_i, X^g\right)$ is the cosine of the angle between local coordinate axis x^l_i and global coordinate axis X^g (see Fig. 5.2), and the detailed derivations can be found in [14].

Therefore, Eq. (5.2) can be expressed in the global coordinate as:

$$\left(\boldsymbol{R}_i^T \boldsymbol{M}^l \boldsymbol{R}_i\right) \ddot{\boldsymbol{U}}^g_{\{i-i+1\}}(t) + \left(\boldsymbol{R}_i^T \boldsymbol{D}^l \boldsymbol{R}_i\right) \dot{\boldsymbol{U}}^g_{\{i-i+1\}}(t) + \left(\boldsymbol{R}_i^T \boldsymbol{K}^l \boldsymbol{R}_i\right) \boldsymbol{U}^g_{\{i-i+1\}}(t) = \left(\boldsymbol{R}_i^T\right) \boldsymbol{F}^l_{\{i-i+1\}}(t) \tag{5.5}$$

With Eq. (5.5), the augmented finite element dynamics of all the nodes can be written as:

$$\boldsymbol{M}^g \ddot{\boldsymbol{U}}^g(t) + \boldsymbol{D}^g \dot{\boldsymbol{U}}^g(t) + \boldsymbol{K}^g \boldsymbol{U}^g(t) = \boldsymbol{F}^g_{\mathrm{ext}}(t) \tag{5.6}$$

where $\boldsymbol{M}^g$, $\boldsymbol{D}^g$, $\boldsymbol{K}^g$ are the global inertia, damping, and stiffness matrices, and can be given as:

$$\boldsymbol{M}^g = \begin{bmatrix} \boldsymbol{M}_1^g & \\ & \boldsymbol{M}_2^g \end{bmatrix}, \boldsymbol{D}^g = \begin{bmatrix} \boldsymbol{D}_1^g & \\ & \boldsymbol{D}_2^g \end{bmatrix}, \boldsymbol{K}^g = \begin{bmatrix} \boldsymbol{K}_1^g & \\ & \boldsymbol{K}_2^g \end{bmatrix}.$$

where $\boldsymbol{M}_1^g, \boldsymbol{D}_1^g, \boldsymbol{K}_1^g$ stand for the global inertia, damping, and stiffness matrices for the FEM segment AB; $\boldsymbol{M}_2^g, \boldsymbol{D}_2^g, \boldsymbol{K}_2^g$ stand for the global inertia, damping, and stiffness matrices for the FEM segment CD:

$$\begin{cases} \boldsymbol{M}_1^g = \sum_{i=1}^{N_1} \boldsymbol{M}_1^l, \quad \boldsymbol{M}_2^g = \sum_{i=1}^{N_2} \boldsymbol{R}_i^T \boldsymbol{M}_2^l \boldsymbol{R}_i, \\ \boldsymbol{D}_1^g = \sum_{i=1}^{N_1} \boldsymbol{D}_1^l, \quad \boldsymbol{D}_2^g = \sum_{i=1}^{N_2} \boldsymbol{R}_i^T \boldsymbol{D}_2^l \boldsymbol{R}_i, \\ \boldsymbol{K}_1^g = \sum_{i=1}^{N_1} \boldsymbol{K}_1^l, \quad \boldsymbol{K}_2^g = \sum_{i=1}^{N_2} \boldsymbol{R}_i^T \boldsymbol{K}_2^l \boldsymbol{R}_i. \end{cases}$$

where N_1 and N_2 are the number of nodes for segment AB and CD; $\boldsymbol{U}^g = [\boldsymbol{U}_1^g; \boldsymbol{U}_2^g] \in \mathbb{R}^{N_0 \times 1}$ is the state vector; $\boldsymbol{F}_{\text{ext}}^g \in \mathbb{R}^{N_0 \times 1} (N_0 = 2(N_1 + N_2))$ denotes the global external force vector, and will be explained in detail in subsection 5.2.3.

5.2.2 Transfer Matrix Method for the Uniform and Straight Segment of Drill String

For the uniform and straight segment of the drill string (BC in Fig. 5.2), we can use the transfer matrix method to analytically express the relation of the motion and force/torque vectors between the end nodes of the segment. According to the wave propagation theory [151], the axial wave equation for straight and uniform beam section is given as:

$$\frac{\partial^2 x}{\partial x_l^2} = \frac{\rho}{E} \cdot \frac{\partial^2 x}{\partial t^2} = \frac{1}{c_L^2} \cdot \frac{\partial^2 x}{\partial t^2} \tag{5.7}$$

where x_l stands for the axial direction in the local coordinate; t denotes time; E is Young's modulus, and ρ is the density of the propagation medium. From Eq. (5.7), the transfer

matrix in the axial direction can be obtained as [151] [103]:

$$\begin{bmatrix} x^C(\omega) \\ F_x^C(\omega) \end{bmatrix} = \begin{bmatrix} \dfrac{e^{ik_L R_{S_2}} + e^{-ik_L R_{S_2}}}{2} & \dfrac{e^{ik_L R_{S_2}} - e^{-ik_L R_{S_2}}}{2k_L EAi} \\ -\dfrac{e^{ik_L R_{S_2}} - e^{-ik_L R_{S_2}}}{2(k_L EAi)^{-1}} & \dfrac{e^{ik_L R_{S_2}} + e^{-ik_L R_{S_2}}}{2} \end{bmatrix} \begin{bmatrix} x^B(\omega) \\ F_x^B(\omega) \end{bmatrix} \tag{5.8}$$

where i is an imaginary unit; ω is radial frequency; R_{S_2} is the length of the segment BC; $\left[x^C, F_x^C\right]^T$ and $\left[x^B, F_x^B\right]^T$ are vectors containing both the axial displacements x^C, x^B and axial forces F_x^C , F_x^B. c_L and k_L are longitudinal wave speed and longitudinal wave number as:

$$c_L = \sqrt{\frac{E}{\rho}}, \quad k_L = \frac{\omega}{c_L}. \tag{5.9}$$

Thus, given the knowledge of axial force F_x^B and displacement x^B at one end (point B in Fig. 5.2), the axial dynamics $\left[x^C, F_x^C\right]^T$ at the other end (or any other point between B and C) of the straight string segment can be obtained. The advantage of using TMM is that the dynamics is expressed as analytical matrix solutions, without the need to solve high-order differential equations. This format requires significantly lower computational resources.

Similarly, the torsional wave equation can be given as:

$$\frac{\partial^2 \alpha}{\partial x_l^2} = \frac{\rho}{G} \cdot \frac{\partial^2 \alpha}{\partial t^2} = \frac{1}{c_T^2} \cdot \frac{\partial^2 \alpha}{\partial t^2} \tag{5.10}$$

The torsional transfer matrix can be derived as [151]:

$$\begin{bmatrix} \alpha^C(\omega) \\ T_x^C(\omega) \end{bmatrix} = \begin{bmatrix} \dfrac{e^{ik_T R_{S_2}} + e^{-ik_T R_{S_2}}}{2} & \dfrac{e^{ik_T R_{S_2}} - e^{-ik_T R_{S_2}}}{2k_T GJi} \\ -\dfrac{e^{ik_T R_{S_2}} - e^{-ik_T R_{S_2}}}{2(k_T GJi)^{-1}} & \dfrac{e^{ik_T R_{S_2}} + e^{-ik_T R_{S_2}}}{2} \end{bmatrix} \begin{bmatrix} \alpha^B(\omega) \\ T_x^B(\omega) \end{bmatrix} \tag{5.11}$$

where G is shear modulus; α^C and α^B are the torsional displacements at point C and point B, respectively. T_x^C and T_x^B are the torsional torques at the cross-section of the corresponding location. c_T and k_T are torsional wave speed and torsional wave number as:

$$c_T = \sqrt{\frac{G}{\rho}}, \quad k_T = \frac{\omega}{c_T}. \tag{5.12}$$

To integrate the transfer matrix method organically into the finite element model, crucial procedures are needed to transform the frequency-domain relations into the time-domain relations with all the motion information on the left side and all the force information on the right side, as shown in the following steps as:

Step 1: Separate the Motion and Force Information in the Frequency Domain

The goal of this step is to separate the motion and force information in the transfer matrix relations in Eqs. (5.8, 5.11). By some matrix manipulations, the force/torque vectors at node B and node C (as shown in Fig. 5.2) can be rewritten in form of the motion vectors at node B and node C in the frequency domain as:

$$\begin{bmatrix} F_x^B(\omega) \\ F_x^C(\omega) \end{bmatrix} = \begin{bmatrix} \dfrac{k_L EAi}{\tanh(ik_L R_{S_2})} \cdot x^B(\omega) - \dfrac{k_L EAi \cdot S_{\text{hb}}}{\sinh(ik_L R_{S_2})} \cdot x^C(\omega) \\ \dfrac{k_L EAi}{\sinh(ik_L R_{S_2})} \cdot x^B(\omega) - \dfrac{k_L EAi}{\tanh(ik_L R_{S_2})} \cdot x^C(\omega) \end{bmatrix} \tag{5.13}$$

$$\begin{bmatrix} T_x^B(\omega) \\ T_x^C(\omega) \end{bmatrix} = \begin{bmatrix} \dfrac{k_T GJi}{\tanh(ik_T R_{S_2})} \cdot \alpha^B(\omega) - \dfrac{k_T GJi \cdot S_{\text{hb}}}{\sinh(ik_T R_{S_2})} \cdot \alpha^C(\omega) \\ \dfrac{k_T GJi}{\sinh(ik_T R_{S_2})} \cdot \alpha^B(\omega) - \dfrac{k_T GJi}{\tanh(ik_T R_{S_2})} \cdot \alpha^C(\omega) \end{bmatrix} \tag{5.14}$$

where $S_{\text{hb}} = \cosh^2(ik_L R_{S_2}) + \sinh^2(ik_L R_{S_2})$.

Step 2: Conduct Inverse Fourier Transform

Using inverse Fourier transform (IFT), Eqs. (5.13, 5.14) can then be converted into time

domain as:

$$\begin{cases} F_x^B(t) = F_x^B(t-2\tau_1) + Z_{c1}\dot{x}^B(t) + Z_{c1}\dot{x}^B(t-2\tau_1) - 2Z_{c1}\dot{x}^C(t-2\tau_1) \\ F_x^C(t) = F_x^C(t-2\tau_1) + 2Z_{c1}\dot{x}^B(t-\tau_1) - Z_{c1}\dot{x}^C(t) - Z_{c1}\dot{x}^C(t-2\tau_1) \end{cases} \tag{5.15}$$

$$\begin{cases} T_x^B(t) = T_x^B(t-2\tau_2) + Z_{c2}\dot{\alpha}^B(t) + Z_{c2}\dot{\alpha}^B(t-2\tau_2) - 2Z_{c2}\dot{\alpha}^C(t-2\tau_2) \\ T_x^C(t) = T_x^C(t-2\tau_2) + 2Z_{c2}\dot{\alpha}^B(t-\tau_2) - Z_{c2}\dot{\alpha}^C(t) - Z_{c2}\dot{\alpha}^C(t-2\tau_2) \end{cases} \tag{5.16}$$

where τ_1 and τ_2 are two constant delays for the axial and torsional waves:

$$\tau_1 = R_{S_2}\sqrt{\frac{\rho}{E}}, \;\; \tau_2 = R_{S_2}\sqrt{\frac{\rho}{G}}. \tag{5.17}$$

Z_{c1} and Z_{c2} are two constants for the axial and torsional waves and calculated as:

$$Z_{c1} = J\sqrt{\rho E}, \;\; Z_{c2} = A\sqrt{\rho G}. \tag{5.18}$$

Rearrange Eqs. (5.15, 5.16), we can obtain the time-domain representation of the boundary forces at both point B and C as:

$$\boldsymbol{F}_{\text{bound}}^B(t) = \begin{bmatrix} F_x^B(t) \\ T_x^B(t) \end{bmatrix}$$

$$= \begin{bmatrix} F_x^B(t-2\tau_1) + Z_{c1}\dot{x}^B(t) + Z_{c1}\dot{x}^B(t-2\tau_1) - 2Z_{c1}\dot{x}^C(t-2\tau_1) \\ T_x^B(t-2\tau_2) + Z_{c2}\dot{\alpha}^B(t) + Z_{c2}\dot{\alpha}^B(t-2\tau_2) - 2Z_{c2}\dot{\alpha}^C(t-2\tau_2) \end{bmatrix} \tag{5.19}$$

$$\boldsymbol{F}_{\text{bound}}^C(t) = \begin{bmatrix} F_x^C(t) \\ T_x^C(t) \end{bmatrix}$$

$$= \begin{bmatrix} F_x^C(t-2\tau_1) + 2Z_{c1}\dot{x}^B(t-\tau_1) - Z_{c1}\dot{x}^C(t) - Z_{c1}\dot{x}^C(t-2\tau_1) \\ T_x^C(t-2\tau_2) + 2Z_{c2}\dot{\alpha}^B(t-\tau_2) - Z_{c2}\dot{\alpha}^C(t) - Z_{c2}\dot{\alpha}^C(t-2\tau_2) \end{bmatrix} \tag{5.20}$$

Step 3: Integrate Transfer Matrix into Finite Element Model

Thus, the overall hybrid modeling dynamics equations including the FEM portion (Eq. (5.6)) and the TMM portion (Eqs. (5.19, 5.20)) can be written as:

$$\boldsymbol{M}^g\ddot{\boldsymbol{U}}^g(t) + \boldsymbol{D}^g\dot{\boldsymbol{U}}^g(t) + \boldsymbol{K}^g\boldsymbol{U}^g(t) = \boldsymbol{F}^g_{\text{ext}}(t) + \boldsymbol{F}^B_{\text{bound}}(t) + \boldsymbol{F}^C_{\text{bound}}(t) \tag{5.21}$$

5.2.3 External Force Modeling for Directional Drilling System

The external forces $\boldsymbol{F}_{\text{ext}}$ include surface control inputs (hook load and top drive torque), drill string/well-bore contact force and torque, bit/rock interaction force and torque, and the gravitational force.

5.2.3.1 Drill String/Well-bore Contact Model

Due to the inevitable contact of the curved drill string with the well-bore, the contact forces between the drill string and well-bore should be modeled. We assume that the critical contact forces are those in the axial and torsional direction since the axial and torsional dynamics are dominant in the drill string motion. Thus, only axial and torsional contact forces/torques are considered and the lateral ones are mainly to maintain the string in the well-bore. Figure 5.3 shows the top view of the cross-sectional area $E-E$ (left), and the cross-sectional area view $F-F$ (right) of the top view $E-E$, where the axial force $F_{S_1}\odot$ acts on the contact area H and points outside the $E-E$ plane (see $F-F$); and torsional torque T_{S_1} is in the opposite direction of the drill string rotation. For drill string/well-bore contact location i, the axial force F_{S_i} and torsional torque T_{S_i} are given as:

$$\begin{cases} F_{S_i}(t) = \mu_w F^n_{S_i}(t)\cos(\phi_i(t)), \\ F^t_{S_i}(t) = \mu_w F^n_{S_i}(t)\sin(\phi_i(t)), \\ F^n_{S_i}(t) = -k_w\Delta(t)\mathbb{H}(\Delta(t)), \\ T_{S_i}(t) = R_w F^t_{S_i}(t). \end{cases} \tag{5.22}$$

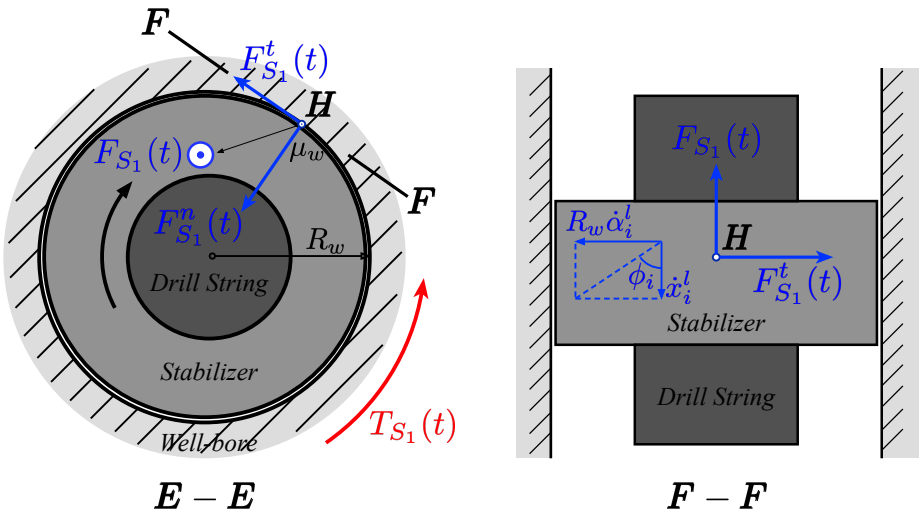

Figure 5.3 Illustration of the well-bore contact model

where μ_w is the coefficient of friction between the well-bore and stabilizers; R_w is the radius of the stabilizer; $F^n_{S_i}$ and $F^t_{S_i}$ are normal and tangential components of the lateral force acting on the stabilizers, and are modeled using the Hertz contact theorem (see [135] [47] for details); k_w is the stiffness coefficient; $\mathbb{H}$ represents the Heaviside function; Δ is the elastic deformation; ϕ_i is the angle characterized by the relative moving direction of the stabilizer with respect to the well-bore (as shown in Fig. 5.3), and their cosine and sine functions are given as:

$$\begin{cases} \cos(\phi_i(t)) = \dfrac{\dot{x}^l_i(t)}{\sqrt{(\dot{x}^l_i(t))^2 + (R_w\dot{\alpha}^l_i(t))^2}}, \\ \sin(\phi_i(t)) = \dfrac{R_w\dot{\alpha}^l_i(t)}{\sqrt{(\dot{x}^l_i(t))^2 + (R_w\dot{\alpha}^l_i(t))^2}}. \end{cases} \tag{5.23}$$

5.2.3.2 Bit/Rock Interaction Model

A polycrystalline diamond compact bit/rock interaction model developed by Detournay et al. [8] is used in this chapter as:

$$\begin{cases} W_{\mathrm{B}}(t) = W_{\mathrm{B}_f}(t) + W_{\mathrm{B}_c}(t), \\ T_{\mathrm{B}}(t) = T_{\mathrm{B}_f}(t) + T_{\mathrm{B}_c}(t) \end{cases} \tag{5.24}$$

where W_{B} and T_{B} stand for the weight-on-bit and torque-on-bit, and they can be decomposed into the frictional component W_{B_f}, T_{B_f} and the cutting component W_{B_c}, T_{B_c}, respectively:

$$\begin{cases} W_{\mathrm{B}_f}(t) = \sigma l_w R_b d(t)/d^*, \\ W_{\mathrm{B}_c}(t) = \zeta \epsilon R_b d(t) \mathbb{H}(d(t)) \\ T_{\mathrm{B}_f}(t) = 0.5 \mu \gamma R_b W_{\mathrm{B}_f}(t), \\ T_{\mathrm{B}_c}(t) = 0.5 \epsilon R_b^2 d(t) \mathbb{H}(d(t)). \end{cases} \tag{5.25}$$

where σ is the maximum contact pressure at the wear-flat interface; l_w is the equivalent wear-flat length; R_b is the bit radius; ζ represents the bit geometry constant; ϵ is the intrinsic specific energy; μ represents the coefficient of friction at the wear-flat rock interface; γ is the geometric parameter of the bit; d^* is the critical depth of cut; d is the axial depth of cut, and can be obtained as:

$$\begin{cases} d(t) = n_0 \left[x^l_{N^*}(t) - x^l_{N^*}(t - \tau_0) \right] \\ \alpha^l_{N^*}(t) - \alpha^l_{N^*}(t - \tau_0) = 2\pi / n_0 \end{cases} \tag{5.26}$$

where N^* denotes the number of nodes for U^g ($N^* = N_1 + N_2$); $x^l_{N^*}$ and $\alpha^l_{N^*}$ are bit axial and torsional displacement; τ_0 is the time delay used to model the motion gap between two neighboring blades on the bit [111].

5.3 Numerical Simulation of the Hybrid Drilling Dynamics Model

In this section, we first compare the beam structure dynamics using both the hybrid modeling approach and the FEM to validate the efficacy of the proposed hybrid modeling approach. Then we use this proposed hybrid modeling approach to simulate the down-hole drilling vibrational behavior (hybrid beam structure model with the bit-rock interaction model). After that, a series of hybrid models are tested with different degrees of freedom to show the model consistency in generating the down-hole vibrational behavior. In the end, the computational expenses using the hybrid modeling approach and the FEM are discussed.

5.3.1 Comparison of Hybrid Method with FEM Simulation Results

To validate the proposed hybrid modeling approach, we will conduct numerical simulations using FEM for the entire drill string (no matter curved or straight portion) with dense FEM meshing and compare that with the simulation from the hybrid modeling approach. Since the finite element method is a well-established modeling approach and validated to be high-fidelity in many real-world applications, the accurate matching of the hybrid model simulation result with that from FEM can prove the effectiveness of the proposed hybrid modeling method.

The drill string of length 2000 m is discretized into 180 finite elements for FEM modeling. Figure 5.4 shows the comparison of axial forces calculated at points B and C (Fig. 5.2) using FEM with those obtained from the hybrid method.

Figure 5.5 shows the torsional torques at points B and C using FEM and hybrid method, respectively. The close match between the red (FEM) and the blue curve (hybrid method) demonstrates the modeling accuracy of the proposed approach. The comparison for torsional torque modeling in Fig. 5.4 indicates modeling effectiveness as well. With the numerically calculated boundary force and torque (at points B and C), the drill string motion dynamics at any arbitrary point can be simulated using the hybrid approach as shown in Fig. 5.6.

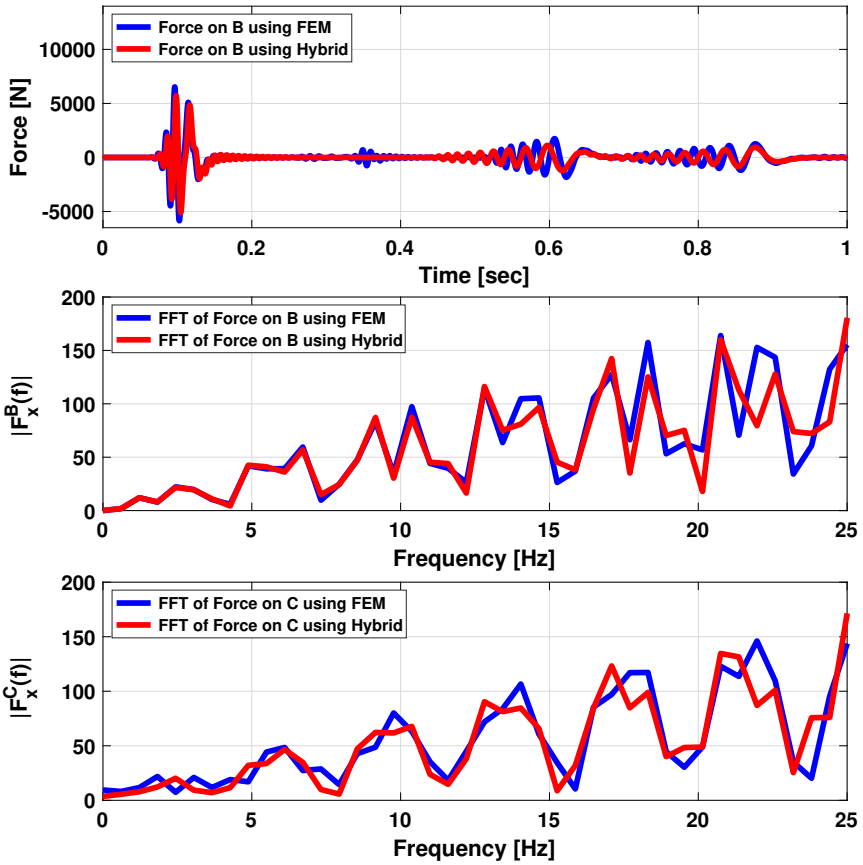

Figure 5.4 Force comparison at point B and point C

5.3.2 Down-Hole Vibration Modeling Using Hybrid Method

In this subsection, a bit-rock interaction model is added to the drill string dynamics modeled using the proposed hybrid method to simulate the down-hole vibrational behavior. We assume the segment CD is the in-plane circular arc characterized by arc radius R_C and the arc angle θ_{CD}. All the parameters used in the simulation are listed in Table 5.1.

The driving torque on the ground is provided by an electric motor through a transmission gearbox. Using a proportional-integral (PI) controller, the top drive's rotational speed is set at 10 rad/s. Meanwhile, a constant hook load is maintained on the surface. The simulation result is shown in Fig. 5.7.

The proposed hybrid model can retrieve the drilling responses like instantaneous axial

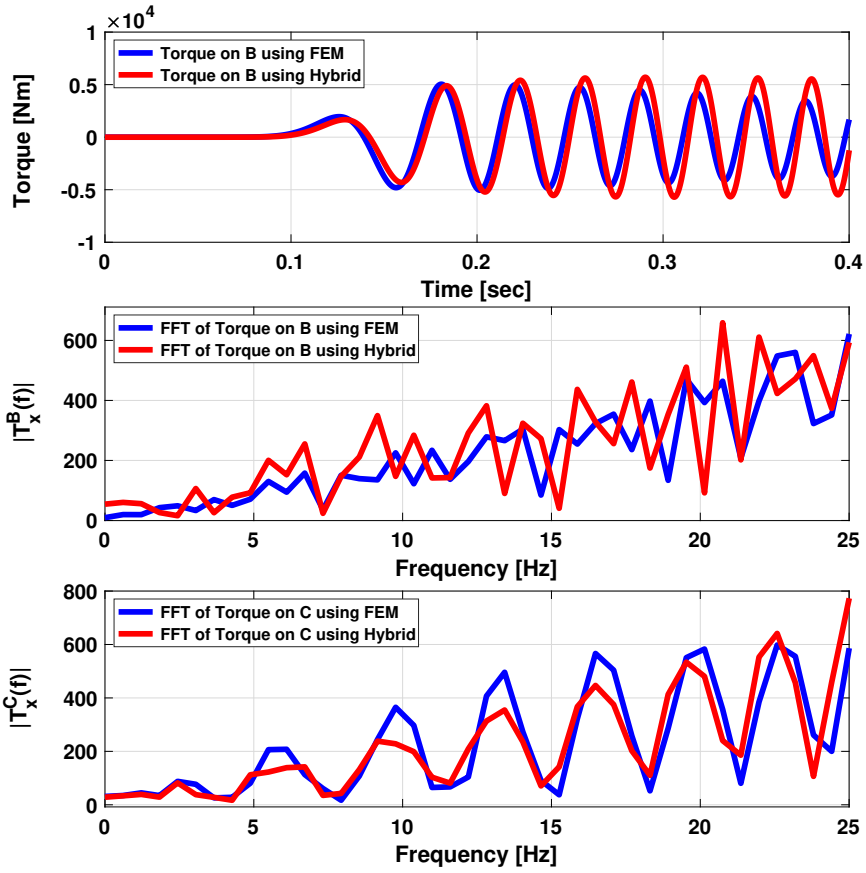

Figure 5.5 Torque comparison at point B and point C

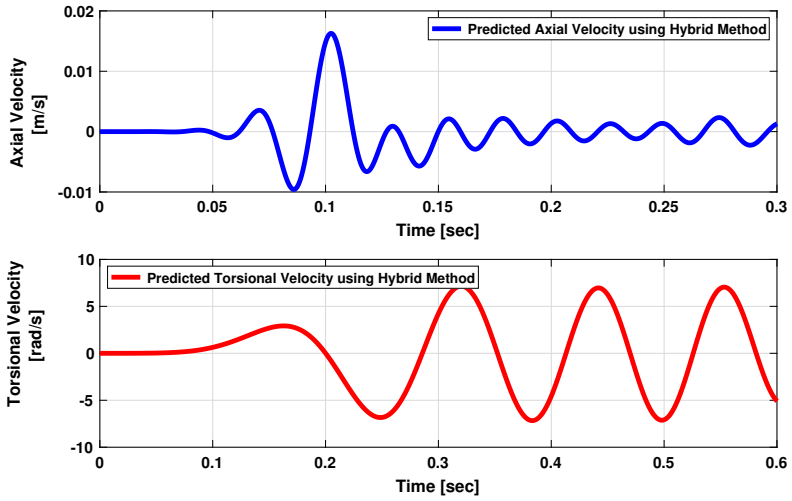

Figure 5.6 Predicted velocity profiles at arbitrary point

Table 5.1 Simulation parameters in computationally efficient directional drilling dynamics model

Symbol	Value [Unit]	Description
E	210 [GPa]	Young's modulus
G	80.8 [GPa]	Shear modulus
ρ	7850 [kg/m^3]	Drill string density
D_i	0.06 [m]	Drill string inner diameter
D_o	0.12 [m]	Drill string outer diameter
A	0.0085 [m^2]	Cross-section area
J	1.72×10^{-5} [m^4]	Torsional constant
α_0	0.05	Raleigh damping
β_0	0.03	Raleigh damping
R_{S_1}	2000 [m]	Length of segment AB
R_{S_2}	1000 [m]	Length of segment BC
R_C	4000 [m]	Radius of segment CD
θ_{CD}	30 [°]	Angle of segment CD
n_0	5	Bit number of blades
k_w	1×10^8 [N/m]	well-bore stiffness
μ_w	0.5	Friction coefficient
R_w	0.24 [m]	Radius of the well-bore
R_b	0.22 [m]	Radius of the bit
l_w	3.6×10^{-3} [m]	Total wear-flat length
d^*	1.2×10^{-3} [m]	Depth of cut threshold
ϵ	45 [MPa]	Intrinsic specific energy
σ	45 [MPa]	Contact strength
ζ	0.64	Cutter face inclination
$\gamma\mu$	0.7	-

velocity and torsional velocity at the drill bit, which can be used in a two phases bit-rock interaction model to calculate W_B and T_B when the bit starts to penetrate the rock formation. For this scenario, the simulation result shows clear axial velocity and torsional velocity vibration at the drill bit.

Figure 5.7 shows the drilling system dynamics response when the torsional velocity of the top drive equals to 10 rad/s. Within the first 0.5 sec, the bit starts a cyclical oscillating cycle in both torsional and axial directions. This behavior is typically referred to as "*stick-slip*" behavior, where the bit can get stuck for a short period of time due to large resistance and then immediately ramp up in speed as a sudden release of elastic energy in the drill pipes.

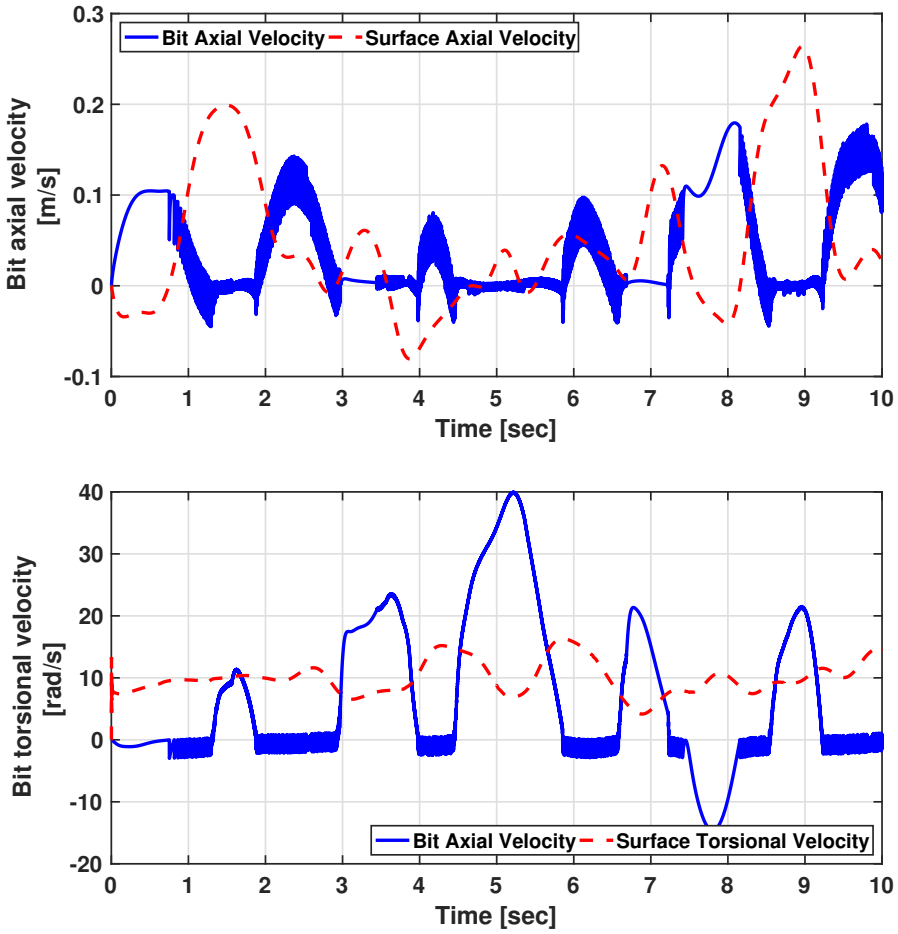

Figure 5.7 Bit-bounce and stick-slip vibration simulation using hybrid model (drill bit velocity profile when top drive torsional speed is 10 rad/s)

5.3.3 Model Validation Using Hybrid Models with Different System Orders

Figure 5.8 shows the comparison of the hybrid models with different system orders (from 24 degree of freedom (DOF) to 68 degree of freedom). The result shows that both the bit axial and torsional velocities have the same general trends and the results of the $24, 32, 40, 48, 68$ DOF models are very consistent. It also shows that more transient details can be observed in the higher-order hybrid drilling dynamics model (see 68 DOF model labeled in green solid line in Fig. 5.8).

This demonstrates that the 68 DOF higher-order hybrid drilling dynamics model can be used to accurately describe the drilling vibrational behaviors for control validation.

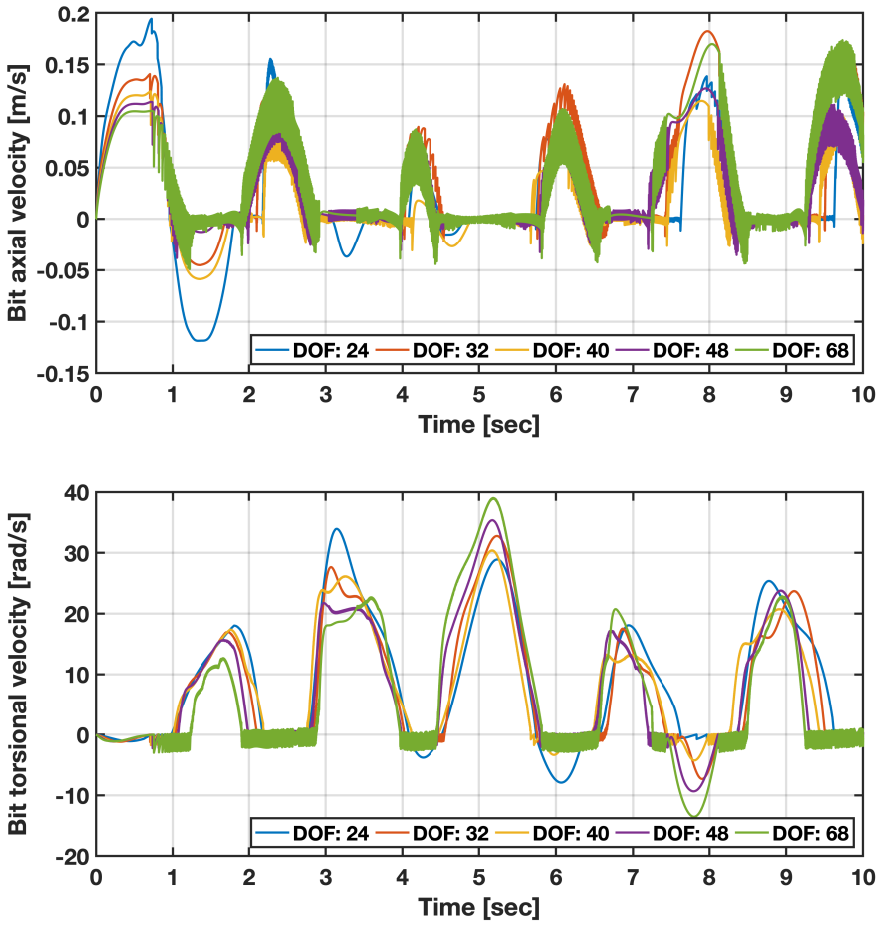

Figure 5.8 Comparison of the hybrid models with different system order

5.3.4 Computational Cost

To evaluate the computational efficiency of the hybrid method, we tested several cases where the curved portion is kept the same but the length of the straight portion gradually increases in the simulation (from 500 meters to 10000 meters shown in the horizontal axis of Fig. 5.9). Meanwhile, we also kept the length of each element used in FEM constant in all the cases. As shown in Fig. 5.9, when the length of the straight portion increases from

500 m to 10000 m, the computational time (simulating a 30 sec drilling event) for hybrid method remained less than 20 sec, but the time needed for FEM computation (if model the entire drill string with FEM) increases drastically to 800 sec. This increase is due to the need for a large number of FEM meshes for the long straight segment. Besides, the modeling accuracy of the hybrid method is well maintained and is close to that using the complete finite element modeling, similar to the model matching results shown in Fig. 5.4 and Fig. 5.5.

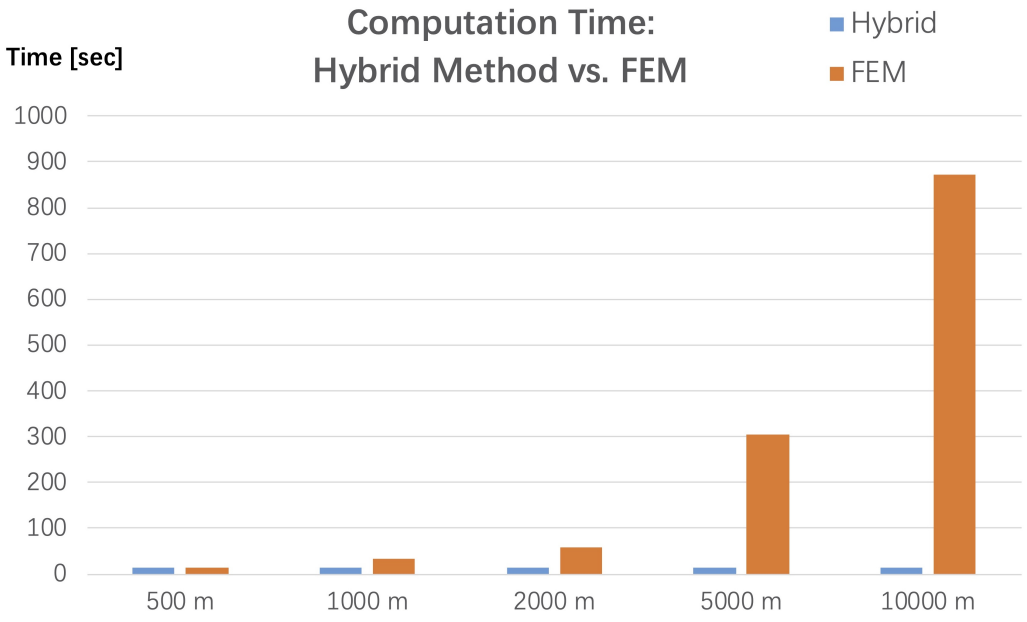

Figure 5.9 Comparison of computation time of FEM and hybrid method (horizontal axis is the length of straight segment; the length of each element used in FEM is kept constant.)

In addition, the computational costs using the FEM model and the hybrid model with different degrees of freedom and sampling time are listed in Table 5.2. A 10 sec simulation and a 20 sec simulation are conducted using a laptop (CPU: i7-9750H, RAM: 16GB) to study the computational expenses saving. While the FEM model requires 432 number of states, the equivalent hybrid model only requires 108 number of states to solve the same drilling

problem. This will tremendously reduce the computational load, and the results show its potential to be used in real-time control validation in Chapter 6.

5.4 Summary

This chapter introduces a hybrid modeling approach integrating the finite element method and the transfer matrix method to model the dynamics of the directional down-hole drilling system. It inherits the merits of both FEM and TMM, which maintains high-fidelity for the curved/non-uniform portion of the drill string and also requires significantly low computational resources. The hybrid approach is enabled by the uniqueness of the drill string geometric structure, which is a large scale in axial dimension but has very a high axial-to-radial ratio. This makes the drill string a single-dimensional element so the integration method proposed at the joints of FEM and TMM is feasible. The comparison with the finite element method validates the proposed hybrid approach in dynamics modeling, and the down-hole drilling vibration simulation also shows its effectiveness in drilling dynamics analysis and real-time control validation.

Table 5.2 Computational expenses comparison between finite element model and hybrid model with different degrees of freedom and sampling time

Model	Time Interval	State No.	Simulation (10 sec)	Simulation (20 sec)
FEM model	10^{-4} sec	432	118.34 sec	240.95 sec
Hybrid model	10^{-4} sec	108	36.89 sec	74.12 sec
Hybrid model	10^{-4} sec	24	8.52 sec	16.74 sec
FEM model	10^{-3} sec	432	12.31 sec	23.86 sec
Hybrid model	10^{-3} sec	108	4.33 sec	10.06 sec
Hybrid model	10^{-3} sec	24	0.74 sec	1.59 sec

6. VALIDATION OF DIRECTIONAL DRILLING CONTROL USING SOFTWARE-IN-THE-LOOP

This chapter presents a software-in-the-loop real-time simulation environment to validate the DHP based controller designed in Chapter 4 for directional down-hole drilling systems. In this SIL platform, the directional drilling dynamics is described by a 68 DOF hybrid model (Chapter 5), and the DHP based controller designed in Chapter 4 is implemented in real-time to effectively mitigate harmful vibrations, accurately track the desired trajectories, and significantly enhance drilling efficiency. Furthermore, this SIL platform can be conveniently transformed into a hardware-in-the-loop real-time platform for physical drill-rig testing, which can facilitate rapid prototyping to validate the effectiveness of the proposed DHP based control algorithm in real-time.

6.1 Introduction

The traditional drilling rig mainly depends on the human drillers to monitor the down-hole conditions and suffers from many critical issues such as the excessive vibrations, non-optimal production rate, high non-production time (NPT), etc. Therefore, the drilling performance is highly based on the operator's experience, skills, and provisional judgments. To resolve these issues, automated drilling systems are developed to optimize the drilling parameters using different control and optimization algorithms. Compared with traditional drilling operations, the automated drilling system can optimize the drilling parameters in real-time according to the sensor data to obtain the "*optimal*" drilling performance [152].

However, it is typically impractical to directly implement and test on the real drill-rig due to the high costs of the drill-rig construction. Additionally, it can be dangerous if the proposed controller is not well-tested. Therefore, instead of implementing the controller directly on the real drill-rig [13], a lab-scale testing platform is needed for control validation as an intermediate step.

At an early or middle stage of the control design and validation, the "*X-in-the-Loop*" is a set of common techniques to test the control algorithms in mathematical/semi-mathematical/physical models [153], which includes "*Model-in-the-Loop* (MIL)," "*Software-in-the-Loop*," "*Hardware-in-the-Loop*," etc (see Fig. 6.1). One of the XIL, the software-in-the-loop, has been commonly used in the field of automotive, aerospace, chemical reaction plants, etc. It allows the tester to integrate different software components in a real-time simulated environment and test the proposed control and optimization algorithms in a faster and safer way. Particularly for the large-scale applications such as the down-hole drilling system, the advantage of using the SIL is obvious: the constructions of the full-scale drill-rig setup can be both very costly and challenging. In addition, applying the SIL can shorten the prototyping time of the control algorithm implementation, and the modification of the system parameters is easier and safer.

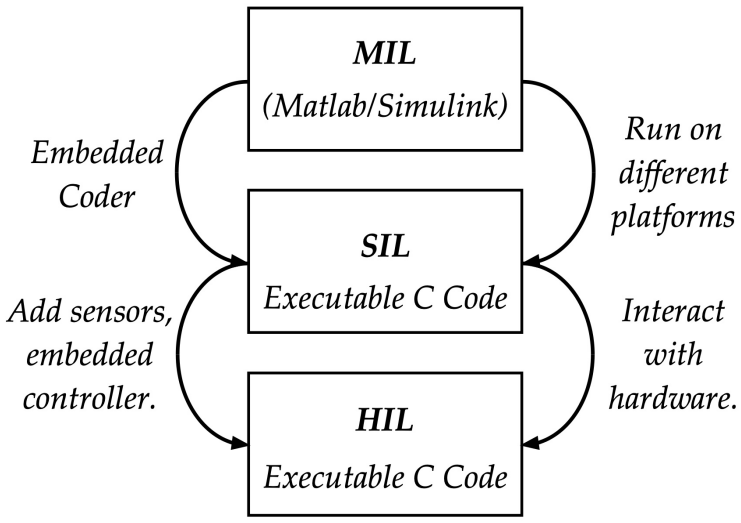

Figure 6.1 Rapid prototyping tools for control: MIL/SIL/HIL

This chapter presents a software-in-the-loop testing framework of the down-hole drilling dynamics system for the real-time implementation and validation using the DHP based controller designed in Chapter 4. Two main parts of the SIL are presented: a drilling dynamics model simulator and a dual heuristic programming controller. The SIL results

show that the harmful "*stick-slip*" and "*bit-bounce*" behaviors can be reconstructed in the open-loop simulation, and obvious mitigation of these vibrations and a more steady drilling performance can be observed after implementing the dual heuristic programming closed-loop controller in this SIL real-time environment. This proves the developed control algorithm is effective and efficient for practical use.

The rest of this chapter is organized as follows. Section 6.2 introduces the overview of the software-in-the-loop architecture including the drilling dynamics model and the DHP based controller. In section 6.3, a series of numerical simulations are conducted to validate the effectiveness of the proposed DHP based control algorithm. In the end, the summary of this chapter is presented.

6.2 Software-in-the-Loop Architecture for Control Validation

In this section, the description of the software-in-the-loop architecture is presented first. Then we test the model-in-loop in the MATLAB/SIMULINK environment and transform it into the LABVIEW software-in-the-loop real-time environment.

Figure 6.2 shows the schematic diagram of the DHP based control design and validation for the directional drilling process. A lower-order finite element drilling dynamics model is used to train the neural network weight matrix and derive the DHP based controller, then this designed DHP based controller is validated using a higher-order hybrid drilling dynamics model.

6.2.1 Model-in-the-Loop

The model-in-the-loop is constructed and tested first in a MATLAB/SIMULINK environment. As illustrated in Fig. 6.3, the block diagram of the directional drilling control consists of three basic elements: the user-defined reference, the hybrid directional drilling dynamics model, and the DHP based controller.

Note that the reference can be assigned to any user-defined function of time. The predetermined neural network matrix is loaded to formulate the DHP based control inputs (u_1 and

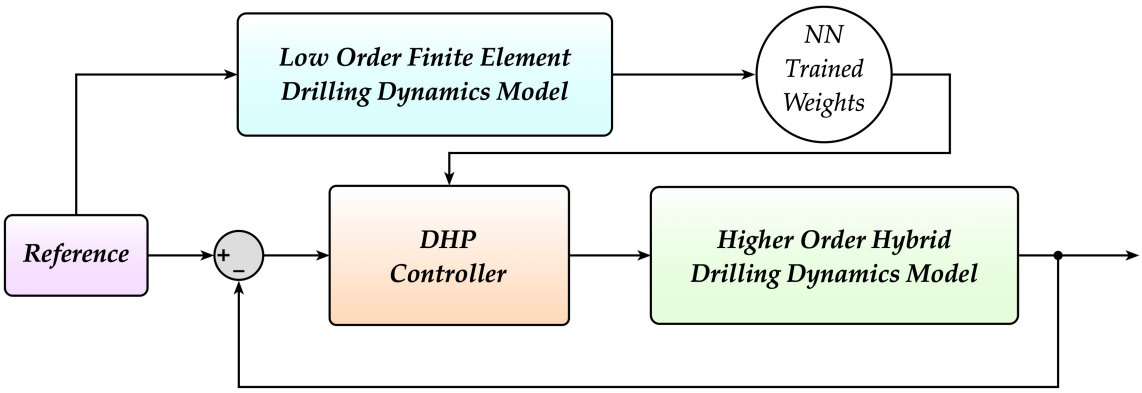

Figure 6.2 Schematic diagram of the control system design and validation for directional drilling

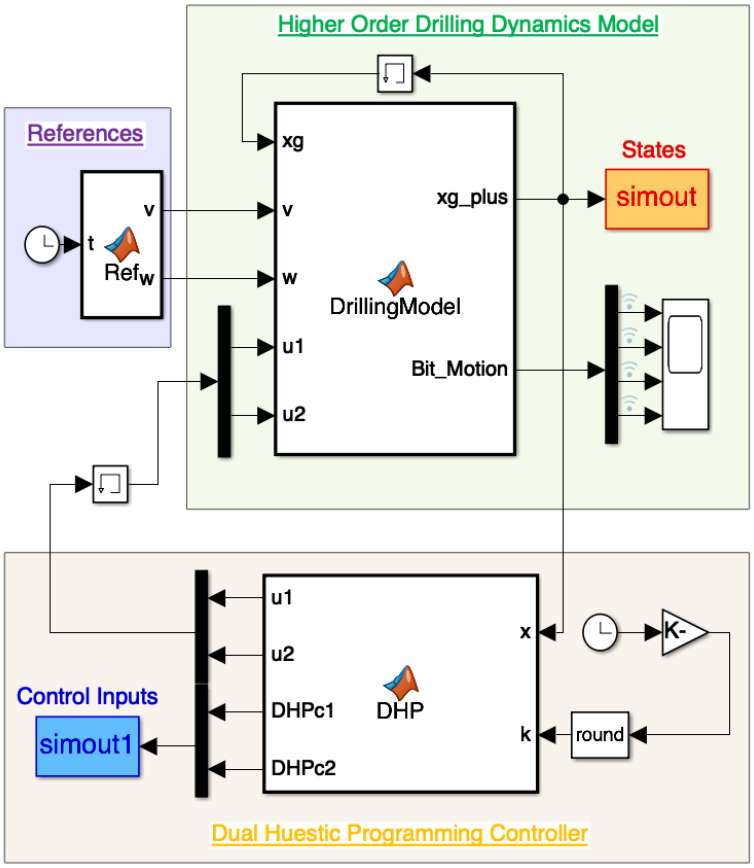

Figure 6.3 SIMULINK block diagram of the directional drilling control

u_2) at step k using the state vector information from "*DrillingModel*" (MATLAB Function). These control inputs will be fed to the higher-order drilling dynamics model to control both

the axial and torsional motions of the directional drilling dynamics in real-time. A fixed time interval dt is set as 10^{-3} sec, and the numerical solver can be selected as the Euler method (ODE1).

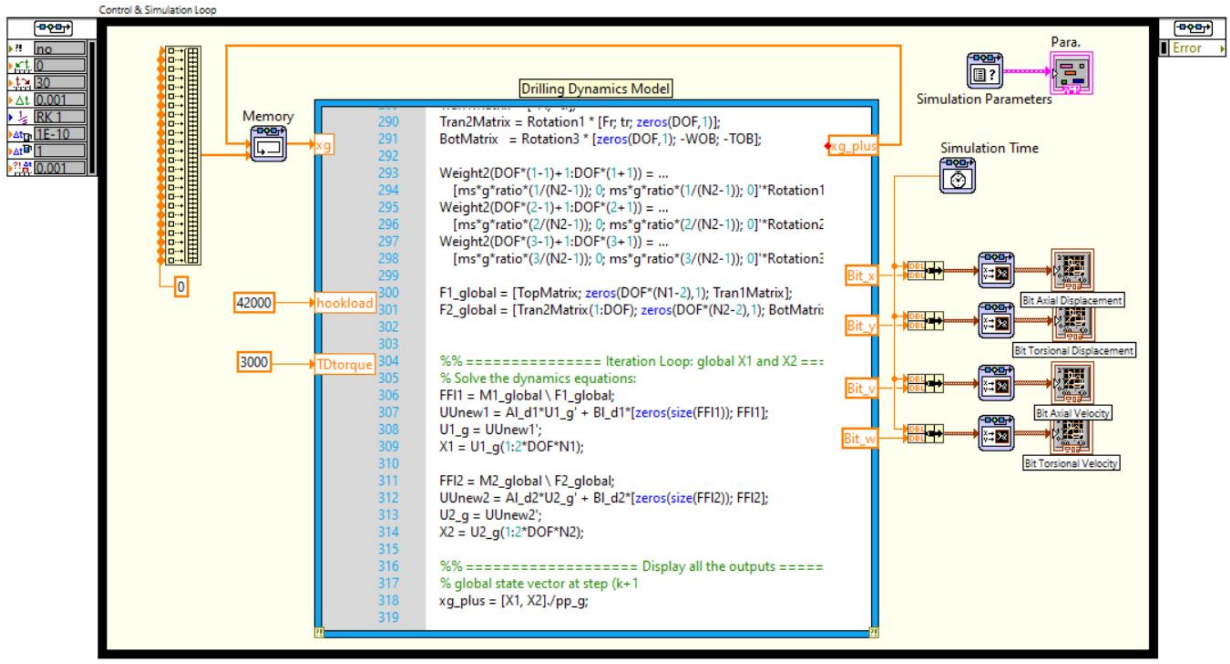

Figure 6.4 Directional drilling dynamics simulator

6.2.2 Software-in-the-Loop Implementation

After the model and control algorithm are examined in the MIL, the SIMULINK model above can be transformed and implemented into the National Instruments LABVIEW environment using the "*MathScript Node*." As shown in Fig 6.4, a hybrid directional drilling dynamics model is used with a zero initial condition. Figure 6.4 shows the drilling scenario with a constant hook load (not including the gravity force) and a constant top drive torque provided. The simulation result shows that the obvious "*stick-slip*" and "*bit-bounce*" behaviors can be reconstructed in the open-loop solution, as shown in Fig. 6.5.

In order to implement the DHP based controller into the LABVIEW environment, the

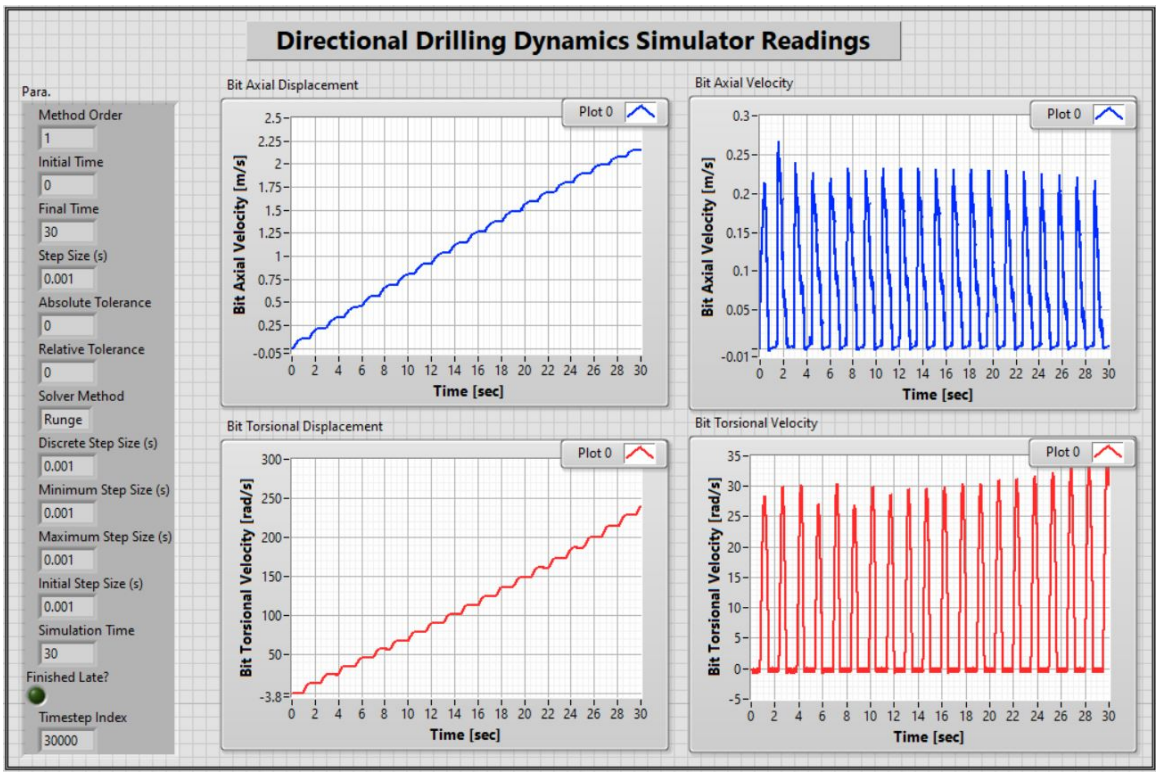

Figure 6.5 Stick-slip and bit-bounce behaviors using the directional drilling dynamics simulator

following procedure is used to reduce the computational burden during the implementation. While a predetermined 3-D weight matrix W is needed to formulate the DHP based controller, there is no direct toolbox in LABVIEW to import such a 3-D array. On the other hand, to load a 3-D array can be also computationally intensive. To solve this problem, we transform this 3-D matrix W into a 2-D matrix, and load the sub-matrix of this reshaped 2-D matrix to obtain the DHP based controller at step k. This can be illustrated in Fig. 6.6, where the dimension of W is $25 \times 24 \times 30000$ and W is transformed into a 750000×24 2-D matrix.

Figure 6.7 displays the drilling dynamics simulator with the DHP based controller in the LABVIEW environment. Figure 6.8 shows the closed-loop solution when the DHP based controller is on. It is observed that the open-loop vibrational behaviors "*stick-slip*" and "*bit-bounce*" disappear after around $5 \sim 10$ sec, and the bit axial and torsional velocities reach

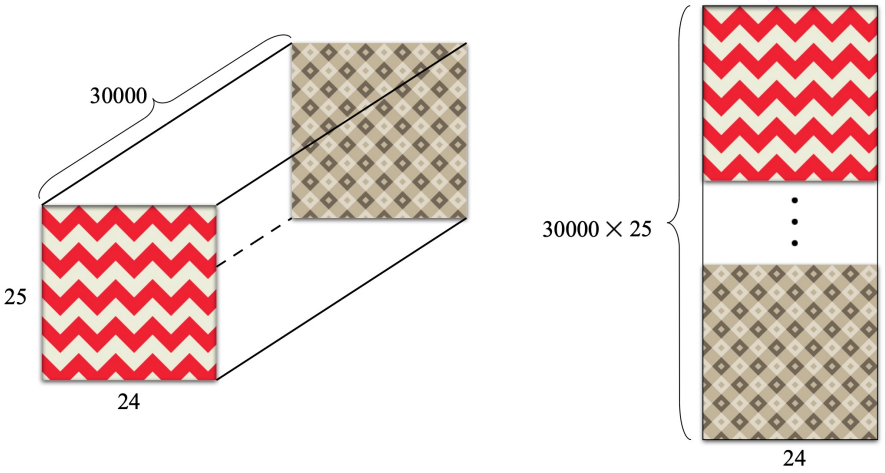

Figure 6.6 Transformation of the neural network weight matrix from 3D array to 2D array

the desired reference values.

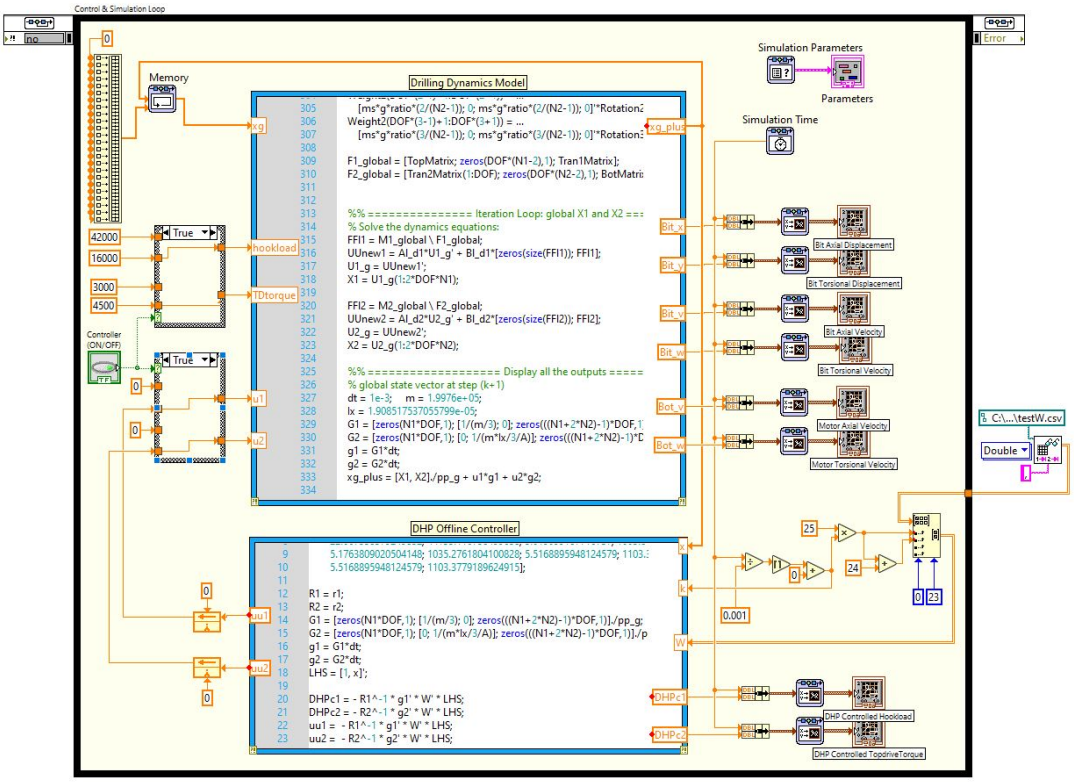

Figure 6.7 DHP controlled directional drilling dynamics simulator

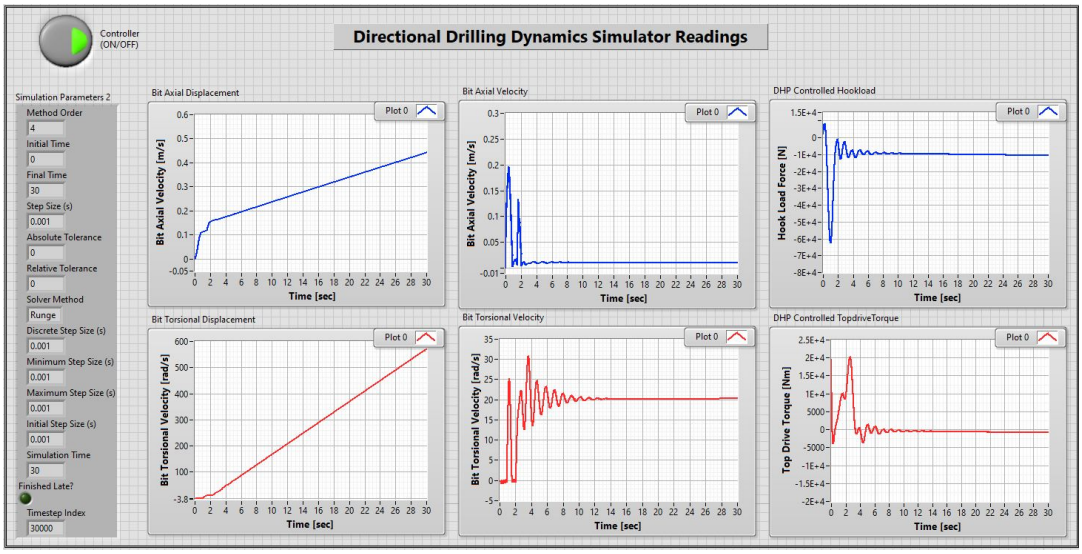

Figure 6.8 DHP controlled drill bit motion profile using the directional drilling dynamics simulator

6.2.3 Potential Use for Hardware-in-the-Loop

After completing the SIL real-time simulation environment in LABVIEW, it is straightforward to transform the current software-in-the-loop into a potential hardware-in-the-loop to further test the effectiveness of the controller. Figure 6.9 illustrates the transformation process of the SIL into the HIL and lists some of the changes:

1. The HIL will replace the drill bit mathematical model with a physical laboratory-scale drill-rig.

2. In the SIL, the bit is assumed at the last node (point D) in the drill string model; In contrast, the velocity (v_{M} and ω_{M}) of the last node in the HIL drill string model becomes the input to the laboratory-scale drill-rig, and the output of the drill-rig is the bit velocity (v_{B} and ω_{B}).

3. Instead of calculating from the mathematical model, the bit motions are measured using the sensors and transmitted to the embedded controller (NI CompactRIO) for control design.

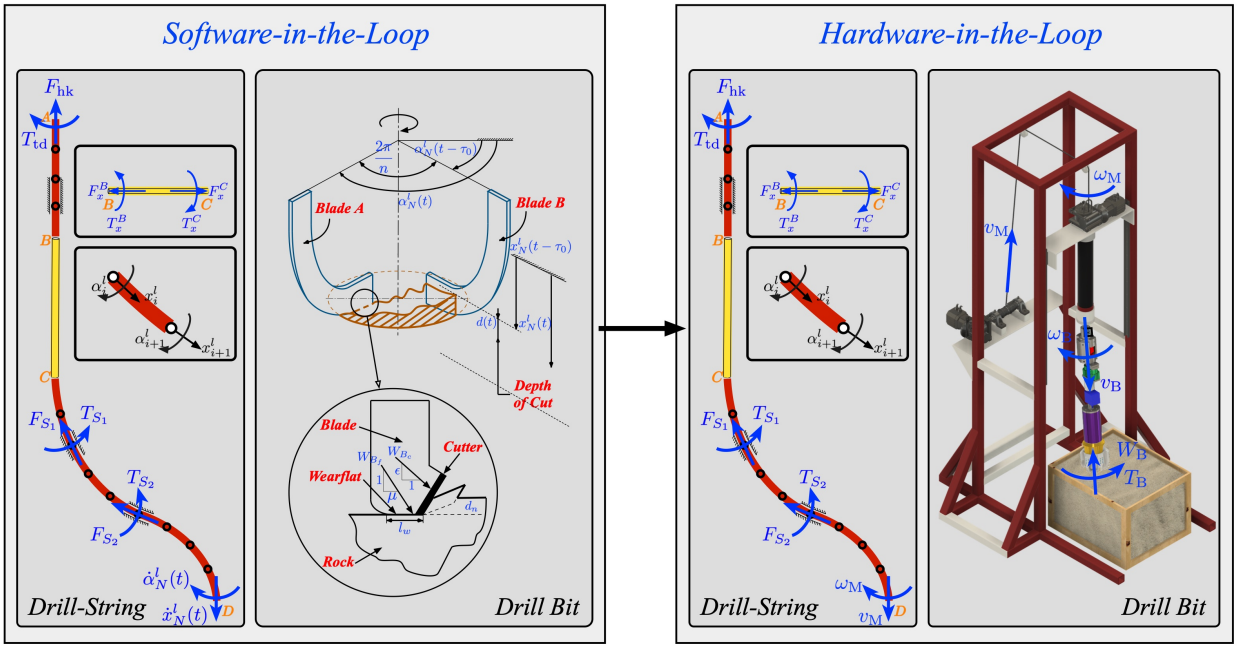

Figure 6.9 Transform of the SIL into the HIL

6.3 Control Validation Results Using a Higher-Order Hybrid Directional Drilling Dynamics Model

A higher-order hybrid directional drilling dynamics model is used to validate the designed DHP based controller in this section. Since the DHP based controller uses all the state vector information in the lower-order model to formulate the controller, these nodes need to be preserved in the higher-order model and the multiplication of the weight matrix W and these nodes' information will formulate the DHP based controller. Figure 6.10 illustrates how to add additional nodes into the original lower-order model.

In the lower-order hybrid model of directional drilling, suppose the finite element segment AB has $N_1 = 2$ nodes, finite element segment CD have $N_2 = 4$ nodes. Also assume N_{a1} ($N_{a1} = 2$) and N_{a2} ($N_{a1} = 3$) are the number of the additional nodes added to section AB and section CD (see green triangle labeled in Fig. 6.10), then the total number of nodes in the higher-order hybrid model of drilling will be: $(N_{a1}+1)(N_1-1)+(N_{a2}+1)(N_2-1)+2 = 17$. Considering that each FEM node contains 4 states (axial and torsional position and velocity),

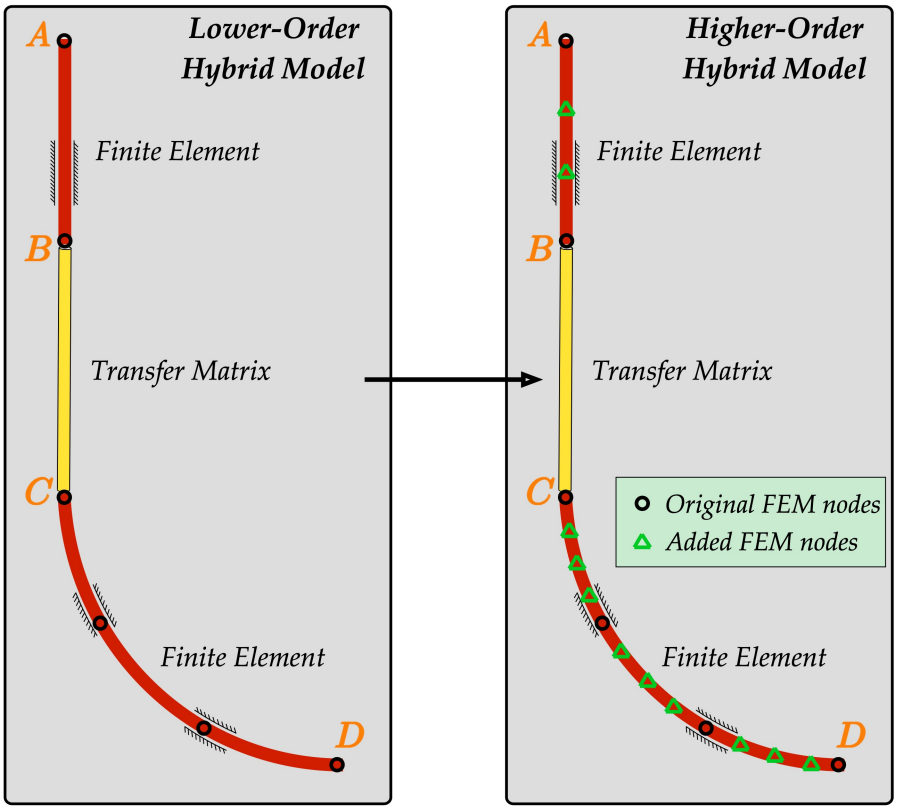

Figure 6.10 Illustration of adding additional FEM nodes to the lower-order directional drilling dynamics model

the higher-order model of drilling has $4 \times 17 = 68$ DOF. In this section, this 68 degree of freedom hybrid directional drilling model is used to validate the proposed DHP based controller.

Three different trajectories are given to test the vibration mitigation and trajectory tracking performance. Figure 6.11 shows that the bit axial and torsional velocities can be quickly stabilized in the 68 DOF higher-order hybrid model of drilling. This validates that the proposed DHP based controller (based on a 24 DOF lower-order FEM model) can regulate the bit velocities, and is effective to avoid the "*stick-slip*" and "*bit-bounce*" behaviors.

Figure 6.12 and Figure 6.13 validate that the designed DHP based controller can effectively track the desired trajectories.

6.4 Summary

This chapter presents a software-in-the-loop real-time simulation environment of the directional drilling system. A 68 DOF higher-order hybrid model of directional drilling and the DHP based controller designed in Chapter 4 is implemented in the LABVIEW real-time environment. The real-time simulation results demonstrate that the designed DHP based controller can effectively mitigate harmful vibrations, accurately track the desired trajectories, and greatly improve drilling efficiency.

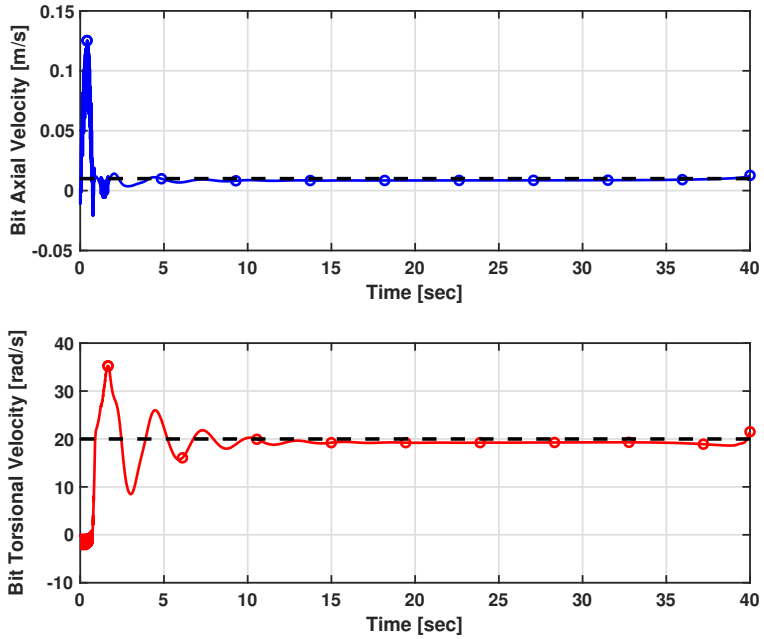

Figure 6.11 DHP controlled bit step response using a 68 DOF hybrid directional drilling model

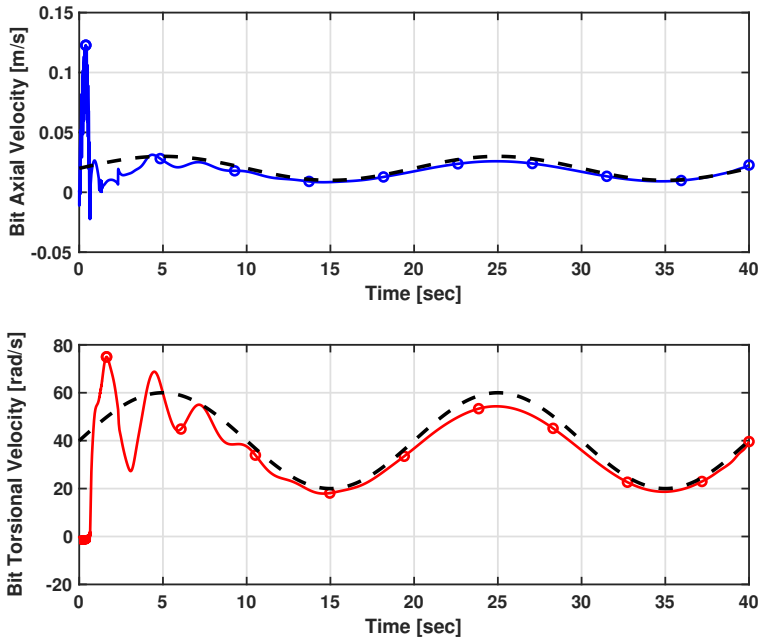

Figure 6.12 DHP controlled bit sinusoidal response using a 68 DOF hybrid directional drilling model

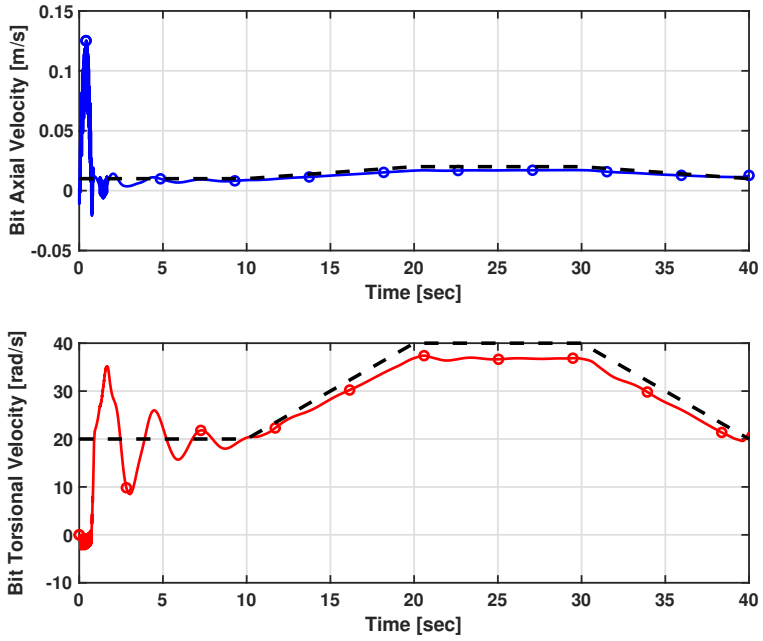

Figure 6.13 DHP controlled bit ramp response using a 68 DOF hybrid directional drilling model

7. SUMMARY

7.1 Summary

This dissertation investigates the modeling, optimization, and control of the down-hole drilling system. Various efforts have been made on control and optimization of both the vertical drilling system and the directional drilling system. For vertical drilling, we proposed two different control and optimization approaches based on a lumped parameter model and a distributed parameter model. For directional drilling, a DHP based control is designed based on a finite element model and further validated using a higher-order hybrid model combining finite element and transfer matrix in a software-in-the-loop real-time simulation testbed.

7.1.1 Vertical Drilling Optimization and Control

An open-loop DP optimization approach is developed in Chapter 2 based on a lumped parameter model. To lower the computational intensity, the proposed DP algorithm is customized for the drilling dynamics model, which makes it computationally efficient and can be used as a guide for drilling control or in a driller-assist system. However, the proposed customized DP approach has some drawbacks:

- The oversimplified model used in the customized DP is inaccurate to describe the slender characteristics of the drill string.
- There is no feedback information in the customized DP approach, which can be inaccurate and ineffective to the output changes. Thus a closed-loop control is needed to accommodate the external disturbances in the output.

Therefore, a closed-loop EID control is designed based on an axial & torsional coupled distributed parameter model in Chapter 3. The proposed EID based controller has robustness, accurate trajectory tracking performance, and low computational efforts.

7.1.2 Directional Drilling Modeling and Control

A dual heuristic programming based controller is first designed using a FEM directional drilling dynamics model. By applying a neural network to approximate the co-state, the DHP based approach resolves the "*curse of dimensionality*" that the traditional DP approach has. As a result, the DHP based controller has a relatively low computational expense and works well for the high-dimensional optimal control problem.

With the designed DHP based controller, a high-fidelity yet low computational expense directional drilling dynamics model is needed for real-time control validation. Chapter 5 proposed a hybrid modeling approach combining the finite element method and the transfer matrix method together, which inherits the merits of both modeling accuracy and computational efficiency.

Finally, a software-in-the-loop real-time simulation testbed is developed in Chapter 6 to test the DHP based controller designed in Chapter 4. A 68 DOF hybrid directional drilling dynamics model is used to validate the controller's performance in terms of vibration mitigation and trajectory tracking.

REFERENCES

[1] S. Laik, *Offshore Petroleum Drilling and Production*. CRC Press, 2018.

[2] T. Richard, C. Germay, and E. Detournay, "A simplified model to explore the root cause of stick–slip vibrations in drilling systems with drag bits," *Journal of sound and vibration*, vol. 305, no. 3, pp. 432–456, 2007.

[3] J. M. Kamel and A. S. Yigit, "Modeling and analysis of stick-slip and bit bounce in oil well drillstrings equipped with drag bits," *Journal of Sound and Vibration*, vol. 333, no. 25, pp. 6885–6899, 2014.

[4] M. E. Merchant, "Mechanics of the metal cutting process. ii. plasticity conditions in orthogonal cutting," *Journal of Applied Physics*, vol. 16, no. 6, pp. 318–324, 1945.

[5] D. Che, P. Han, P. Guo, and K. Ehmann, "Issues in polycrystalline diamond compact cutter–rock interaction from a metal machining point of view-part ii: bit performance and rock cutting mechanics," *Journal of Manufacturing Science and Engineering*, vol. 134, no. 6, p. 064002, 2012.

[6] C. Fairhurst and W. Lacabanne, "Some principles and developments in hard rock drilling techniques," 1956.

[7] E. Detournay and P. Defourny, "A phenomenological model for the drilling action of drag bits," in *International journal of rock mechanics and mining sciences & geomechanics abstracts*, vol. 29, pp. 13–23, Elsevier, 1992.

[8] E. Detournay, T. Richard, and M. Shepherd, "Drilling response of drag bits: Theory and experiment," *International Journal of Rock Mechanics and Mining Sciences*, vol. 45, no. 8, pp. 1347–1360, 2008.

[9] J.-H. She, X. Xin, and Y. Pan, "Equivalent-input-disturbance approach-analysis and application to disturbance rejection in dual-stage feed drive control system,"

IEEE/ASME Transactions on Mechatronics, vol. 16, no. 2, pp. 330–340, 2011.

[10] J. Cheng, M. Wu, C. Lu, L. Chen, X. Chen, W. Cao, and X. Lai, "A stick-slip vibration suppression method for the drillstring system based on neutral type model," in *Control Conference (ASCC), 2017 11th Asian*, pp. 2837–2842, IEEE, 2017.

[11] R. F. Mitchell and S. Z. Miska, *Fundamentals of drilling engineering*. Society of Petroleum Engineers, 2017.

[12] S. Song, J. Hou, Y. Liu, and C. Cao, "A perfect play of salt, bamboo and gas: The first petroleum well (breakthrough) in the world," in *AAPG Annual Convention and Exhibition*.

[13] T. Vromen, "Control of stick-slip vibrations in drilling systems," 2015.

[14] C. Ke and X. Song, "Computationally efficient down-hole drilling system dynamics modeling integrating finite element and transfer matrix," *Journal of Dynamic Systems, Measurement, and Control*, vol. 139, no. 12, p. 121003, 2017.

[15] J. Bailey and I. Finnie, "An analytical study of drill-string vibration," *Journal of Engineering for Industry*, vol. 82, no. 2, pp. 122–127, 1960.

[16] P. Paslay and D. Bogy, "Drill string vibrations due to intermittent contact of bit teeth," *Journal of engineering for industry*, vol. 85, no. 2, pp. 187–194, 1963.

[17] D. Dareing and B. J. Livesay, "Longitudinal and angular drill-string vibrations with damping," *Journal of Engineering for Industry*, vol. 90, no. 4, pp. 671–679, 1968.

[18] L. F. Kreisle, J. M. Vance, *et al.*, "Mathematical analysis of the effect of a shock sub on the longitudinal vibrations of an oilwell drill string," *Society of Petroleum Engineers Journal*, vol. 10, no. 04, pp. 349–356, 1970.

[19] D. Dareing, "Guidelines for controlling drill string vibrations," *Journal of energy resources technology*, vol. 106, no. 2, pp. 272–277, 1984.

[20] D. W. Dareing *et al.*, "Drill collar length is a major factor in vibration control," *Journal of petroleum technology*, vol. 36, no. 04, pp. 637–644, 1984.

[21] E. Skaugen, A. Kyllingstad, *et al.*, "Performance testing of shock absorbers," in *SPE Annual Technical Conference and Exhibition*, Society of Petroleum Engineers, 1986.

[22] E. Skaugen *et al.*, "The effects of quasi-random drill bit vibrations upon drillstring dynamic behavior," in *SPE Annual Technical Conference and Exhibition*, Society of Petroleum Engineers, 1987.

[23] H. Y. Lee, *Drillstring axial vibration and wave propagation in boreholes*. PhD thesis, Massachusetts Institute of Technology, 1991.

[24] V. Dunayevsky, F. Abbassian, A. Judzis, *et al.*, "Dynamic stability of drillstrings under fluctuating weight on bit," *SPE drilling & completion*, vol. 8, no. 02, pp. 84–92, 1993.

[25] S. Parfitt, F. Abbassian, *et al.*, "A model for shock sub performance qualification," in *SPE/IADC Drilling Conference*, Society of Petroleum Engineers, 1995.

[26] J. Niedzwecki and S. Thampi, "Heave compensated response of long multi-segment drill strings," *Applied Ocean Research*, vol. 10, no. 4, pp. 181–190, 1988.

[27] B. Schmalhorst, E. Brommundt, A. Baumgart, U. Richter, *et al.*, "Drilling dynamics in the presence of mud flow," in *IADC/SPE Drilling Conference*, Society of Petroleum Engineers, 2000.

[28] M. Elsayed and C. C. Phung, "Modeling of drillstrings," in *ASME 2005 24th International Conference on Offshore Mechanics and Arctic Engineering*, pp. 15–24, American Society of Mechanical Engineers, 2005.

[29] Z. Li, B. Guo, *et al.*, "Analysis of longitudinal vibration of drill string in air and gas drilling," in *Rocky Mountain Oil & Gas Technology Symposium*, Society of Petroleum Engineers, 2007.

[30] J. Tian, C. Wu, L. Yang, Z. Yang, G. Liu, and C. Yuan, "Mathematical modeling and analysis of drill string longitudinal vibration with lateral inertia effect," *Shock and Vibration*, vol. 2016, 2016.

[31] Y.-Q. Lin and Y.-H. Wang, "Stick-slip vibration of drill strings," *Journal of Engineering for Industry*, vol. 113, no. 1, pp. 38–43, 1991.

[32] J. Jansen and L. Van den Steen, "Active damping of self-excited torsional vibrations in oil well drillstrings," *Journal of sound and vibration*, vol. 179, no. 4, pp. 647–668, 1995.

[33] W. Tucker and C. Wang, "An integrated model for drill-string dynamics," *Journal of sound and vibration*, vol. 224, no. 1, pp. 123–165, 1999.

[34] G. Halsey, A. Kyllingstad, T. Aarrestad, D. Lysne, *et al.*, "Drillstring torsional vibrations: Comparison between theory and experiment on a full-scale research drilling rig," in *SPE Annual Technical Conference and Exhibition*, Society of Petroleum Engineers, 1986.

[35] A. Baumgart, "Stick-slip and bit-bounce of deep-hole drillstrings," *Journal of energy resources technology*, vol. 122, no. 2, pp. 78–82, 2000.

[36] N. Challamel, H. Sellami, E. Chenevez, L. Gossuin, *et al.*, "A stick-slip analysis based on rock/bit interaction: Theoretical and experimental contribution," in *IADC/SPE Drilling Conference*, Society of Petroleum Engineers, 2000.

[37] B. Besselink, N. van de Wouw, and H. Nijmeijer, "A Semi-Analytical of Stickslip Oscillations in Drilling Systems," *ASME Journal of Computational and Nonlinear Dynamics*, vol. 6, pp. 021006–1.

[38] D. A. Barton, B. Krauskopf, and R. E. Wilson, "Nonlinear dynamics of torsional waves in a drill-string model with spatial extent," *Journal of Vibration and Control*, vol. 16, no. 7-8, pp. 1049–1065, 2010.

[39] E. M. Navarro-López and D. Cortés, "Avoiding harmful oscillations in a drillstring through dynamical analysis," *Journal of sound and vibration*, vol. 307, no. 1, pp. 152–171, 2007.

[40] S. S. Rao, *Vibration of Continuous Systems*. John Wiley & Sons, 2007.

[41] A. T. Beck and C. R. da Silva Jr, "Timoshenko versus euler beam theory: Pitfalls of a deterministic approach," *Structural Safety*, vol. 33, no. 1, pp. 19–25, 2011.

[42] A. Ghasemloonia, D. G. Rideout, and S. D. Butt, "A Review of Drillstring Vibration Modeling and Suppression Methods," *Journal of Petroleum Science and Engineering*, vol. 131, pp. 150–164, jul 2015.

[43] R.-J. Shyu, *Bending Vibration of Rotating Drill Strings*. PhD thesis, Massachusetts Institute of Technology, 1989.

[44] J. Jansen, "Non-linear rotor dynamics as applied to oilwell drillstring vibrations," *Journal of sound and vibration*, vol. 147, no. 1, pp. 115–135, 1991.

[45] S. Chen and M. Géradin, "An improved transfer matrix technique as applied to bha lateral vibration analysis," *Journal of Sound and Vibration*, vol. 185, no. 1, pp. 93–106, 1995.

[46] A. Berlioz, J. Der Hagopian, R. Dufour, and E. Draoui, "Dynamic behavior of a drillstring: experimental investigation of lateral instabilities," 1996.

[47] A. Christoforou and A. Yigit, "Dynamic modelling of rotating drillstrings with borehole interactions," *Journal of sound and vibration*, vol. 206, no. 2, pp. 243–260, 1997.

[48] P. Spanos, M. Payne, and C. Secora, "Bottom-hole assembly modeling and dynamic response determination," *Journal of Energy Resources Technology*, vol. 119, no. 3, pp. 153–158, 1997.

[49] P. Spanos, A. Chevallier, and N. P. Politis, "Nonlinear stochastic drill-string vibrations," *Journal of vibration and acoustics*, vol. 124, no. 4, pp. 512–518, 2002.

[50] L. Khajiyeva, A. Kudaibergenov, and A. Kudaibergenov, "The effect of gas and fluid flows on nonlinear lateral vibrations of rotating drill strings," *Communications in Nonlinear Science and Numerical Simulation*, vol. 59, pp. 565–579, 2018.

[51] M. Elsayed and D. W. Raymond, "Analysis of coupling between axial and torsional vibration in a compliant model of a drillstring equipped with a pdc bit," in *ASME 2002 Engineering Technology Conference on Energy*, pp. 897–904, American Society of Mechanical Engineers, 2002.

[52] A. S. Yigit and A. P. Christoforou, "Stick-slip and bit-bounce interaction in oil-well drillstrings," *Journal of Energy Resources Technology*, vol. 128, no. 4, pp. 268–274, 2006.

[53] R. Sampaio, M. Piovan, and G. V. Lozano, "Coupled axial/torsional vibrations of drillstrings by means of non-linear model," *Mechanics Research Communications*, vol. 34, no. 5-6, pp. 497–502, 2007.

[54] M. Zamanian, S. E. Khadem, and M. Ghazavi, "Stick-slip oscillations of drag bits by considering damping of drilling mud and active damping system," *Journal of Petroleum Science and Engineering*, vol. 59, no. 3-4, pp. 289–299, 2007.

[55] A. Chi, J. Zhang, W. Ge, and B. Guo, "Prediction of drillstring fatigue life under axial-torsional-combined vibration," in *SPE Gas Technology Symposium in Calgray, Alberta, Canada. SPE*, vol. 99356, 2006.

[56] C. Germay, V. Denoël, and E. Detournay, "Multiple mode analysis of the self-excited vibrations of rotary drilling systems," *Journal of Sound and Vibration*, vol. 325, no. 1-2, pp. 362–381, 2009.

[57] M. A. Trindade, C. Wolter, and R. Sampaio, "Karhunen–loeve decomposition of coupled axial/bending vibrations of beams subject to impacts," *Journal of sound and vibration*, vol. 279, no. 3-5, pp. 1015–1036, 2005.

[58] H. Hakimi and S. Moradi, "Drillstring vibration analysis using differential quadrature method," *Journal of Petroleum Science and Engineering*, vol. 70, no. 3-4, pp. 235–242, 2010.

[59] A. A. Jafari, R. Kazemi, and M. F. Mahyari, "The effects of drilling mud and weight bit on stability and vibration of a drill string," *Journal of Vibration and Acoustics*, vol. 134, no. 1, p. 011014, 2012.

[60] R. Kazemi, A. A. Jafari, and M. F. Mahyari, "The effect of drilling mud flow on the lateral and axial vibrations of drill string," in *ASME 2010 10th Biennial Conference on Engineering Systems Design and Analysis*, pp. 465–473, American Society of Mechanical Engineers, 2010.

[61] S. Sahebkar, M. Ghazavi, S. Khadem, and M. Ghayesh, "Nonlinear vibration analysis of an axially moving drillstring system with time dependent axial load and axial velocity in inclined well," *Mechanism and Machine Theory*, vol. 46, no. 5, pp. 743–760, 2011.

[62] A. Ghasemloonia, D. G. Rideout, and S. D. Butt, "Coupled transverse vibration modeling of drillstrings subjected to torque and spatially varying axial load," *Proceedings of the Institution of Mechanical Engineers, Part C: Journal of Mechanical Engineering Science*, vol. 227, no. 5, pp. 946–960, 2013.

[63] S. Al-Hiddabi, B. Samanta, and A. Seibi, "Non-linear control of torsional and bending vibrations of oilwell drillstrings," *Journal of sound and vibration*, vol. 265, no. 2, pp. 401–415, 2003.

[64] R. Leine, D. Van Campen, and W. Keultjes, "Stick-slip whirl interaction in drillstring dynamics," *Journal of Vibration and Acoustics*, vol. 124, no. 2, pp. 209–220, 2002.

[65] H. Melakhessou, A. Berlioz, and G. Ferraris, "A nonlinear well-drillstring interaction model," *Journal of vibration and acoustics*, vol. 125, no. 1, pp. 46–52, 2003.

[66] N. Vlajic, C.-M. Liao, H. Karki, and B. Balachandran, "Stick-slip and whirl motions of drill strings: Numerical and experimental studies," in *ASME 2011 International Design*

Engineering Technical Conferences and Computers and Information in Engineering Conference, pp. 829–838, American Society of Mechanical Engineers, 2011.

[67] C.-M. Liao, *Experimental and numerical studies of drill-string dynamics*. PhD thesis, 2011.

[68] C.-M. Liao, B. Balachandran, M. Karkoub, and Y. L. Abdel-Magid, "Drill-string dynamics: reduced-order models and experimental studies," *Journal of Vibration and Acoustics*, vol. 133, no. 4, p. 041008, 2011.

[69] Y. Khulief and H. Al-Naser, "Finite element dynamic analysis of drillstrings," *Finite elements in analysis and design*, vol. 41, no. 13, pp. 1270–1288, 2005.

[70] Y. Khulief, F. Al-Sulaiman, and S. Bashmal, "Vibration analysis of drillstrings with string-borehole interaction," *Proceedings of the Institution of Mechanical Engineers, Part C: Journal of Mechanical Engineering Science*, vol. 222, no. 11, pp. 2099–2110, 2008.

[71] T. Ritto, R. Sampaio, and C. Soize, "Drill-string dynamics coupled with the drilling fluid dynamics," in *XIII International Symposium on Dynamic Problems of Mechanics (DINAME 2009)*, pp. 1–10, ABCM, 2009.

[72] T. Feng, M. Vadali, Z. Ma, D. Chen, and J. Dykstra, "A finite element method with full bit-force modeling to analyze drillstring vibration," *Journal of Dynamic Systems, Measurement, and Control*, vol. 139, no. 9, p. 091016, 2017.

[73] T. Richard, C. Germay, and E. Detournay, "Self-excited stick–slip oscillations of drill bits," *Comptes rendus MECANIQUE*, vol. 332, no. 8, pp. 619–626, 2004.

[74] K. Nandakumar and M. Wiercigroch, "Stability analysis of a state dependent delayed, coupled two dof model of drill-string vibration," *Journal of Sound and Vibration*, vol. 332, no. 10, pp. 2575–2592, 2013.

[75] M. Kapitaniak, V. V. Hamaneh, J. P. Chávez, K. Nandakumar, and M. Wiercigroch, "Unveiling complexity of drill–string vibrations: Experiments and modelling," *International Journal of Mechanical Sciences*, vol. 101, pp. 324–337, 2015.

[76] A. Christoforou and A. Yigit, "Fully coupled vibrations of actively controlled drillstrings," *Journal of sound and vibration*, vol. 267, no. 5, pp. 1029–1045, 2003.

[77] T. Ritto, M. Escalante, R. Sampaio, and M. B. Rosales, "Drill-string horizontal dynamics with uncertainty on the frictional force," *Journal of Sound and Vibration*, vol. 332, no. 1, pp. 145–153, 2013.

[78] J. Bélair, S. A. Campbell, and P. van den Driessche, "Frustration, stability, and delay-induced oscillations in a neural network model," *SIAM Journal on Applied Mathematics*, vol. 56, no. 1, pp. 245–255, 1996.

[79] B. Balachandran, T. Kalmár-Nagy, and D. E. Gilsinn, *Delay differential equations*. Springer, 2009.

[80] B. Saldivar, S. Mondié, J.-J. Loiseau, and V. Rasvan, "Stick-slip oscillations in oillwell drilstrings: Distributed parameter and neutral type retarded model approaches," *IFAC Proceedings Volumes*, vol. 44, no. 1, pp. 284–289, 2011.

[81] I. Boussaada, A. Cela, H. Mounier, and S.-I. Niculescu, "Control of drilling vibrations: A time-delay system-based approach," *IFAC Proceedings Volumes*, vol. 46, no. 3, pp. 226–231, 2013.

[82] B. Saldivar, T. Knüppel, F. Woittennek, I. Boussaada, H. Mounier, and S.-I. Niculescu, "Flatness-based control of torsional-axial coupled drilling vibrations," *IFAC Proceedings Volumes*, vol. 47, no. 3, pp. 7324–7329, 2014.

[83] B. Saldivar, S. Mondié, J.-J. Loiseau, and V. Rasvan, "Exponential stability analysis of the drilling system described by a switched neutral type delay equation with nonlinear perturbations," in *Decision and Control and European Control Conference (CDC-ECC), 2011 50th IEEE Conference on*, pp. 4164–4169, IEEE, 2011.

[84] B. Saldivar and S. Mondié, "Drilling vibration reduction via attractive ellipsoid method," *Journal of the Franklin Institute*, vol. 350, no. 3, pp. 485–502, 2013.

[85] Y. Nishimatsu, "The mechanics of rock cutting," in *International Journal of Rock Mechanics and Mining Sciences & Geomechanics Abstracts*, vol. 9, pp. 261–270, Elsevier, 1972.

[86] S. SCHMIDBAUER, "Sur l'état du stockage définitif dans la république fédérale d'allemagne et dans un domaine international," in *Berichte: Siebter Internationaler Kongress Über Felsmechanik*, vol. 3, p. 1463, CRC Press, 1991.

[87] J. Cheatham and P. Gnirk, "The mechanics of rock failure associated with drilling at depth," in *Failure and Breakage of Rock, Proceedings of the 8th Symposium on Rock Mechanics, University of Minnesota, September*, pp. 15–17, 1966.

[88] T. Warren, A. Sinor, *et al.*, "Drag bit performance modeling," in *SPE Annual Technical Conference and Exhibition*, Society of Petroleum Engineers, 1986.

[89] D. A. Glowka *et al.*, "Use of single-cutter data in the analysis of pdc bit designs: Part 1-development of a pdc cutting force model," *Journal of Petroleum Technology*, vol. 41, no. 08, pp. 797–849, 1989.

[90] E. Detournay, C. Atkinson, *et al.*, "Influence of pore pressure on the drilling response of pdc bits," in *The 32nd US Symposium on Rock Mechanics (USRMS)*, American Rock Mechanics Association, 1991.

[91] J. I. Adachi, E. Detournay, and A. Drescher, "Determination of rock strength parameters from cutting tests," *Proc. NARMS*, pp. 1517–1523, 1996.

[92] J. Almenara and E. Detournay, "Cutting experiments in sandstones with blunt pdc cutters," in *Rock Characterization: ISRM Symposium, Eurock'92, Chester, UK, 14–17 September 1992*, pp. 215–220, Thomas Telford Publishing, 1992.

[93] W. Samiselo, *Rock-tool friction as a cuttability predictor*. PhD thesis, Master s Thesis Imperial College, London, 1992.[Links], 1992.

[94] E. Kuru and A. Wojtanowicz, "An experimental study of sliding friction between pdc drill cutters and rocks," in *International Journal of Rock Mechanics and Mining Sciences and Geomechanics Abstracts*, vol. 6, p. 278A, 1995.

[95] L. Gerbaud, S. Menand, and H. Sellami, "Pdc bits: all comes from the cutter rock interaction," in *IADC/SPE Drilling Conference*, p. 1, 2006.

[96] D. Zijsling *et al.*, "Analysis of temperature distribution and performance of polycrystalline diamond compact bits under field drilling conditions," in *SPE annual technical conference and exhibition*, Society of Petroleum Engineers, 1984.

[97] I. Rostamsowlat, "Effect of cutting tool properties and depth of cut in rock cutting: an experimental study," *Rock Mechanics and Rock Engineering*, vol. 51, no. 6, pp. 1715–1728, 2018.

[98] I. Rostamsowlat, T. Richard, and B. Evans, "An experimental study of the effect of back rake angle in rock cutting," *International Journal of Rock Mechanics and Mining Sciences*, vol. 107, pp. 224–232, 2018.

[99] A. Serrarens, "H-infinite control as applied to torsional drillstring dynamics," 1997.

[100] R. W. Tucker and C. Wang, "Torsional vibration control and cosserat dynamics of a drill-rig assembly," *Meccanica*, vol. 38, no. 1, pp. 145–161, 2003.

[101] F. Abdulgalil and H. Siguerdidjane, "Backstepping design for controlling rotary drilling system," in *Control Applications, 2005. CCA 2005. Proceedings of 2005 IEEE Conference on*, pp. 120–124, IEEE, 2005.

[102] M. Karkoub, Y. Abdel-Magid, B. Balachandran, *et al.*, "Drill-string torsional vibration suppression using ga optimized controllers," *Journal of Canadian Petroleum Technology*, vol. 48, no. 12, pp. 32–38, 2009.

[103] E. Kreuzer and M. Steidl, "Controlling torsional vibrations of drill strings via decomposition of traveling waves," *Archive of Applied Mechanics*, vol. 82, no. 4, pp. 515–531, 2012.

[104] C. Sagert, F. Di Meglio, M. Krstic, and P. Rouchon, "Backstepping and flatness approaches for stabilization of the stick-slip phenomenon for drilling," *IFAC Proceedings Volumes*, vol. 46, no. 2, pp. 779–784, 2013.

[105] T. Feng, H. Zhang, and D. Chen, "Dynamic programming based controllers to suppress stick-slip in a drilling system," in *2017 American Control Conference (ACC)*, pp. 1302–1307, IEEE, 2017.

[106] X. Song, Y. Zhao, and J. Dykstra, "Active damping of acoustic ringing effect for oil well sonic logging system," *IEEE Transactions on Industrial Electronics*, vol. 64, no. 4, pp. 3423–3432, 2017.

[107] D. P. Bertsekas, *Dynamic Programming and Optimal Control*, vol. 1. Athena Scientific Belmont, MA, 1995.

[108] N. P. Faísca, K. I. Kouramas, P. M. Saraiva, B. Rustem, and E. N. Pistikopoulos, "A multi-parametric programming approach for constrained dynamic programming problems," *Optimization Letters*, vol. 2, no. 2, pp. 267–280, 2008.

[109] R. E. Bellman and S. E. Dreyfus, *Applied dynamic programming*. Princeton university press, 2015.

[110] X. Song, M. A. M. Zulkefli, Z. Sun, and H.-C. Miao, "Automotive transmission clutch fill control using a customized dynamic programming method," *Journal of Dynamic Systems, Measurement, and Control*, vol. 133, no. 5, p. 054503, 2011.

[111] X. Liu, N. Vlajic, X. Long, G. Meng, and B. Balachandran, "Coupled Axial-Torsional Dynamics in Rotary Drilling with State-Dependent Delay: Stability and Control," *Nonlinear Dynamics*, vol. 78, pp. 1891–1906, jul 2014.

[112] D. Tian and X. Song, "Observer design for a well-bore drilling system with down-hole measurement feedback," *Journal of Dynamic Systems, Measurement, and Control*, 2018.

[113] E. M. Navarro-López and E. Licéaga-Castro, "Non-desired transitions and sliding-mode control of a multi-dof mechanical system with stick-slip oscillations," *Chaos, Solitons & Fractals*, vol. 41, no. 4, pp. 2035–2044, 2009.

[114] M. Ghasemi and X. Song, "Control of a vertical drilling system using a cascade sliding mode controller," in *American Control Conference (ACC), 2017*, pp. 5830–5835, IEEE, 2017.

[115] M. Ghasemi and X. Song, "Trajectory tracking and rate of penetration control of downhole vertical drilling system," *Journal of Dynamic Systems, Measurement, and Control*, vol. 140, no. 9, p. 091003, 2018.

[116] S. Fubin, S. Linxiu, L. Lin, and Z. Qizhi, "Adaptive pid control of rotary drilling system with stick slip oscillation," in *Signal Processing Systems (ICSPS), 2010 2nd International Conference on*, vol. 2, pp. V2–289, IEEE, 2010.

[117] E. M. Navarro-López and D. Cortés, "Sliding-mode control of a multi-dof oilwell drill-string with stick-slip oscillations," in *2007 American Control Conference*, pp. 3837–3842, IEEE, 2007.

[118] S. K. Gupta and P. Wahi, "Global axial-torsional dynamics during rotary drilling," *Journal of Sound and Vibration*, vol. 375, pp. 332–352, 2016.

[119] C. Ke and X. Song, "Control of down-hole drilling process using a computationally efficient dynamic programming method," vol. 140, 03 2018.

[120] J.-H. She, M. Fang, Y. Ohyama, H. Hashimoto, and M. Wu, "Improving disturbance-rejection performance based on an equivalent-input-disturbance approach," *IEEE Transactions on Industrial Electronics*, vol. 55, no. 1, pp. 380–389, 2008.

[121] F. Di Meglio and U. J. F. Aarsnes, "A distributed parameter systems view of control problems in drilling," *IFAC-PapersOnLine*, vol. 48, no. 6, pp. 272–278, 2015.

[122] K. Edelman and O. Gendelman, "Dynamics of self-excited oscillators with neutral delay coupling," *Nonlinear Dynamics*, vol. 72, no. 3, pp. 683–694, 2013.

[123] J. K. Hale and S. M. V. Lunel, *Introduction to functional differential equations*, vol. 99. Springer Science & Business Media, 2013.

[124] B. Zhou and Q. Liu, "Input delay compensation for neutral type time-delay systems," *Automatica*, vol. 78, pp. 309–319, 2017.

[125] S. Boyd, L. El Ghaoui, E. Feron, and V. Balakrishnan, *Linear Matrix Inequalities in System and Control Theory*. SIAM, 1994.

[126] D. W. Ho and G. Lu, "Robust stabilization for a class of discrete-time non-linear systems via output feedback: the unified lmi approach," *International Journal of Control*, vol. 76, no. 2, pp. 105–115, 2003.

[127] M. Karkoub, M. Zribi, L. Elchaar, and L. Lamont, "Robust μ-synthesis controllers for suppressing stick-slip induced vibrations in oil well drill strings," *Multibody System Dynamics*, vol. 23, no. 2, pp. 191–207, 2010.

[128] F. Abdulgalil and H. Siguerdidjane, "Pid based on sliding mode control for rotary drilling system," in *EUROCON 2005-The International Conference on" Computer as a Tool"*, vol. 1, pp. 262–265, IEEE, 2005.

[129] M. Ghasemi and X. Song, "Trajectory tracking and rate of penetration control of downhole vertical drilling system," *Journal of Dynamic Systems, Measurement, and Control*, vol. 140, no. 9, p. 091003, 2018.

[130] D. Tian and X. Song, "Control of a downhole drilling system using integral barrier lyapunov functionals," in *2019 American Control Conference (ACC)*, pp. 1349–1354, IEEE, 2019.

[131] C. Ke and X. Song, "Drilling control system using an equivalent input disturbance based control with a neutral-type axial-torsional coupled dynamics model," *Journal of Dynamic Systems, Measurement and Control*, 2019.

[132] M. B. S. Márquez, I. Boussaada, H. Mounier, and S.-I. Niculescu, "Analysis and control of oilwell drilling vibrations," in *A Time-Delay Systems Approach, ser. Advances in Industrial Control*, Springer, 2015.

[133] U. J. F. Aarsnes and R. J. Shor, "Stick-slip and torsional friction factors in inclined wellbores," in *MATEC Web of Conferences*, vol. 148, p. 16002, EDP Sciences, 2018.

[134] C. Ke and X. Song, "Computationally efficient dynamics modeling for downhole drilling system integrating finite element and transfer matrix," in *ASME 2016 Dynamic Systems and Control Conference*, American Society of Mechanical Engineers Digital Collection, 2016.

[135] T. Feng, I. Kim, and D. Chen, "Dynamic modeling of directional drillstring: A linearized model considering well profile," *Journal of Dynamic Systems, Measurement, and Control*, vol. 140, no. 6, p. 061005, 2018.

[136] S. Arbatani, A. Callejo, J. Kövecses, M. Kalantari, N. R. Marchand, and J. Dargahi, "An approach to directional drilling simulation: Finite element and finite segment methods with contact," *Computational Mechanics*, vol. 57, no. 6, pp. 1001–1015, 2016.

[137] D. Yang, M. Rahman, and Y. Chen, "Bottomhole assembly analysis by finite difference differential method," *International journal for numerical methods in engineering*, vol. 74, no. 9, pp. 1495–1517, 2008.

[138] F. Di Meglio, U. J. Aarsnes, and R. Shor, "Advances in control of hyperbolic partial differential," *Nonlinear Dynamics and Control of Deep Drilling Systems*, p. 145.

[139] N. Bekiaris-Liberis and M. Krstic, "Compensation of wave actuator dynamics for nonlinear systems," *IEEE Transactions on Automatic Control*, vol. 59, no. 6, pp. 1555–1570, 2014.

[140] H. L. Monteiro and M. A. Trindade, "Performance analysis of proportional-integral feedback control for the reduction of stick-slip-induced torsional vibrations in oil well drillstrings," *Journal of Sound and Vibration*, vol. 398, pp. 28–38, 2017.

[141] R. J. Shor, U. J. F. Aarsnes, and F. di Meglio, "Effects of latency, motor inertia and filtering on stick-slip mitigation control," *Nonlinear Dynamics and Control of Deep Drilling Systems*, p. 133.

[142] W. B. Powell, *Approximate Dynamic Programming: Solving the curses of dimensionality*, vol. 703. John Wiley & Sons, 2007.

[143] A. Heydari and S. N. Balakrishnan, "Fixed-final-time optimal tracking control of input-affine nonlinear systems," *Neurocomputing*, vol. 129, pp. 528–539, 2014.

[144] A. Hohl, M. Tergeist, H. Oueslati, C. Herbig, M. Ichaoui, G.-P. Ostermeyer, H. Reckmann, *et al.*, "Prediction and mitigation of torsional vibrations in drilling systems," in *IADC/SPE Drilling Conference and Exhibition*, Society of Petroleum Engineers, 2016.

[145] A. Marquez, E. Omojuwa, C. Teodoriu, *et al.*, "Mitigating downhole vibrations in bottom hole assemblies using finite element analysis," in *SPE Health, Safety, Security, Environment, & Social Responsibility Conference-North America*, Society of Petroleum Engineers, 2017.

[146] G.-R. Liu and S. S. Quek, *The finite element method: a practical course*. Butterworth-Heinemann, 2013.

[147] T. Sardarmehni, "Near-optimal control of switched systems with continuous-time dynamics using approximate dynamic programming," 2018.

[148] W. Rudin *et al.*, *Principles of Mathematical Analysis*, vol. 3. McGraw-hill New York, 1964.

[149] J. A. Pabon, N. Wicks, Y. Chang, B. Dow, R. J. Harmer, *et al.*, "Modeling transient vibrations while drilling using a finite rigid body approach," in *SPE Deepwater Drilling and Completions Conference*, Society of Petroleum Engineers, 2010.

[150] J. Rudat, D. Dashevskiy, *et al.*, "Development of an innovative model-based stick/slip control system," in *SPE/IADC Drilling Conference and Exhibition*, Society of Petroleum Engineers, 2011.

[151] J.-H. Han, Y.-J. Kim, and M. Karkoub, "Modeling of wave propagation in drill strings using vibration transfer matrix methods," *The Journal of the Acoustical Society of America*, vol. 134, no. 3, pp. 1920–1931, 2013.

[152] M. Khadisov, H. Hagen, A. Jakobsen, and D. Sui, "Developments and experimental tests on a laboratory-scale drilling automation system," *Journal of Petroleum Exploration and Production Technology*, pp. 1–17, 2019.

[153] M. B. Ayed, L. Zouari, and M. Abid, "Software in the loop simulation for robot manipulators," *Engineering, Technology & Applied Science Research*, vol. 7, no. 5, 2017.